Laser Field Interactions with Atoms and Molecules

by

Ye Li

A dissertation submitted to the Graduate Faculty of
Auburn University
in partial fulfillment of the
requirements for the Degree of
Doctor of Philosophy

Auburn, Alabama
December 10, 2016

Keywords: atom, laser, photoionization, time-dependent close-coupling,
collisional-radiative, density-matrix

Approved by

Michael Pindzola, Chair, Professor of Department of Physics
Stuart Loch, Co-chair, Associate Professor of Department of Physics
Michael Fogle, Associate Professor of Department of Physics
Eugene Oks, Professor of Department of Physics
Konrad Patkowski, Assistant Professor of Department of Chemistry and Biochemistry

Abstract

This dissertation explores multiple areas of laser matter interactions. It studies four main topics: multi-photon (few photon) double ionization of He, double photoionization of He-like systems from level resolved states, single and double photoionization of the diatomic molecule–Li_2, and non-equilibrium modeling of the Fe XVII 3C/3D line intensity ratio for an intense x-ray free electron laser.

A time-dependent close-coupling (TDCC) method is used to calculate the five-photon double ionization of He. It is found that the generalized cross section used in the past for two-photon double ionization of He cannot be extended to five-photon double ionization of He. Therefore only five-photon double ionization probabilities that depend on specific radiation field pulses can be calculated. A TDCC method is then used to calculate the multiphoton double ionization of He using femtosecond laser pulses with linear and circular polarization. Total double ionization probabilities are calculated for 2, 3, 4, and 5 photon absorption in the photon energy range from 10 to 60 eV. Single and triple differential probabilities are calculated for 2, 3, 4, and 5 photon absorption at energies where the total ionization probability is near a maximum. For circular polarization the total and differential probabilities are consistently smaller compared to linear polarization as the number of photons absorbed is increased while keeping the radiation field intensity constant. For linear polarization, the total and differential probabilities vary substantially as a function of photons absorbed due to the presence of more absorption pathways.

A semi-relativistic TDCC method is developed. The TDCC($l_1 j_1 l_2 j_2 J$) for He only includes the spin-orbit interaction, whereas the TDCC($l_1 j_1 l_2 j_2 J$) includes the spin-orbit, mass-velocity, and Darwin interactions. Double photoionization cross sections of He from the $1s^2$,

$1s2s$, and $1s2p$ configurations and Ne^{8+} from the $1s^2$ configuration are carried out using both TDCC(l_1l_2L) and TDCC($l_1j_1l_2j_2J$).

TDCC methods are used to study the single and double photoionization of Li_2. Formulations for both one-active and two-active electron methods make use of Hartree with local exchange potentials for the core electrons. Both the single and double photoionization cross sections for Li_2 are found to be larger for linear polarization than for circular polarization, in sharp contrast to that found before for H_2. In particular the double photoionization cross sections for Li_2 are found to be approximately five times larger than for H_2 and thus more easily observed by future experiments.

A review is presented for two methods used to model recent LCLS experimental results for the 3C/3D line intensity ratio of Fe XVII [1], the time-dependent collisional-radiative method and the density-matrix approach. These are described and applied to a two-level atomic system excited by an X-ray free electron laser. A range of pulse parameters is explored and the effects on the predicted Fe XVII 3C and 3D line intensity ratio are calculated. We reaffirm the conclusions from Oreshkina et al. [2, 3]: the non-linear effects in the density matrix are important and the reduction in the Fe XVII 3C/3D line intensity ratio is sensitive to the laser pulse parameters, namely pulse duration, pulse intensity, and laser bandwidth. It is also shown that for both models the lowering of the 3C/3D line intensity ratio below the expected time-independent oscillator strength ratio has a significant contribution due to the emission from the plasma after the laser pulse has left the plasma volume. Laser intensities above $\sim 1 \times 10^{12}$ W/cm^2 are required for a reduction in the 3C/3D line intensity ratio below the expected time independent oscillator strength ratio.

Acknowledgments

I would first like to express my sincere thank to my advisor Dr. Michael Pindzola. He introduced me into the field of atomic physics. He is not just the mentor of my research, but also the mentor of my life. Dr. Pindzola's courage and the attitude of persistency and consistency in research have had a huge influence on me. I look up to him as a role model.

I would also like to thank my co-advisor Dr. Stuart Loch. Dr. Loch really likes helping and guiding students through their research. He is very kind and generous. He inspires me a lot during my research. I remember there were times that we brainstorming and intensively coding just like the nights before finals.

I would then like to thank my committee members Dr. Eugene Oks, Dr. Michael Fogle and my university reader Dr. Konrad Patkowski for taking their time reading through my dissertation and providing helpful comments and suggestions. I also really enjoyed Dr. Oks' quantum mechanics classes. Dr. Oks has a really sharp mind and his classes were very well organized. I learnt a lot from his lectures, they were among my favorite lectures that I have ever had. I have also worked with Dr. Fogle on some experiments, and I learned a lot from him. Dr. Fogle has a really broad knowledge about both experiment and theory. I really thank him for guiding me during the experiments.

Dr. Connor Ballance is definitely one of the people that I own a huge thanks to. We discussed a lot of topics during the years while he was still at Auburn. He has always had a positive influence on my theoretical and computational research. Dr. Satoshi Hinata is also one of the professors who helped me a lot during my years here. I enjoyed his lectures a lot. Dr. Hinata explains things from varieties of angles and helped me improved my thinking strategy.

I would also like to thank Dr. Teck Lee, Dr. Edward Thomas and also Dr. Michael Fogle again for the teaching instruction and advice while I was working as their teaching assistant. I've been working with Mr. Dave Patrick in the undergraduate physics teaching lab for a long time. I really thank Dave for his guidance and instructions that helped my teaching skills and providing me an opportunity to run the lab.

Finally I would like to thank my family for supporting me going to graduate school, to pursue a deeper understanding of physics. They have encouraged me through my life. One really important person in my life is my wife Qi. I would not be able to make it without her love and support, she really helped me spiritually through my years here. My specially thanks go to my grandmother on mom's side. My grandmother recently passed away. I would not forget how she used to teach me and take care of me when I was little and I would like to dedicate this dissertation to her.

This dissertation is supported in part by grants from the US Department of Energy, the US National Science Foundation, and the US National Aeronautics and Space Administration. Computational work was carried out at the National Energy Research Scientific Computing Center (NERSC) in Berkeley, California, the National Institute for Computational Sciences (NICS) in Knoxville, Tennessee, the High Performance Computing Center (HRLS) in Stuttgart, Germany, and a local cluster CASIC at Auburn University, Auburn, Alabama.

Table of Contents

List of Figures

List of Tables

Chapter 1

Introduction

In this dissertation, the general topic of laser interactions with atoms and molecules is investigated. This is important as a tool to explore fundamental atomic processes, and the effects of electron-electron correlation. The time-dependent close-coupling (TDCC) method has been used with much success in such studies [4, 5]. It has been used to look at electron-impact ionization of neutral atoms[6, 7], ions [8, 9], and small molecules [10, 11], as well as photoionization processes [12, 13, 14, 15, 16]. One further system is also investigated in this dissertation, and the focus being on spectral emission from Fe^{16+}. This ion has important spectral diagnostic applications for laboratory and astrophysical plasmas [17, 18] providing an electron temperature diagnostic.

The main focus of this work is to use the TDCC method to study systems where one might expect strong correlation effects between the electrons involved in the ionization processes. Probability distributions for multi-photon double ionization of Helium atom are presented in Chapter 2 and Chapter 3. It still remains a challenge to solve the quantal three body break up problem, even from the ground state of the Helium. The TDCC method propagates the two electron wave functions and has been applied to study two photon double ionization of Helium in the past [14, 19]. With the recent experiment on five-photon sequential double ionization of He in an intense extreme-ultraviolet (EUV) free-electron-laser (FEL)[20] and the recent achievement in generating circular polarized ultrashort light pulses[21], we explore 2,3,4,5 photon double ionization of Helium, and as a result two articles have been published [22, 23]. The TDCC method is used to probe the double photoionization process of He-like systems from the level resolved perspective. In Chapter 4 we take a first step to develop a semi-relativistic TDCC method. For the double photoionization of

Helium, only the spin-orbit interaction is employed in the TDCC method. For the double photoionization of Ne^{8+}, the spin-orbit, Darwin, and mass-velocity interactions are included. As a result two publications were achieved [24, 25]. The single and double photoionization process for the Lithium molecule is studied in Chapter 5. Studies of the photoionization of diatomic molecules are important for the understanding of many astrophysical and laboratory science phenomena [26]. We use a TDCC-3D (one active electron) approach to study the single photoionization and TDCC-6D (two active electron) approach to study both the single and double ionization process of Li_2. One article was published under the study of this chapter [27]. In each of these chapters the theoretical methods are described as they are needed.

The final project of this dissertation (Chapter 6) is a study of a recent X-ray Free-Electron Laser (XFEL) experiment at the Linear Coherent Light Source (LCLS). Their measurement of the Fe XVII 3C/3D line intensity ratio was found to be very different from any theoretical calculation of the oscillator strength ratio, with the results being published in a recent Nature article [1]. Chapter 6 contains some results from a recent publication using the time-dependent collisional-radiative (CR) method [28], and then develops a density-matrix (DM) method that is also used to analyze the experiment. Time-dependent effects are found to be very important, and if the laser pulses are sufficiently intense, it can reduce the 3C/3D line intensity ratio. This work will be submitted for publication.

Chapter 2

Five Photon Double Ionization of Helium

2.1 Background

Extensive theoretical studies of the two-photon double ionization of He[14, 19, 29, 30, 31, 32, 33, 34, 35, 36, 37] have shown that in the non-sequential photon energy range between 40 eV and 50 eV that a generalized cross section (cm^4 sec) may be calculated for a constant intensity and an arbitrary number of photon energy time periods. In the non-sequential range the two continuum photoelectons only interact with each other and are strongly correlated. To test our knowledge of how strongly correlated photoelectrons behave, the fully differential and total integrated generalized cross sections are compared with experiment. However, once the photon energy moves above 50 eV near the sequential threshold of 54.4 eV for He^+, the generalized cross section breaks down as the double ionization probability divided by the total number of photon energy time periods is no longer a constant function.

Recently experimental studies of the five photon sequential double ionization of He were carried out using the free-electron laser at RIKEN[20]. These studies stimulate the question as to whether there is a photon energy range in which a generalized cross section might be calculated so as to explore how strongly correlated photoelectrons behave after absorbing five photons in a strictly non-sequential manner.

In this chapter we apply the time-dependent close-coupling method[4] to calculate five photon double ionization probabilities for a range of photon energies using a constant intensity and a range of photon energy time periods. Our main finding is that the TDCC calculations show no photon energies at which a generalized cross section can be obtained.

We then carry out furthur TDCC calculations over a range of photon energies using a femtosecond Gaussian pulse to find the photon energy at which the double ionization probability reaches a peak as a guide for future experiments.

2.2 Theory

The time-dependent Schrodinger equation for a two electron atom is given by:

$$\begin{aligned} i\frac{\partial\Psi(\vec{r}_1,\vec{r}_2,t)}{\partial t} &= \sum_{i=1}^{2}\left(-\frac{1}{2}\nabla_i^2-\frac{Z}{r_i}\right)\Psi(\vec{r}_1,\vec{r}_2,t) \\ &+\sum_{i<j=1}^{2}\frac{1}{|\vec{r}_i-\vec{r}_j|}\Psi(\vec{r}_1,\vec{r}_2,t) \\ &+E(t)\cos\omega t\sum_{i=1}^{2}r_i\cos\theta_i\Psi(\vec{r}_1,\vec{r}_2,t)\ , \end{aligned} \tag{2.1}$$

where Z is the atomic number, $E(t)$ is the electric field amplitude, and ω is the radiation field frequency. We choose a linearly polarized field in the "length" gauge.

For the possible extraction of a generalized cross section, a "constant intensity" pulse has:

$$\begin{aligned} E(t) &= E_0\sin^2(\pi t/2T) \text{ for } t<T \\ &= E_0 \text{ for } T<t<(N-1)T \\ &= E_0\sin^2(\pi t/2(N-1)T) \text{ for } (N-1)T<t<NT\ , \end{aligned} \tag{2.2}$$

where $E_0=(5.336\times10^{-9})\sqrt{I}$, I is the intensity in Watts/cm^2, $T=2\pi/\omega$ is a field period, and N is the number of field periods.

Expanding the total wavefunction, $\Psi(\vec{r}_1, \vec{r}_2, t)$, in coupled spherical harmonics for each LS symmetry and substitution into Eq.(2.1) yields the following time-dependent close-coupled partial differential equations[4]:

$$\begin{aligned} i\frac{\partial P^{LS}_{l_1 l_2}(r_1, r_2, t)}{\partial t} &= \sum_{i=1}^{2} T_{l_i}(r_i) P^{LS}_{l_1 l_2}(r_1, r_2, t) \\ &+ \sum_{l_1', l_2'} \sum_{i<j=1}^{2} V^{L}_{l_1 l_2, l_1' l_2'}(r_i, r_j) P^{LS}_{l_1' l_2'}(r_1, r_2, t) \\ &+ \sum_{L'} \sum_{l_1', l_2'} \sum_{i=1}^{2} W^{LL'}_{l_1 l_2, l_1' l_2'}(r_i, t) P^{L'S}_{l_1' l_2'}(r_1, r_2, t) \ , \end{aligned} \tag{2.3}$$

where $T_{l_i}(r_i)$ is a kinetic and nuclear energy operator, $V^{L}_{l_1 l_2, l_1' l_2'}(r_i, r_j)$ is an electron-electron interaction energy operator, and $W^{LL'}_{l_1 l_2, l_1' l_2'}(r_i, t)$ is a time-varying radiation field energy operator. Detailed expressions for the three operators have been given before, the last two involving products of 3j and 6j symbols[4]. The number of coupled channels for $l_i \leq l_{max}$ and $S = 0$ is given by[38]:

$$N_{cc} = \frac{(l_{max} + 1)(l_{max} + 2)(2l_{max} + 3)}{6} \ , \tag{2.4}$$

where $L = 2l_{max}$.

The initial condition for the solution of the time-dependent close-coupled equations is given by:

$$P^{LS}_{l_1 l_2}(r_1, r_2, t = 0) \ = \ \bar{P}^{L_0 S_0}_{l_1 l_2}(r_1, r_2, \tau \to \infty) \delta_{L, L_0} \delta_{S, S_0} \ , \tag{2.5}$$

where the radial wavefunction, $\bar{P}^{L_0S_0}_{l_1l_2}(r_1, r_2, \tau \to \infty)$ is obtained by relaxation in imaginary time:

$$\begin{aligned}
-\frac{\partial \bar{P}^{L_0S_0}_{l_1l_2}(r_1, r_2, \tau)}{\partial \tau} &= \sum_{i=1}^{2} T_{l_i}(r_i) \bar{P}^{L_0S_0}_{l_1l_2}(r_1, r_2, \tau) \\
&\quad + \sum_{l_1', l_2'} \sum_{i<j=1}^{2} V^{L}_{l_1l_2, l_1'l_2'}(r_i, r_j) \bar{P}^{L_0S_0}_{l_1'l_2'}(r_1, r_2, \tau) \ , \qquad (2.6)
\end{aligned}$$

and L_0 and S_0 are the initial term values. The initial condition for the solution of Eq.(2.6) is given by:

$$\bar{P}^{L_0S_0}_{l_1l_2}(r_1, r_2, \tau = 0) = P_{1s}(r_1) P_{1s}(r_1) \delta_{L_0,0} \delta_{S_0,0} \ , \qquad (2.7)$$

where bound, $P_{nl}(r)$, and continuum, $P_{kl}(r)$, radial wavefunctions are obtained by diagonalization of $T_l(r)$.

The time-dependent close-coupled equations are solved using standard numerical methods to obtain a discrete representation of the radial wavefunctions and all operators on a two dimensional lattice. On a massively parallel computer each r_i coordinate is partitioned over many processors. Following propagation in real time, momentum space probability amplitudes are calculated using:

$$K^{LS}_{l_1l_2}(k_1, k_2) = \int_0^\infty dr_1 \int_0^\infty dr_2 P_{k_1l_1}(r_1) P_{k_2l_2}(r_2) P^{LS}_{l_1l_2}(r_1, r_2, t \to \infty) \ . \qquad (2.8)$$

The total probability for double ionization is given by:

$$\mathcal{P}_{double} = \int_0^\infty dk_1 \int_0^\infty dk_2 \sum_{LS} \sum_{l_1l_2} |K^{LS}_{l_1l_2}(k_1, k_2)|^2 \ . \qquad (2.9)$$

The total generalized cross section for n photon double ionization is given by:

$$\sigma^n_{double} = (\frac{\omega}{I})^n \frac{\mathcal{P}_{double}}{(N-1)T} \ . \qquad (2.10)$$

2.3 Results

2.3.1 Two photon double ionization of He

Two photon double ionization probabilities for He are calculated using the TDCC method. A lattice of 360 × 360 points is used with a uniform grid spacing of $\Delta r_1 = \Delta r_2 = 0.20$. Relaxation on the lattice using Eq.(2.6) and the 4 $L = 0$ coupled channels found in Table 2.1 yields a ground state of He with an energy E = -75.8 eV. Propagation on the lattice using Eq.(2.3) and the 17 $L = 0,1,2$ coupled channels found in Table 2.1 yields the total two-photon double ionization probabilities found in Figure 2.1. The "constant intensity" pulse of Eq.(2.2) is used for both $N = 10$ and $N = 20$ total field periods with an intensity of $I = 10^{14}$ W/cm^2.

As shown in Figure 2.1 the total double ionization probabilities using Eq.(2.9) for $N = 20$ are approximately a factor of 2 higher than those for $N = 10$ over the photon energy range from 40 eV to 50 eV. As shown in Figure 2.2 the total double ionization generalized cross sections using Eq.(2.10) are thus the same whether $N = 10$ or $N = 20$ in the photon energy range from 40 eV to 50 eV.

In the photon energy range from 50 eV to 55 eV the total two-photon double ionization probabilities for $N = 20$ grow to be a factor of 5.3 times higher than those for $N = 10$ at 54 eV. Therefore, double ionization generalized cross sections can no longer be used as one approaches the He$^+$ ionization threshold of 54.4 eV, as has been noted by many theoretical groups[29, 30, 31, 32, 33, 34, 35, 36]. To study the strongly correlated motion of two continuum electrons in the field of a residual ion, the quantal three-body breakup problem, one must stay in a photon energy range for which a generalized cross section is valid. We also note that accurate double ionization generalized cross sections for photon energies below 50 eV calculated using the TDCC method[14, 19] were made using a lattice of 720 × 720 points with a lattice grid spacing of $\Delta r_1 = \Delta r_2 = 0.10$.

2.3.2 Five photon double ionization of He

Five photon double ionization probabilities for He are calculated using the TDCC method. A lattice of 720 × 720 points is used with a uniform grid spacing of Δr_1 = Δr_2 = 0.10. Relaxation on the lattice using Eq.(2.6) and the 4 $L = 0$ coupled channels found in Table 2.1 yields a ground state of He with an energy E = -78.1 eV. Propagation on the lattice using Eq.(2.3) and the 30 $L = 0$ - 6 coupled channels found in Table 2.1 yields the total five-photon double ionization probabilities found in Figure 2.3. The "constant intensity" pulse of Eq.(2.2) is used for both $N = 10$ and $N = 20$ total field periods with an intensity of $I = 10^{14}$ W/cm^2.

As shown in Figure 2.3 the total double ionization probabilities using Eq.(2.9) for $N =$ 20 are quite different from those for $N = 10$ over the entire photon energy range from 15 eV to 19 eV. Therefore, double ionization generalized cross sections cannot be obtained at any photon energy. We attribute the absence of any non-sequential double ionization photon energy range to the many different possible combinations of sequential and non-sequential processes available. The peaks in the double ionization probability shown in Figure 2.3 also appear to be due to the Fourier spectrum of the constant intensity pulse used in these calculations. Calculations of the double ionization probability in which a Gaussian shaped pulse was used for the same $N = 10$ and $N = 20$ total field periods, did not exhibit oscillations as a function of photon energy (see Section 3.3).

As a check on the lattice size, we also carried out calculations on a lattice of 1440 × 1440 points with a uniform grid spacing of Δr_1 = Δr_1 = 0.10 and found no change in the $N = 10$ and $N = 20$ results. Thus, the lattice boundary does not affect the observed double ionization probabilities. As a check on the number of coupled channels, we also carried out calculations on a lattice of 720 × 720 points with a uniform grid spacing of Δr_1 = Δr_2 = 0.10 with the 55 $L = 0$ - 8 coupled channels found in Table 2.2. Very little change is found in the double ionization probabilities. Decreasing the intensity to $I = 10^{12}$ W/cm^2

produces a double ionization probability that has the same shape as in Figure 2.3, but with substantially smaller ionization probability.

2.3.3 Five photon double ionization of He using a femtosecond pulse

Five photon double ionization probabilities for He are calculated using a "Gaussian" pulse given by:

$$E(t) = E_0 e^{-2ln(2)(t-2T_p)/T_p^2} \ , \tag{2.11}$$

where T_p is the full width at half maximum[39]. TDCC calculations for the five photon double ionization of He are presented in Figure 2.4 using the 720 × 720 lattice, the 30 $L =$ 0 - 6 coupled channels found in Table 2.2, and photon energies ranging from 18.0 eV to 23.0 eV. The Gaussian pulse of Eq.(2.11) is used with an intensity of $I = 10^{14}$ W/cm^2 and for both $T_p = 5.0\pi/\omega$ and $T_p = 10.0\pi/\omega$. Oscillations are not present and a smooth ionization probability is found as a function of photon energy. The peaks of the double ionization probabilities are found between 20 eV and 21 eV, and the full widths at half maximum are $T_p = 0.51$ fsec amd 1.02 fsec. The double ionization peaks are in reasonable agreement with an experimentally observed[20] peak of 20.4 eV from five photon double ionization of He using a free electron laser with a lower intensity (10^{12} W/cm^2) and longer pulse time (100 fsec).

2.4 Summary

A time-dependent close-coupling method has been used to calculate five photon double ionization probabilities for He. It is found that a generalized cross section, based on an ionization probability divided by the total number of photon energy periods, cannot be obtained due to the presence of mixed non-sequential and sequential processes. This is in keeping with TDCC calculations for the two photon double ionization of He in which a generalized cross section cannot be calculated for photon energies above 50 eV. We suspect that the study of the quantal three-body breakup problem is limited to the one photon and two photon double ionization of atoms.

Five-photon double ionization probabilities for He were then calculated as a function of photon energy using femtosecond Gaussian pulses. The double ionization peak energy was found to be in good agreement with experiment[20] using a free electron laser with a lower intensity and longer pulse time. In the future we plan to calculate multiphoton double ionization probabilities for atoms using attosecond to femtosecond Gaussian pulses over a wide range of intensities in support of free electron laser experiments.

Table 2.1: Coupled channels for maximum $l = 3$

channel	$(l_1 l_2)$	L	channel	$(l_1 l_2)$	L	channel	$(l_1 l_2)$	L
1	ss	0	11	sd	2	21	dp	3
2	pp	0	12	ds	2	22	df	3
3	dd	0	13	pp	2	23	fd	3
4	ff	0	14	pf	2	24	pf	4
5	sp	1	15	fp	2	25	fp	4
6	ps	1	16	dd	2	26	dd	4
7	pd	1	17	ff	2	27	ff	4
8	dp	1	18	sf	3	28	df	5
9	df	1	19	fs	3	29	fd	5
10	fd	1	20	pd	3	30	ff	6

Table 2.2: Coupled channels for maximum $l = 4$

channel	$(l_1 l_2)$	L	channel	$(l_1 l_2)$	L	channel	$(l_1 l_2)$	L
1	ss	0	21	gd	2	41	ff	4
2	pp	0	22	ff	2	42	gg	4
3	dd	0	23	gg	2	43	pg	5
4	ff	0	24	sf	3	44	gp	5
5	gg	0	25	fs	3	45	df	5
6	sp	1	26	pd	3	46	fd	5
7	ps	1	27	dp	3	47	fg	5
8	pd	1	28	pg	3	48	gf	5
9	dp	1	29	gp	3	49	ff	6
10	df	1	30	df	3	50	dg	6
11	fd	1	31	fd	3	51	gd	6
12	fg	1	32	fg	3	52	gg	6
13	gf	1	33	gf	3	53	fg	7
14	sd	2	34	sg	4	54	gf	7
15	ds	2	35	gs	4	55	gg	8
16	pp	2	36	pf	4			
17	pf	2	37	fp	4			
18	fp	2	38	dd	4			
19	dd	2	39	dg	4			
20	dg	2	40	gd	4			

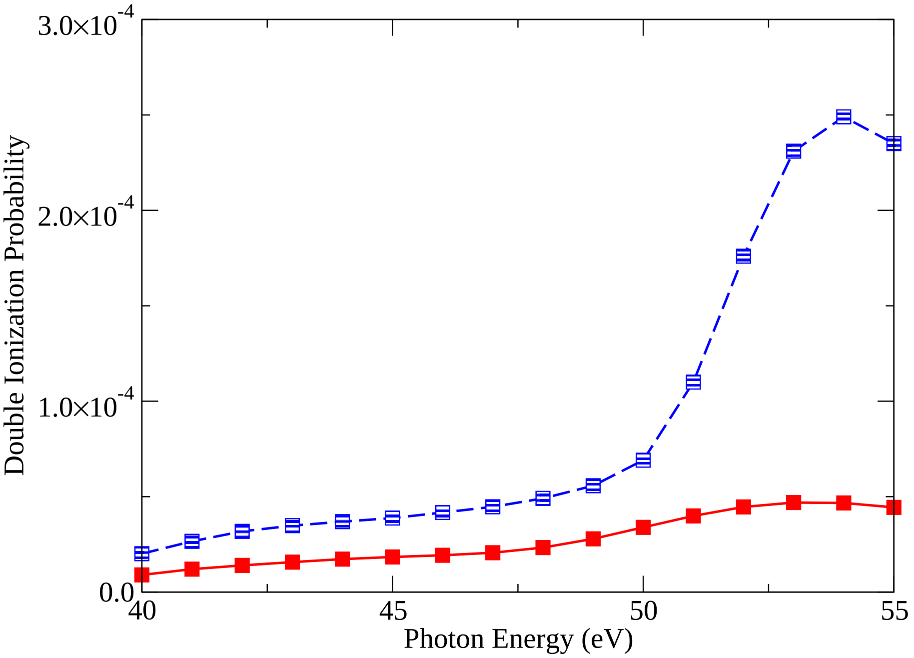

Figure 2.1: Two-photon double ionization of He. Solid line (red) : TDCC for 17 coupled channels, $\Delta r = 0.20$, and $N = 10$, dashed line (blue) : TDCC for 17 coupled channels, $\Delta r = 0.20$, and $N = 20$.

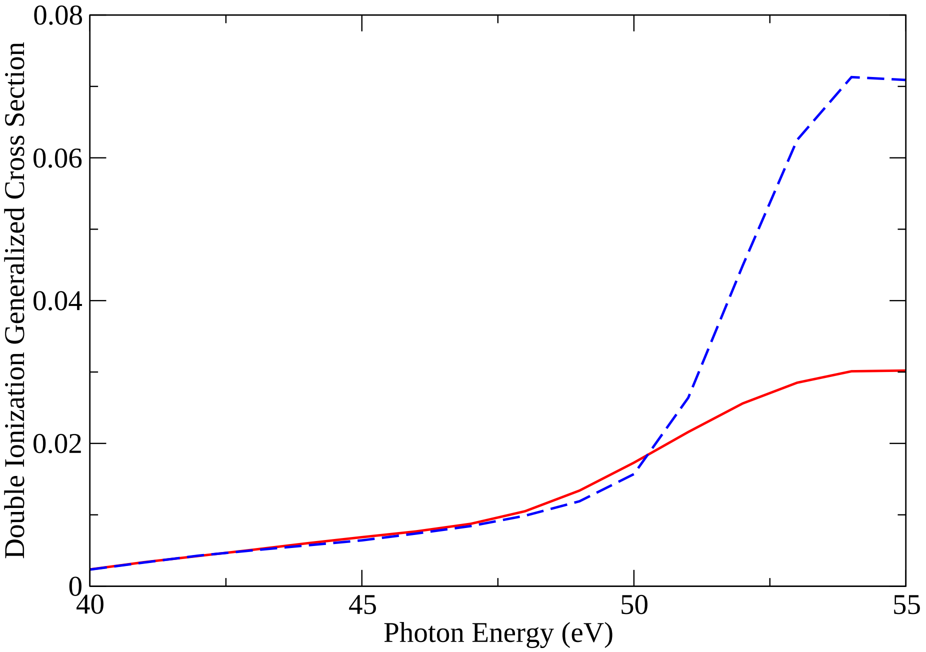

Figure 2.2: Two-photon double ionization of He. Solid line (red) : TDCC for 17 coupled channels, $\Delta r = 0.20$, and $N = 10$, dashed line (blue) : TDCC for 17 coupled channels, $\Delta r = 0.20$, and $N = 20$ (multiply by 1.90×10^{-50} to convert to cm^4 sec).

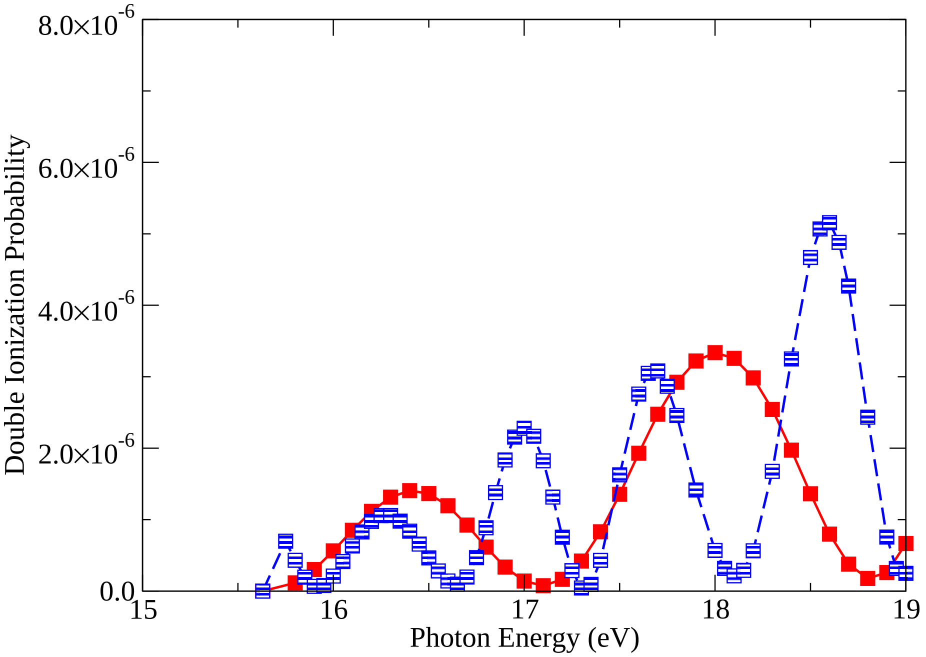

Figure 2.3: Five-photon double ionization of He. Solid line (red) : TDCC for 30 coupled channels, $\Delta r = 0.10$, and $N = 10$, dashed line (blue) : TDCC for 30 coupled channels, $\Delta r = 0.10$, and $N = 20$.

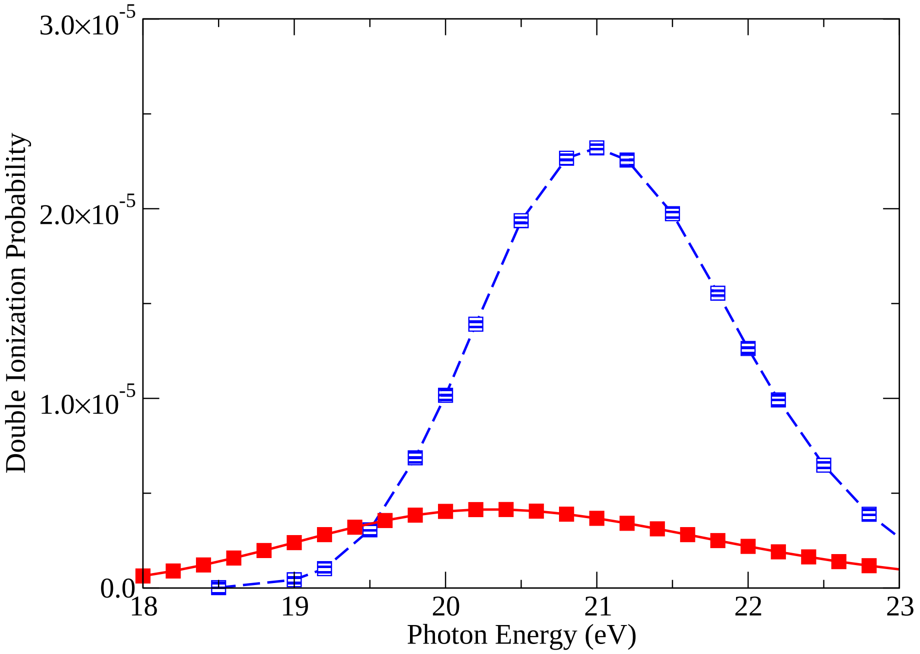

Figure 2.4: Five-photon double ionization of He. Solid line (red) : TDCC for 30 coupled channels, $I = 10^{14}$ W/cm^2, $\Delta r = 0.10$, and $T_p = 5.0\pi/\omega$, dashed line (blue): TDCC for 30 coupled channels, $I = 10^{14}$ W/cm^2, $\Delta r = 0.10$, and $T_p = 10.0\pi/\omega$.

Chapter 3

Multiphoton Double Ionization of Helium using Femtosecond Laser Pulses

3.1 Background

The development of short wavelength free electron lasers at FLASH, LCLS, and SCSS has enabled high precision studies of multiphoton ionization processes in atoms and molecules[40]. The double ionization process is quite interesting since it can involve the motion of two free electrons in the field of an atomic or molecular ion core. Even for the ground state of the He atom, the three body Coulomb breakup problem remains a theoretical challenge. In the last year, progress has been achieved in the generation of ultrashort circularly polarized light pulses[21], opening up the study of chiral sensitivity in multiphoton double ionization processes in atoms and molecules.

The study of the multiphoton double ionization of the ground state of the He atom begins with 2 photon absorption at a photon energy of 39.5 eV, corresponding to half the total experimental binding energy of the ground state[41]. Until the photon energy begins to approach 54.4 eV, corresponding to the single photon ionization of He^+, the double ionization process is completely governed by the three body correlated motion of the two electrons. In this energy range, the total double ionization probability scales with the pulse duration and the intensity squared, so that a ”generalized” cross section may be defined. Over the years a number of non-perturbative theoretical calculations have been made for the 2 photon double ionization cross sections of He. Some of the calculations employed a numerical lattice, B-splines, or basis functions to directly solve the time-dependent Schrodinger equation [14, 15, 33, 36, 32, 42, 30].

When the number of photons absorbed using linear polarized light becomes greater than 2, the double ionization of He becomes dominated by various sequential processes[43, 22]. Thus the correlated motion of the two electrons resulting in strong repulsion at equal energy sharing breaks down. We note that recently the free electron laser at SCSS was used to investigate 5 photon double ionization of the He atom in the photon energy range from 20.1 eV to 20.8 eV for a 100 fsec pulse at an intensity of 1.0×10^{12} Watts/cm^2[20].

In this chapter we apply the time-dependent close-coupling method[4] to calculate 2,3,4, and 5 photon double ionization probabilities for the ground state of He using both linearly and circularly polarized light for femtosecond laser pulses at 1.0×10^{14} Watts/cm^2. Total double ionization probabilities are calculated in the photon energy range from 10 eV to 60 eV. Single and triple differential probabilities are calculated for 2,3,4, and 5 photon absorption at the total probability peak energies. Sequential processes are found to dominate the double ionization probabilities when the number of photons absorbed is greater than 2.

The rest of this chapter is organized as follows. In section 2 we give a brief review of the theoretical method used to calculate total, single differential, and triple differential probabilities for the double ionization of the He atom. In section 3 we present double ionization probabilities for 2,3,4,and 5 photon absorption under both linear and circular polarized light for He. We conclude with a brief summary and future plans in section 4. Unless otherwise stated, we will use atomic units.

3.2 Theory

The time-dependent Schrodinger equation for the He atom is given by:

$$\begin{aligned} i\frac{\partial \Psi(\vec{r}_1,\vec{r}_2,t)}{\partial t} &= \sum_{i=1}^{2}\left(-\frac{1}{2}\nabla_i^2 - \frac{Z}{r_i}\right)\Psi(\vec{r}_1,\vec{r}_2,t) \\ &+ \left(\frac{1}{|\vec{r}_1-\vec{r}_2|}\right)\Psi(\vec{r}_1,\vec{r}_2,t) \\ &+ E(t)\cos\omega t \sum_{i=1}^{2}(Q_i)\,\Psi(\vec{r}_1,\vec{r}_2,t)\ , \end{aligned} \tag{3.1}$$

where $Z = 2$ and ω is the radiation field frequency. The radiation field amplitude is given by:

$$E(t) = E_0 \exp\left\{\left(\frac{-2\ln(2)(t-2T)^2}{T^2}\right)\right\}\ , \tag{3.2}$$

where $E_0 = (5.336 \times 10^{-9})\sqrt{I}$ and I is the intensity in Watts/cm^2. The full width at half maximum for the Gaussian pulse is given by:

$$T = \frac{N\pi}{2\omega}\ , \tag{3.3}$$

where N is the number of radiation field cycles. As an example, for $N = 10$ field cycles, $T = 1.03$ fsec for $\omega = 10$ eV and $T = 0.17$ fsec for $\omega = 60$ eV. In the "length" gauge for linearly polarized light, $Q_i = z_i$, while for circularly polarized light, $Q_i = (x_i + iy_i)/\sqrt{2}$.

Expanding the total wavefunction, $\Psi(\vec{r}_1,\vec{r}_2,t)$, in coupled spherical harmonics for each L symmetry and substitution into Eq.(3.1) yields the following time-dependent close-coupled equations[4]:

$$
\begin{aligned}
i\frac{\partial P^L_{l_1l_2}(r_1,r_2,t)}{\partial t} &= \sum_{i=1}^{2} T_{l_i}(r_i)P^L_{l_1l_2}(r_1,r_2,t) \\
&\quad + \sum_{l'_1,l'_2} V^L_{l_1l_2,l'_1l'_2}(r_1,r_2)P^L_{l'_1l'_2}(r_1,r_2,t) \\
&\quad + \sum_{L'}\sum_{l'_1,l'_2}\sum_{i=1}^{2} W^{LL'}_{l_1l_2,l'_1l'_2}(r_i,t)P^{L'}_{l'_1l'_2}(r_1,r_2,t)\ . \qquad (3.4)
\end{aligned}
$$

The kinetic and nuclear energy operator is given by:

$$
T_{l_i}(r_i) = -\frac{1}{2}\frac{d^2}{dr_i^2} + \frac{l_i(l_i+1)}{2r_i^2} - \frac{Z}{r_i}\ . \qquad (3.5)
$$

The electron-electron interaction operator is given by:

$$
\begin{aligned}
V^L_{l_1l_2,l'_1l'_2}(r_1,r_2) &= (-1)^{l'_1+l_2+L} \\
&\quad \times\sqrt{(2l_1+1)(2l_2+1)(2l'_1+1)(2l'_2+1)} \\
&\quad \times\sum_{\lambda}\frac{(r_1,r_2)^{\lambda}_{<}}{(r_1,r_2)^{\lambda+1}_{>}} \\
&\quad \times\begin{pmatrix} l_1 & \lambda & l'_1 \\ 0 & 0 & 0 \end{pmatrix}\begin{pmatrix} l_2 & \lambda & l'_2 \\ 0 & 0 & 0 \end{pmatrix}\begin{Bmatrix} l_1 & l_2 & L \\ L' & 1 & l'_1 \end{Bmatrix}\ . \qquad (3.6)
\end{aligned}
$$

The radiation field operator is given by:

$$
\begin{aligned}
W^{LL'}_{l_1l_2,l'_1l'_2}(r_i,t) &= E(t)\cos\omega t\ r_i(-1)^L\begin{pmatrix} L & 1 & L' \\ 0 & 0 & 0 \end{pmatrix} \\
&\quad \times < (l_1,l_2)L||C^1(i)||(l'_1,l'_2)L' > \qquad (3.7)
\end{aligned}
$$

for linear polarization and

$$\begin{aligned} W^{LL'}_{l_1 l_2, l'_1 l'_2}(r_i, t) &= -E(t)\cos\omega t \; r_i \begin{pmatrix} L & 1 & L' \\ -L & 1 & L' \end{pmatrix} \\ &\times < (l_1, l_2)L||C^1(i)||(l'_1, l'_2)L' > \end{aligned} \tag{3.8}$$

for circular polarization. In either case the reduced matrix elements are given by[44]:

$$\begin{aligned} < (l_1, l_2)L||C^1(1)||(l'_1, l'_2)L' > &= \delta_{l_2, l'_2}(-1)^{l_2+L'+1} \\ &\times\sqrt{(2l_1+1)(2l'_1+1)(2L+1)(2L'+1)} \\ &\times \begin{pmatrix} l_1 & 1 & l'_1 \\ 0 & 0 & 0 \end{pmatrix} \begin{Bmatrix} l_1 & l_2 & L \\ L' & 1 & l'_1 \end{Bmatrix} \end{aligned} \tag{3.9}$$

and

$$\begin{aligned} < (l_1, l_2)L||C^1(2)||(l'_1, l'_2)L' > &= \delta_{l_1, l'_1}(-1)^{l_1+l_2+l'_2+L+1} \\ &\times\sqrt{(2l_2+1)(2l'_2+1)(2L+1)(2L'+1)} \\ &\times \begin{pmatrix} l_2 & 1 & l'_2 \\ 0 & 0 & 0 \end{pmatrix} \begin{Bmatrix} l_1 & l_2 & L \\ 1 & L' & l'_2 \end{Bmatrix} . \end{aligned} \tag{3.10}$$

The initial condition for the solution of the time-dependent close-coupled equations is given by:

$$P^L_{l_1 l_2}(r_1, r_2, t = 0) = \bar{P}^{L_0}_{l_1 l_2}(r_1, r_2, \tau \to \infty)\delta_{L,L_0} , \tag{3.11}$$

where the radial wavefunction, $\bar{P}^{L_0}_{l_1 l_2}(r_1, r_2, \tau \to \infty)$, is obtained by relaxation in imaginary time of the time-dependent close-coupled equations of Eq.(3.4) without the radiation field operator (Eq. (2.6)).

Following propagation of the time-dependent close-coupled equations, momentum space amplitudes are calculated using:

$$\begin{aligned} K^L_{l_1 l_2} &= \int_0^\infty dr_1 \int_0^\infty dr_2 P_{k_1 l_1}(r_1) P_{k_2 l_2}(r_2) \\ &\quad \times P^L_{l_1 l_2}(r_1, r_2, t \to \infty) \ , \end{aligned} \tag{3.12}$$

where $P_{kl}(r)$ are continuum radial wavefunctions for He$^+$. The total multiphoton double ionization probability is given by:

$$\Phi = \int_0^\infty dk_1 \int_0^\infty dk_2 \sum_{l_1 l_2 L} |K^L_{l_1 l_2}(k_1, k_2)|^2 \ . \tag{3.13}$$

We note for two photon double ionization using linear polarization that $L = 0, 2$, while for circular polarization that $L = 2$. The single differential multiphoton double ionization probability in ejected energy, $\epsilon = k_2^2/2$, is given by:

$$\frac{d\Phi}{d\epsilon} = \frac{1}{k_1 k_2} \int_0^\infty dk_1 \int_0^\infty dk_2 \delta(\tan\alpha - \frac{k_2}{k_1}) \sum_{l_1 l_2 L} |K^L_{l_1 l_2}(k_1, k_2)|^2 \ , \tag{3.14}$$

where α is the hyperspherical angle. The triple differential multiphoton double ionization probability is given by:

$$\begin{aligned} \frac{d^3\Phi}{d\epsilon d\Omega_1 d\Omega_2} &= \frac{1}{k_1 k_2} \int_0^\infty dk_1 \int_0^\infty dk_2 \delta(\tan\alpha - \frac{k_2}{k_1}) \\ &\quad \times | \sum_{l_1 l_2 L} (-i)^{l_1 + l_2} e^{\sigma_{l_1} + \sigma_{l_2}} K^L_{l_1 l_2}(k_1, k_2) Y^L_{l_1 l_2}(\Omega_1, \Omega_2)|^2 \ , \end{aligned} \tag{3.15}$$

where σ_l are Coulomb phase shifts for He$^+$ and $Y^L_{l_1 l_2}(\Omega_1, \Omega_2)$ are coupled spherical harmonics.

3.3 Results

Multiphoton double ionization probabilities for the ground state of the He atom were calculated using the time-dependent close-coupling (TDCC) method. The TDCC equations are solved using standard numerical methods to obtain a discrete representation of the radial wavefunctions and all operators on a two dimensional lattice. Both coordinates are partitioned over the many processors on a massively parallel computer. The number of coupled channels for $l_i \leq l_{max}$ is given by[38]:

$$N_{cc} = \frac{(l_{max}+1)(l_{max}+2)(2l_{max}+3)}{6} \,, \tag{3.16}$$

where the largest L value is $2l_{max}$.

3.3.1 Total probabilities

Survey calculations were first made over a wide range of photon energies to obtain 2,3,4,and 5 photon total double ionization probabilities for He using both linear and circular polarization. The intensity was chosen at 1.0×10^{14} Watts/cm^2, the number of radiation field cycles was chosen at $N = 10$, and a lattice of 240×240 points was chosen with a uniform grid spacing of $\Delta r_i = 0.20$. The choice of $l_{max} = 5$ gives 91 coupled channels ranging from $L = 0$ to $L = 10$.

Multiphoton total double ionization probabilities are presented in Figures 3.1-3.4. Although the total angular momentum L is equal to the number of photons absorbed for circular polarization, other values of L contribute for linear polarization. For example, 3 photon double ionization involves only the L pathway $0 \rightarrow 1 \rightarrow 2 \rightarrow 3$ for circular polarization, while the L pathways $0 \rightarrow 1 \rightarrow 2 \rightarrow 3$, $0 \rightarrow 1 \rightarrow 2 \rightarrow 1$ and $0 \rightarrow 1 \rightarrow 0 \rightarrow 1$ are available for linear polarization. For 3 photon double ionization the $L = 1$ contributions are much larger than the $L = 3$ contributions. There is also a very large peak in the $L = 1$ contribution at 20 eV due to single photon excitation of the $1s2p\ {}^1P$ excited state of He.

Thus to make a clear map of the energy regions for 2,3,4, and 5 photon absorption using linear polarization, we choose to show only the maximum L contributions in Figures 3.1-3.4.

The 2 photon double ionization probabilities in Figure 3.1 are found over the energy range from 35 eV to 60 eV with a peak probability at 49 eV. The 3 photon double ionization probabilities in Figure 3.2 are found over the energy range from 24 eV to 40 eV with a peak probability at 29 eV. The 4 photon double ionization probabilities in Figure 3.3 are found over the energy range from 19 eV to 30 eV with a peak probability at 22 eV. Finally the 5 photon double ionization probabilities in Figure 3.4 are found over the energy range from 15 eV to 25 eV with a peak probability at 18 eV.

Peak total multiphoton double ionization probabilities for linear polarization are given in Table 3.1, while those for circular polarization are given in Table 3.2. The 2 photon $L = 0 + 2$ probability for linear polarization is quite close to the $L = 2$ probability for circular polarization. The 3 photon $L = 1 + 3$ probability for linear polarization is a factor of 2 larger than the $L = 3$ probability for circular polarization. The 4 photon $L = 0 + 2 + 4$ probability for linear polarization is almost the same as the $L = 4$ probability for circular polarization. Finally the 5 photon $L = 1 + 3 + 5$ probability for linear polarization is three and a half orders of magnitude larger than the $L = 5$ probability for circular polarization.

Selected calculations were made for the number of radiation field cycles set at $N = 20$. The photon energies for the peaks of the double ionization probabilities remain the same for $N = 20$, only the magnitudes of the probabilities increase.

Selected calculations were made for a choice of $l_{max} = 6$ and 140 coupled channels ranging from $L = 0$ to $L = 12$. No changes were found in the magnitudes of the double ionization probabilities for $L = 2, 3, 4, 5$ using the 140 coupled channels, although changes in magnitudes of probabilities were seen for $L > 5$ as expected.

Selected calculations were made for a lattice of 360 × 360 points with a uniform grid spacing of $\Delta r_i = 0.20$. Only very small changes were found in the magnitudes of the multiphoton total double ionization probabilities.

3.3.2 Differential probabilities

Calculations were made at the peak photon energies to obtain multiphoton differential double ionization probabilities. A lattice of 720 × 720 points with a uniform grid spacing of $\Delta r_i = 0.10$ was used to give accurate differential probabilities. Small changes were found in the magnitudes of the multiphoton total double ionization probabilities, while small shifts in the peak photon energies were observed: 51 eV for 2 photon, 29 eV for 3 photon, 23 eV for 4 photon, and 19 eV for 5 photon. The small shifts are in keeping with a 3% lowering of the total energy for He using the finer mesh. We note that a uniform momentum mesh of 100 points at $\Delta k = 0.02$ was used to calculate the momentum space amplitudes of Eq.(3.12).

Peak single differential multiphoton double ionization probabilities for linear polarization are presented in Figure 3.5, while those for circular polarization are presented in Figure 3.6. Peak triple differential multiphoton double ionization probabilities for linear polarization are presented in Figure 3.7, while those for circular polarization are presented in Figure 3.8.

The 2 photon single differential probabilities for linear and circular polarization are very similar in magnitude and shape. The minimum found at equal energy sharing is due to non-sequential electron repulsion. The 2 photon triple differential probabilities for linear and circular polarization are also very similar in magnitude and shape. At equal energy sharing with one electron emitted at 0 degrees, the dominant escape route for the other electron is at 180 degrees. The back to back emission of the two electrons at equal energy sharing for a 51 eV radiation field pulse is in agreement with theoretical calculations[14, 15, 33, 36, 32, 42, 30] for the 2 photon double ionization cross section in the non-sequential energy range from 40 eV to 52 eV.

The 3 photon single differential probabilities for linear and circular polarization are somewhat similar in magnitude and shape. We note that the linear polarization case has large contributions from $L = 1$ (see Table 3.1). For linear polarization there is a slight minimum at equal energy sharing, while for circular polarization there is a slight maximum at equal energy sharing. The 3 photon triple differential probabilities for linear and circular polarization are also somewhat similar in magnitude and shape. At equal energy sharing with one electron emitted at 0 degrees, the dominant escape route for the other electron is at 0, 36, 114, 246, and 324 degrees for linear polarization, while the escape routes for the other electron are at 42, 114, 246, and 318 degrees for circular polarization. The features in our 3 photon triple differential probabilities are in qualitative agreement with the angular distributions of Liu and Thumm [43], which were computed at a photon energy of 30 eV.

The 4 photon single differential probabilities for linear and circular polarization are fairly similar in magnitude and shape. Maximums are found at equal energy sharing. The 4 photon triple differential probabilities for linear and circular polarization are also fairly similar in magnitude and shape. At equal energy sharing with one electron emitted at 0 degrees, the dominant escape route for the other electron is at 180 degrees. Additional escape routes are found at 96 and 264 degrees for linear polarization and 90 and 270 degrees for circular polarization.

The 5 photon single differential probabilities for linear and circular polarization are very different in magnitude and shape. We note that the linear polarization case is dominated by contributions for $L = 1$ (see Table 3.1). For linear polarization there is a maximum at equal energy sharing, while for circular polarization there is a minimum at equal energy sharing. The 5 photon triple differential probabilities for linear and circular polarization are also very different in magnitude and shape. At equal energy sharing with one electron emitted at 0 degrees, the dominant escape route for the other electron is 0 degrees with other small peaks at 114 and 246 degrees for linear polarization, while the dominant escape routes for the other electron are at 78, 138, 222, and 282 degrees for circular polarization.

In regard to the multiphoton triple differential double ionization probabilities, we find that for both the linear and circular polarization cases that absorption of an odd number of photons leads to a distribution which has a minimum at back-to-back electron emissions ($\theta_1 = 0$, $\theta_2 = 180$), whereas absorption of an even number of photons leads to a distribution which has a maximum at back-to-back emissions. This behavior is consistent with the selection rules for 3 body break-up as discussed in detail by Maulbetsch and Briggs[45]. Their analysis shows that the final angular momentum state of the outgoing electron pair strongly influences the resulting electron angular distribution. They also show that the probability vanishes for back-to-back emissions ($\theta_1 = 0$, $\theta_2 =180$), when the final angular momentum state is odd. For single photon double ionization cross sections of He, such angular distributions have been studied in detail by many theoretical and experimental groups[5].

Selected calculations were made for a lattice of 1440 × 1440 points with a uniform grid spacing of $\Delta r_i = 0.10$. The calculations were made for $N = 10$ radiation field cycles followed by an additional 20 cycles in which the radiation field amplitude is set to zero. Very little change was seen in the shapes of the single and triple differential probabilities for 5 photon absorption using linear polarization. At equal energy sharing with one electron emitted at 0 degrees, the dominant escape route for the other electron remains at 0 degrees. This seems to indicate a strong sequential ionization pathway in which one electron leaves at 0 degrees followed at a later time by a second electron also at 0 degrees. Thus the electrons follow each other in time and are not able to interact and push themselves away from each other.

3.4 Summary

A time-dependent close-coupling method has been used to calculate multiphoton double ionization probabilities for He using femtosecond laser pulses. Total double ionization probabilities were calculated over the energy range from 10 eV to 60 eV to locate those energy ranges for which 2,3,4, and 5 photon absorption is the dominant process. The energy ranges are generally from 1.0 to 1.6 times the threshold energy for double ionization. Peak total double ionization probabilities were identified for the 2,3,4, and 5 photon absorption for both linear and circularly polarized light. At the total probabilities peak energies single and triple differential double ionization probabilities were calculated to guide experiments. For circular polarization the total, single differential, and triple differential double ionization probabilities drop in a steady manner as the number of photons absorbed is increased. However, for linear polarization the total, single differential, and triple differential probabilities do not drop in a steady manner. For example, the 5 photon double ionization probabilities are much larger than the 4 photon double ionization probabilities.

We hope these survey calculations will stimulate experimental studies for 2,3,4, and 5 photon double ionization of He using femtosecond laser pulses. The time-dependent close-coupling method can be easily applied to the ground and metastable excited states of many atoms and their ions for which two electrons are found above a closed shell atomic core.

Table 3.1: Total multiphoton double ionization probabilities for linear polarization

photons	energy	L	probability
2	49 eV	0	1.5×10^{-6}
		2	3.5×10^{-6}
		0+2	5.0×10^{-6}
3	29 eV	1	1.0×10^{-6}
		3	2.7×10^{-7}
		1+3	1.3×10^{-6}
4	22 eV	0	2.5×10^{-9}
		2	5.7×10^{-9}
		4	2.8×10^{-9}
		0+2+4	1.1×10^{-8}
5	18 eV	1	2.6×10^{-6}
		3	2.0×10^{-10}
		5	4.8×10^{-11}
		1+3+5	2.6×10^{-6}

Table 3.2: Total multiphoton double ionization probabilities for circular polarization

photons	energy	L	probability
2	49 eV	2	5.3×10^{-6}
3	29 eV	3	6.9×10^{-7}
4	22 eV	4	1.3×10^{-8}
5	18 eV	5	4.1×10^{-10}

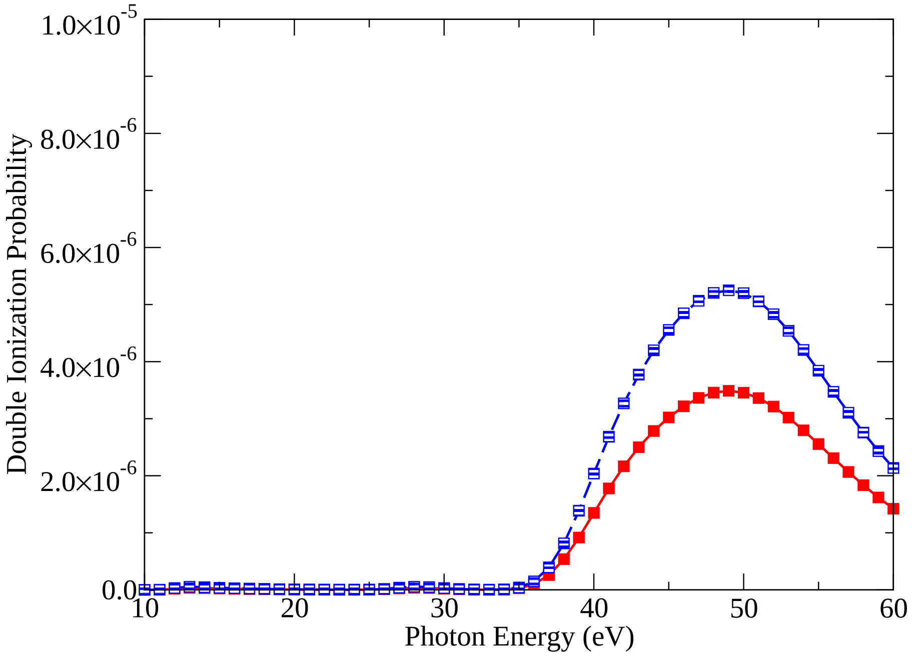

Figure 3.1: (color online) Two photon double ionization probability for $L = 2$. Solid line (red) : linear polarization, dashed line (blue) : circular polarization

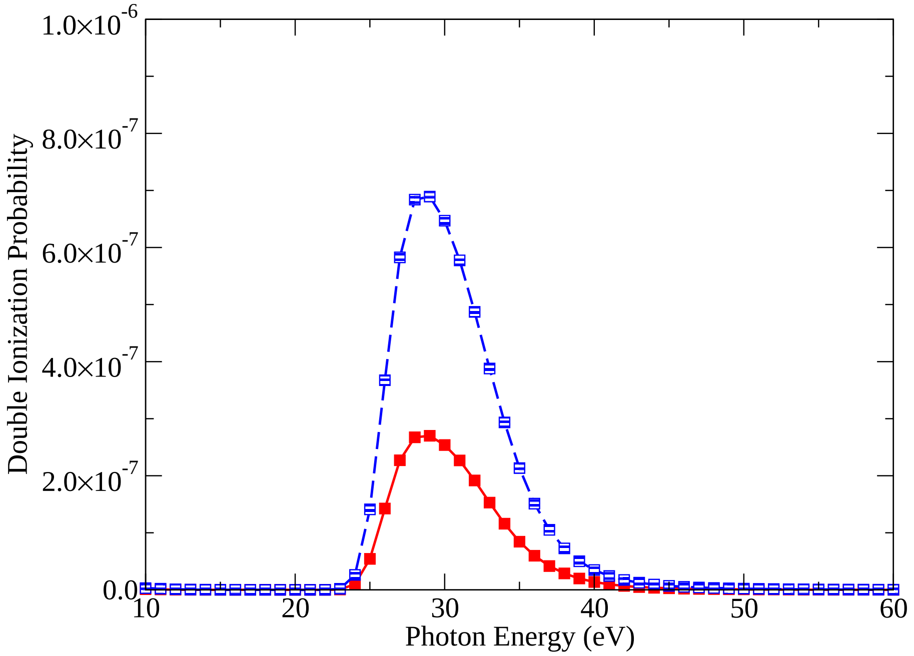

Figure 3.2: (color online) Three photon double ionization probability for $L = 3$. Solid line (red) : linear polarization, dashed line (blue) : circular polarization

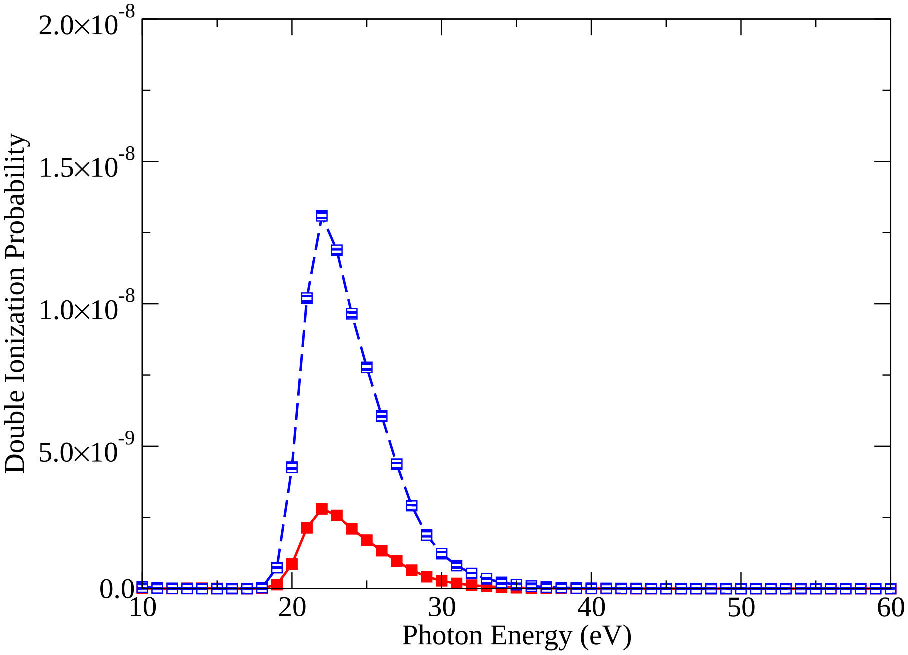

Figure 3.3: (color online) Four photon double ionization probability for $L = 4$. Solid line (red) : linear polarization, dashed line (blue) : circular polarization

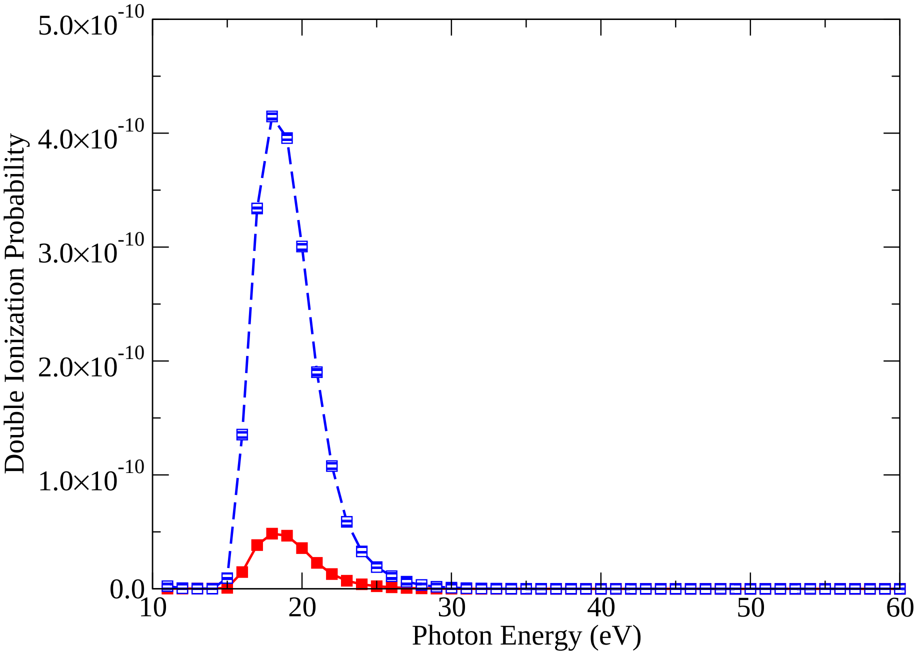

Figure 3.4: (color online) Five photon double ionization probability for $L = 5$. Solid line (red) : linear polarization, dashed line (blue) : circular polarization

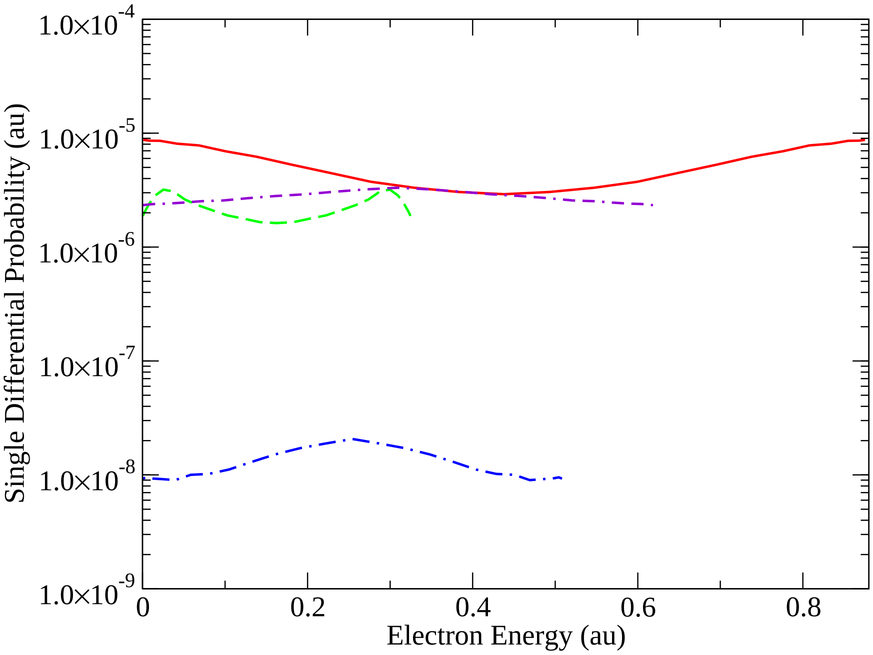

Figure 3.5: (color online) Single differential probabilities using linear polarization. Solid line (red) : two photons at 51 eV, dashed line (green): three photons at 29 eV, dot dashed line (blue): four photons at 23 eV, dot double dashed line (violet): five photons at 19 eV

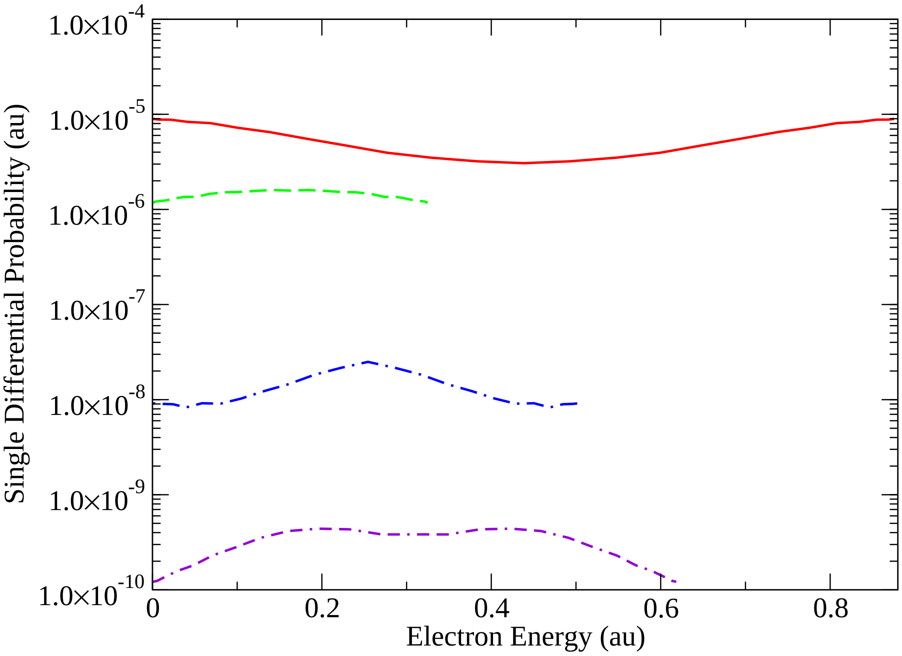

Figure 3.6: (color online) Single differential probabilities using circular polarization. Solid line (red) : two photons at 51 eV, dashed line (green): three photons at 29 eV, dot dashed line (blue): four photons at 23 eV, dot double dashed line (violet): five photons at 19 eV

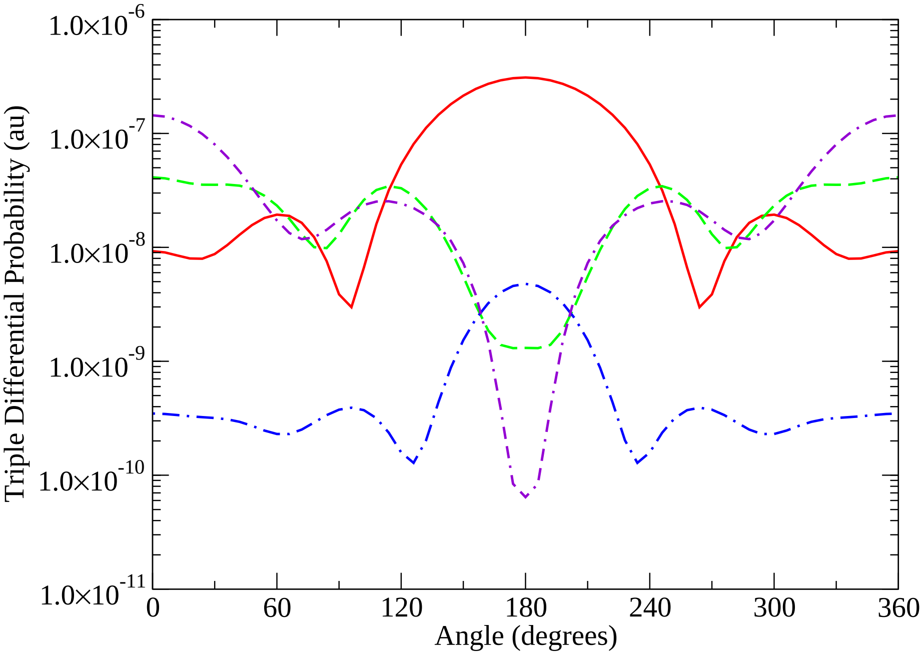

Figure 3.7: (color online) Triple differential probabilities using linear polarization. Equal energy sharing for ejected electrons, $\theta_1 = \phi_1 = \phi_2 = 0$ degrees. Solid line (red) : two photons at 51 eV, dashed line (green): three photons at 29 eV, dot dashed line (blue): four photons at 23 eV, dot double dashed line (violet): five photons at 19 eV

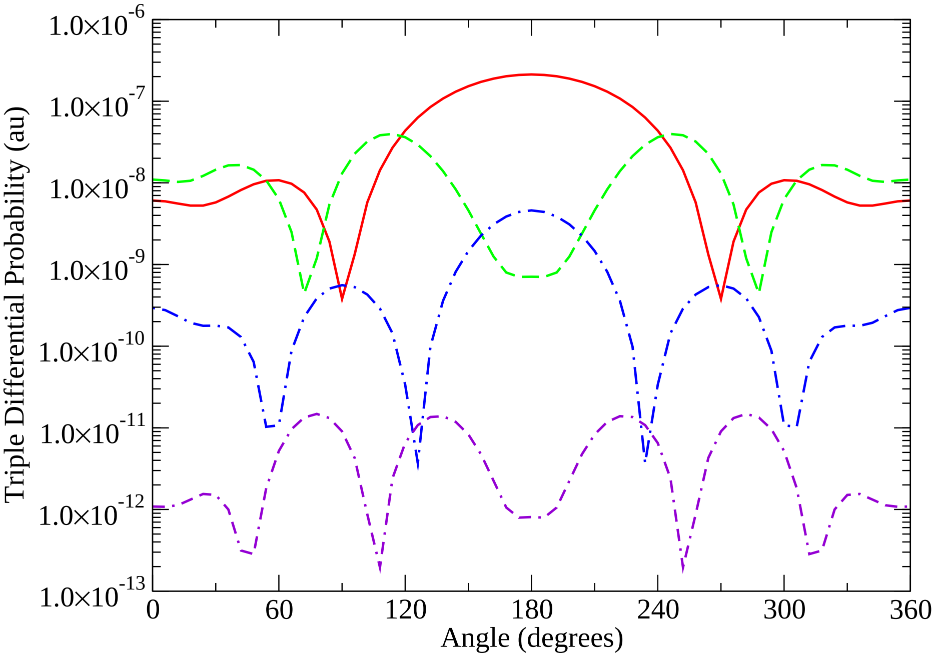

Figure 3.8: (color online) Triple differential probabilities using circular polarization. Equal energy sharing for ejected electrons, $\theta_1 = \phi_1 = \phi_2 = 0$ degrees. Solid line (red) : two photons at 51 eV, dashed line (green): three photons at 29 eV, dot dashed line (blue): four photons at 23 eV, dot double dashed line (violet): five photons at 19 eV

Chapter 4

Double Photoionization of Helium and Ne^{8+} from Level Resolved Ground and Excited States

4.1 Background

The double photoionization of atoms has been of long interest due to the difficulty in accurately describing the emission of two electrons at low photon energies. The two continuum electrons are strongly correlated and difficult to describe using many-body perturbation theory.

Good agreement was found early on between experimental measurements[46, 47] for the ratio of double photoionization to single photoionization for $\mathrm{He}(1s^2)$ and non-perturbative theoretical calculations made using the eigenchannel R-matrix method[48], the converged close-coupling method[49], the R-matrix with pseudo-states method[50], the time-dependent close-coupling method[51], and the hyperspherical close-coupling method[52]. Non-perturbative theoretical calculations for the double photoionization of $\mathrm{He}(1s2s\ ^{1,3}S)$ were also made using the eigenchannel R-matrix method[53], the converged close-coupling method[54], and the time-dependent close-coupling method[55].

With the continued development of free electron lasers, the double photoionization of atomic ions has now become of interest. For example, the double photoionization of Li^+ in ground and excited states has been calculated using the converged close-coupling method[56], the B-spline based R-matrix method[57], and the time-dependent close-coupling method[58]. For more highly charged atomic ions, all methods must include semi-relativistic effects, like the spin-orbit interaction.

In this chapter we take the first step in developing a semi-relativistic time-dependent close-coupling (TDCC) method for the double photoionization of atomic ions by exploring the inclusion of the spin-orbit interaction, the Darwin, and the mass-velocity contributions. The new TDCC method uses a $l_1j_1l_2j_2J$ coupling scheme instead of the l_1l_2L coupling scheme employed by the non-relativistic TDCC method. For the He case, only the spin-orbit interaction is included in the level resolved calculations. Double photoionization cross sections for the He atom are calculated using the TDCC(l_1l_2L) method for the $1s^2\ {}^1S$, $1s2s\ {}^3S$, and $1s2p\ {}^3P$ terms and compared with the TDCC($l_1j_2l_2j_2J$) method for the $1s^2\ {}^1S_0$, $1s2s\ {}^3S_1$, and $1s2p\ {}^3P_{0,1,2}$ levels. We find that the total double photoionization cross sections for the $1s2p\ {}^3P_{0,1,2}$ levels differ and all of their peak values are larger than the $1s2p\ {}^3P$ term peak value, with the $1s2p\ {}^3P_0$ level having the largest peak cross section. The differences in the total cross sections for the $1s2p\ {}^3P_{0,1,2}$ levels are attributed to two electron continuum correlation effects. We find that both coupling schemes give a same double photoionization cross sections for the 1s2p configuration once we average over the ${}^3P$ and ${}^1P$ terms and the ${}^3P_{0,1,2}$ and ${}^1P_1$ levels. Double photoionization cross sections for the Ne^{8+} atomic ion are also calculated using the non-relativistic TDCC(l_1l_2L) method for the $1s^2\ {}^1S$ term and compared with semi-relativistic TDCC($l_1j_2l_2j_2J$) method for the $1s^2\ {}^1S_0$ level.

4.2 Theory

The time-dependent close-coupling method was developed for the double photoionization of atoms using a $l_1 l_2 L$ coupling scheme[4]. The time-dependent close-coupling method will now be developed for the double photoionization of atoms using a $l_1 j_1 l_2 j_2 J$ coupling scheme.

The time-dependent Schrodinger equation for a two-electron atom, including spin-orbit, mass-velocity, and Darwin interactions, in a time-varying electromagnetic field is given by:

$$\begin{aligned}
i\frac{\partial \Psi(\vec{r}_1, \vec{r}_2, t)}{\partial t} &= \sum_{i=1}^{2} \left(-\frac{1}{2}\nabla_i^2 + V(r_i) \right) \Psi(\vec{r}_1, \vec{r}_2, t) \\
&+ \sum_{i=1}^{2} \left(\frac{1}{2c^2} \frac{1}{r_i} \frac{\partial V(r_i)}{\partial r_i} \vec{l}_i \cdot \vec{s}_i \right) \Psi(\vec{r}_1, \vec{r}_2, t) \\
&+ \sum_{i=1}^{2} \left(-\frac{1}{2c^2} (E_i - V(r_i))^2 \right) \Psi(\vec{r}_1, \vec{r}_2, t) \\
&+ \sum_{i=1}^{2} \left(-\frac{1}{4c^2} \frac{\partial V(r_i)}{\partial r_i} \frac{\partial}{\partial r_i} \right) \Psi(\vec{r}_1, \vec{r}_2, t) \\
&+ \frac{1}{|\vec{r}_1 - \vec{r}_2|} \Psi(\vec{r}_1, \vec{r}, t) \\
&+ E(t) \cos \omega t \; (r_1 \cos\theta_1 + r_2 \cos\theta_2) \Psi(\vec{r}_1, \vec{r}_2, t) \; , \qquad (4.1)
\end{aligned}$$

where $V(r_i) = -\frac{Z}{r_i}$, Z is the atomic number, $\vec{l}_i$ is the orbital angular momentum, $\vec{s}_i$ is the spin angular momentum, and c is the speed of light. We choose a linearly polarized radiation field in the "length" gauge, where $E(t)$ is the electric field amplitude and ω is the radiation field frequency. For the Helium case, only the spin-orbit interaction is included.

4.2.1 TDCC($l_1 l_2 L$) Method

Expanding the total wavefunction, $\Psi(\vec{r}_1, \vec{r}_2, t)$, in coupled spherical harmonics for each L symmetry and substitution into Eq.(4.1), ignoring the spin-orbit, mass-velocity, and Darwin interactions, yields the following time-dependent close-coupled partial differential equations:

$$\begin{aligned} i\frac{\partial P^L_{l_1l_2}(r_1,r_2,t)}{\partial t} &= \sum_{i=1}^{2} T_{l_i}(r_i) P^L_{l_1l_2}(r_1,r_2,t) \\ &+ \sum_{l_1'l_2'} V^L_{l_1l_2,l_1'l_2'}(r_1,r_2) P^L_{l_1'l_2'}(r_1,r_2,t) \\ &+ \sum_{l_1'l_2'L'} W^{LL'}_{l_1l_2,l_1'l_2'}(r_1,t) P^{L'}_{l_1'l_2'}(r_1,r_2,t) \\ &+ \sum_{l_1'l_2'L'} W^{LL'}_{l_1l_2,l_1'l_2'}(r_2,t) P^{L'}_{l_1'l_2'}(r_1,r_2,t) \ . \end{aligned} \tag{4.2}$$

The kinetic and nuclear energy operator is given by:

$$T_{l_i}(r_i) = -\frac{1}{2}\frac{d^2}{dr_i^2} + \frac{l_i(l_i+1)}{2r_i^2} - \frac{Z}{r_i} \ . \tag{4.3}$$

The electron-electron interaction energy operator, derived using expressions for the scalar product of two tensor operators and uncoupling formulae for reduced matrix elements[44], is given by:

$$\begin{aligned} V^L_{l_1l_2,l_1'l_2'}(r_1,r_2) &= (-1)^{l_1'+l_2+L} \\ &\times \sqrt{(2l_1+1)(2l_2+1)(2l_1'+1)(2l_2'+1)} \\ &\times \sum_{\lambda} \frac{(r_1,r_2)^{\lambda}_{<}}{(r_1,r_2)^{\lambda+1}_{>}} \begin{pmatrix} l_1 & \lambda & l_1' \\ 0 & 0 & 0 \end{pmatrix} \begin{pmatrix} l_2 & \lambda & l_2' \\ 0 & 0 & 0 \end{pmatrix} \\ &\times \begin{Bmatrix} l_1 & l_2 & L \\ l_2' & l_1' & \lambda \end{Bmatrix} \ . \end{aligned} \tag{4.4}$$

The radiation field energy operators, derived using the Wigner-Eckart theorem and uncoupling formulae for reduced matrix elements[44], are given by:

$$\begin{aligned} W^{LL'}_{l_1 l_2, l'_1 l'_2}(r_1,t) &= E(t)\cos\omega t \; r_1 \; \delta_{l_2,l'_2} \\ &\times (-1)^{l_2+L+L'-M+1}\sqrt{(2L+1)(2L'+1)} \\ &\times \sqrt{(2l_1+1)(2l'_1+1)} \\ &\times \begin{pmatrix} l_1 & 1 & l'_1 \\ 0 & 0 & 0 \end{pmatrix} \begin{pmatrix} L & 1 & L' \\ -M & 0 & M' \end{pmatrix} \\ &\times \begin{Bmatrix} l_1 & l_2 & L \\ L' & 1 & l'_1 \end{Bmatrix} \end{aligned} \tag{4.5}$$

and

$$\begin{aligned} W^{LL'}_{l_1 l_2, l'_1 l'_2}(r_2,t) &= E(t)\cos\omega t \; r_2 \; \delta_{l_1,l'_1} \\ &\times (-1)^{l_1+l_2+l'_2-M+1}\sqrt{(2L+1)(2L'+1)} \\ &\times \sqrt{(2l_2+1)(2l'_2+1)} \\ &\times \begin{pmatrix} l_2 & 1 & l'_2 \\ 0 & 0 & 0 \end{pmatrix} \begin{pmatrix} L & 1 & L' \\ -M & 0 & M' \end{pmatrix} \\ &\times \begin{Bmatrix} l_1 & l_2 & L \\ 1 & L' & l'_2 \end{Bmatrix} \; . \end{aligned} \tag{4.6}$$

We assume $M = M' = 0$ in Eqs.(4.5) and (4.6).

The close-coupling partial differential equations for relaxation in imaginary time of a two-electron atom are given by:

$$\begin{aligned} -\frac{\partial \bar{P}^{L_0}_{l_1 l_2}(r_1, r_2, \tau)}{\partial \tau} &= \sum_{i=1}^{2} T_{l_i}(r_i) \bar{P}^{L_0}_{l_1 l_2}(r_1, r_2, \tau) \\ &\quad + \sum_{l'_1 l'_2} V^{L_0}_{l_1 l_2, l'_1 l'_2}(r_1, r_2) \bar{P}^{L_0}_{l'_1 l'_2}(r_1, r_2, \tau) \ . \end{aligned} \tag{4.7}$$

The initial conditions for the solution of Eq.(4.7) are given by:

$$\bar{P}^{L_0}_{ss}(r_1, r_2, \tau = 0) = P_{1s}(r_1) P_{1s}(r_2) \tag{4.8}$$

for the $1s^2\ ^1S$ term,

$$\bar{P}^{L_0}_{ss}(r_1, r_2, \tau = 0) = \sqrt{\frac{1}{2}} P_{1s}(r_1) P_{2s}(r_2) - \sqrt{\frac{1}{2}} P_{2s}(r_1) P_{1s}(r_2) \tag{4.9}$$

for the $1s2s\ ^3S$ term, and

$$\begin{aligned} \bar{P}^{L_0}_{sp}(r_1, r_2, \tau = 0) &= +\sqrt{\frac{1}{2}} P_{1s}(r_1) P_{2p}(r_2) \\ \bar{P}^{L_0}_{ps}(r_1, r_2, \tau = 0) &= -\sqrt{\frac{1}{2}} P_{2p}(r_1) P_{1s}(r_2) \end{aligned} \tag{4.10}$$

for the $1s2p\ ^3P$ term. The bound radial wavefunctions, $P_{nl}(r)$, are obtained by diagonalization of the Hamiltonian, $T_l(r)$, of Eq.(4.3).

The initial condition for the solution of the time-dependent close-coupled equations of Eq.(4.2) is given by:

$$P^{L}_{l_1 l_2}(r_1, r_2, t = 0) = \bar{P}^{L_0}_{l_1 l_2}(r_1, r_2, \tau \to \infty) \delta_{L, L_0} \ . \tag{4.11}$$

Following propagation in real time, momentum space amplitudes are calculated using:

$$\begin{aligned} K^L_{l_1l_2}(k_1,k_2) &= \int_0^\infty dr_1 \int_0^\infty dr_2 P_{k_1l_1}(r_1)P_{k_2l_2}(r_2) \\ &\quad \times P^L_{l_1l_2}(r_1,r_2,t\to\infty)\ , \end{aligned} \tag{4.12}$$

where the continuum radial wavefunctions, $P_{kl}(r)$, are obtained by a distorted-wave solution of the radial Schrodinger equation using $T_l(r)$ of Eq.(4.3). The total double photoionization cross section is given by:

$$\sigma_2 = \frac{\omega}{IT}\int_0^\infty dk_1 \int_0^\infty dk_2 \sum_{l_1l_2L} |K^L_{l_1l_2}(k_1,k_2)|^2\ , \tag{4.13}$$

where T is the total time for the propagation.

4.2.2 TDCC($l_1j_1l_2j_2J$) Method

Expanding the total wavefunction, $\Psi(\vec{r}_1,\vec{r}_2,t)$, in coupled spin-orbit eigenfunctions for each J symmetry and substitution into Eq.(4.1), including the spin-orbit mass-velocity, and Darwin interactions, yields the following time-dependent close-coupled partial differential equations:

$$\begin{aligned} i\frac{\partial P^J_{l_1j_1l_2j_2}(r_1,r_2,t)}{\partial t} &= \sum_{i=1}^{2} T_{l_ij_i}(r_i)P^J_{l_1j_1l_2j_2}(r_1,r_2,t) \\ &\quad + \sum_{l'_1j'_1l'_2j'_2} V^J_{l_1j_1l_2j_2,l'_1j'_1l'_2j'_2}(r_1,r_2)P^J_{l'_1j'_1l'_2j'_2}(r_1,r_2,t) \\ &\quad + \sum_{l'_1j'_1l'_2j'_2J'} W^{JJ'}_{l_1j_1l_2j_2,l'_1j'_1l'_2j'_2}(r_1,t)P^{J'}_{l'_1j'_1l'_2j'_2}(r_1,r_2,t) \\ &\quad + \sum_{l'_1j'_1l'_2j'_2J'} W^{JJ'}_{l_1j_1l_2j_2,l'_1j'_1l'_2j'_2}(r_2,t)P^{J'}_{l'_1j'_1l'_2j'_2}(r_1,r_2,t)\ . \end{aligned} \tag{4.14}$$

For the He case, the kinetic, nuclear, and spin-orbit energy operator is given by:

$$\begin{aligned} T_{l_i j_i}(r_i) &= -\frac{1}{2}\frac{d^2}{dr_i^2} + \frac{l_i(l_i+1)}{2r_i^2} - \frac{Z}{r_i} \\ &\quad + \frac{Z}{4c^2 r_i^3}[j_i(j_i+1) - l_i(l_i+1) - \frac{3}{4}] \ . \end{aligned} \tag{4.15}$$

For the Ne^{8+} case, kinetic, nuclear, spin-orbit, mass-velocity, and Darwin operator is given by:

$$\begin{aligned} T_{l_i j_i}(r_i) &= -\frac{1}{2}\frac{\partial^2}{\partial r_i^2} + \frac{l_i(l_i+1)}{2r_i^2} + V(r_i) \\ &\quad + \frac{1}{4c^2}\frac{[j_i(j_i+1) - l_i(l_i+1) - \frac{3}{4}]}{r_i}\frac{\partial V(r_i)}{\partial r_i} \\ &\quad - \frac{1}{2c^2}[\epsilon_i - V(r_i)]^2 - \frac{1}{4c^2}\frac{\partial V(r_i)}{\partial r_i}[\frac{\partial}{\partial r_i} + \frac{\kappa_i}{r_i}] \ , \end{aligned} \tag{4.16}$$

where $\kappa_i = -(l_i+1)$ for $j_i = l_i + \frac{1}{2}$ and $\kappa_i = +l_i$ for $j_i = l_i - \frac{1}{2}$. The electron-electron interaction energy operator, derived using expressions for the scalar product of two tensor operators and uncoupling formulae for reduced matrix elements[44], is given by:

$$\begin{aligned} V^J_{l_1 j_1 l_2 j_2, l'_1 j'_1 l'_2 j'_2}(r_1, r_2) &= (-1)^{2j'_1 + j_2 + j'_2 + J + 1} \\ &\quad \times \sqrt{(2l_1+1)(2l_2+1)(2l'_1+1)(2l'_2+1)} \\ &\quad \times \sqrt{(2j_1+1)(2j_2+1)(2j'_1+1)(2j'_2+1)} \\ &\quad \times \sum_\lambda \frac{(r_1, r_2)^\lambda_<}{(r_1, r_2)^{\lambda+1}_>} \begin{pmatrix} l_1 & \lambda & l'_1 \\ 0 & 0 & 0 \end{pmatrix} \begin{pmatrix} l_2 & \lambda & l'_2 \\ 0 & 0 & 0 \end{pmatrix} \\ &\quad \times \begin{Bmatrix} l_1 & \frac{1}{2} & j_1 \\ j'_1 & \lambda & l'_1 \end{Bmatrix} \begin{Bmatrix} l_2 & \frac{1}{2} & j_2 \\ j'_2 & \lambda & l'_2 \end{Bmatrix} \\ &\quad \times \begin{Bmatrix} j_1 & j_2 & J \\ j'_2 & j'_1 & \lambda \end{Bmatrix} \ . \end{aligned} \tag{4.17}$$

The radiation field energy operators, derived using the Wigner-Eckart theorem and uncoupling formulae for reduced matrix elements[44], are given by:

$$\begin{aligned}
W^{JJ'}_{l_1 j_1 l_2 j_2, l'_1 j'_1 l'_2 j'_2}(r_1, t) \;&=\; E(t)\cos\omega t \; r_1 \; \delta_{l_2,l'_2}\delta_{j_2,j'_2} \\
&\times(-1)^{j_1+j'_1+j_2+J+J'-M+\frac{1}{2}}\sqrt{(2J+1)(2J'+1)} \\
&\times\sqrt{(2l_1+1)(2l'_1+1)(2j_1+1)(2j'_1+1)} \\
&\times\begin{pmatrix} l_1 & 1 & l'_1 \\ 0 & 0 & 0 \end{pmatrix}\begin{pmatrix} J & 1 & J' \\ -M & 0 & M' \end{pmatrix} \\
&\times\begin{Bmatrix} j_1 & j_2 & J \\ J' & 1 & j'_1 \end{Bmatrix}\begin{Bmatrix} l_1 & \frac{1}{2} & j_1 \\ j'_1 & 1 & l'_1 \end{Bmatrix}
\end{aligned} \qquad (4.18)$$

and

$$\begin{aligned}
W^{JJ'}_{l_1 j_1 l_2 j_2, l'_1 j'_1 l'_2 j'_2}(r_2, t) \;&=\; E(t)\cos\omega t \; r_2 \; \delta_{l_1,l'_1}\delta_{j_1,j'_1} \\
&\times(-1)^{j_1+2j'_2+2J-M+\frac{1}{2}}\sqrt{(2J+1)(2J'+1)} \\
&\times\sqrt{(2l_2+1)(2l'_2+1)(2j_2+1)(2j'_2+1)} \\
&\times\begin{pmatrix} l_2 & 1 & l'_2 \\ 0 & 0 & 0 \end{pmatrix}\begin{pmatrix} J & 1 & J' \\ -M & 0 & M' \end{pmatrix} \\
&\times\begin{Bmatrix} j_1 & j_2 & J \\ 1 & J' & j'_2 \end{Bmatrix}\begin{Bmatrix} l_2 & \frac{1}{2} & j_2 \\ j'_2 & 1 & l'_2 \end{Bmatrix} .
\end{aligned} \qquad (4.19)$$

We assume $M = M' = 0$ in Eqs.(4.18) and (4.19).

The close-coupling partial differential equations for relaxation in imaginary time of a two-electron atom are given by:

$$\begin{aligned}
-\frac{\partial \bar{P}^{J_0}_{l_1 j_1 l_2 j_2}(r_1, r_2, \tau)}{\partial \tau} &= \sum_{i=1}^{2} T_{l_i j_i}(r_i) \bar{P}^{J_0}_{l_1 j_1 l_2 j_2}(r_1, r_2, \tau) \\
&+ \sum_{l_1' j_1' l_2' j_2'} V^{J_0}_{l_1 j_1 l_2 j_2, l_1' j_1' l_2' j_2'}(r_1, r_2) \bar{P}^{J_0}_{l_1' j_1' l_2' j_2'}(r_1, r_2, \tau) \ . \qquad (4.20)
\end{aligned}$$

The initial conditions for the solution of Eq.(4.20) are given by:

$$\bar{P}^{J_0}_{s\frac{1}{2}s\frac{1}{2}}(r_1, r_2, \tau = 0) = P_{1s\frac{1}{2}}(r_1) P_{1s\frac{1}{2}}(r_2) \qquad (4.21)$$

for the $1s^2\ {}^1S_0$ level,

$$\bar{P}^{J_0}_{s\frac{1}{2}s\frac{1}{2}}(r_1, r_2, \tau = 0) = \sqrt{\frac{1}{2}} P_{1s\frac{1}{2}}(r_1) P_{2s\frac{1}{2}}(r_2) - \sqrt{\frac{1}{2}} P_{2s\frac{1}{2}}(r_1) P_{1s\frac{1}{2}}(r_2) \qquad (4.22)$$

for the $1s2s\ {}^3S_1$ level,

$$\begin{aligned}
\bar{P}^{J_0}_{s\frac{1}{2}p\frac{1}{2}}(r_1, r_2, \tau = 0) &= +\sqrt{\frac{1}{2}} P_{1s\frac{1}{2}}(r_1) P_{2p\frac{1}{2}}(r_2) \\
\bar{P}^{J_0}_{p\frac{1}{2}s\frac{1}{2}}(r_1, r_2, \tau = 0) &= +\sqrt{\frac{1}{2}} P_{2p\frac{1}{2}}(r_1) P_{1s\frac{1}{2}}(r_2) \qquad (4.23)
\end{aligned}$$

for the $1s2p\ {}^3P_0$ level,

$$\begin{aligned}
\bar{P}^{J_0}_{s\frac{1}{2}p\frac{1}{2}}(r_1, r_2, \tau = 0) &= +\sqrt{\frac{1}{4}} P_{1s\frac{1}{2}}(r_1) P_{2p\frac{1}{2}}(r_2) \\
\bar{P}^{J_0}_{p\frac{1}{2}s\frac{1}{2}}(r_1, r_2, \tau = 0) &= +\sqrt{\frac{1}{4}} P_{2p\frac{1}{2}}(r_1) P_{1s\frac{1}{2}}(r_2) \\
\bar{P}^{J_0}_{s\frac{1}{2}p\frac{3}{2}}(r_1, r_2, \tau = 0) &= +\sqrt{\frac{1}{4}} P_{1s\frac{1}{2}}(r_1) P_{2p\frac{3}{2}}(r_2) \\
\bar{P}^{J_0}_{p\frac{3}{2}s\frac{1}{2}}(r_1, r_2, \tau = 0) &= +\sqrt{\frac{1}{4}} P_{2p\frac{3}{2}}(r_1) P_{1s\frac{1}{2}}(r_2) \qquad (4.24)
\end{aligned}$$

for the $1s2p\ ^3P_1$ level, and

$$\begin{aligned}
\bar{P}^{J_0}_{s\frac{1}{2}p\frac{3}{2}}(r_1, r_2, \tau = 0) &= +\sqrt{\frac{1}{2}} P_{1s\frac{1}{2}}(r_1) P_{2p\frac{3}{2}}(r_2) \\
\bar{P}^{J_0}_{p\frac{3}{2}s\frac{1}{2}}(r_1, r_2, \tau = 0) &= -\sqrt{\frac{1}{2}} P_{2p\frac{3}{2}}(r_1) P_{1s\frac{1}{2}}(r_2)
\end{aligned} \tag{4.25}$$

for the $1s2p\ ^3P_2$ level. The bound radial wavefunctions, $P_{nlj}(r)$, are obtained by diagonalization of the Hamiltonian, $T_{lj}(r)$, of Eq.(4.15). For the Ne^{8+} case, all the bound and continuum energies and wavefunctions are then corrected in first order perturbation theory using:

$$V_{mv}(r) = -\frac{1}{2c^2}(\epsilon - V(r))^2 \tag{4.26}$$

for the mass-velocity interaction[44] and

$$V_D(r) = -\frac{1}{4c^2}\frac{\partial V(r)}{\partial r}\left(\frac{\partial}{\partial r} + \frac{\kappa}{r}\right)\delta_{\kappa,-1} \tag{4.27}$$

for the Darwin interaction[44].

The initial condition for the solution of the time-dependent close-coupled equations of Eq.(4.14) is given by:

$$P^J_{l_1j_1l_2j_2}(r_1, r_2, t = 0) = \bar{P}^{J_0}_{l_1j_1l_2j_2}(r_1, r_2, \tau \to \infty)\delta_{J,J_0} \ . \tag{4.28}$$

Following propagation in real time, momentum space amplitudes are calculated using:

$$\begin{aligned}
K^J_{l_1j_1l_2j_2}(k_1, k_2) &= \int_0^\infty dr_1 \int_0^\infty dr_2 P_{k_1l_1j_1}(r_1) P_{k_2l_2j_2}(r_2) \\
&\quad \times P^J_{l_1j_1l_2j_2}(r_1, r_2, t \to \infty) \ ,
\end{aligned} \tag{4.29}$$

where the continuum radial wavefunctions, $P_{klj}(r)$, are obtained by a distorted-wave solution of the radial Schrodinger equation using $T_{lj}(r)$ of Eq.(4.15) for the He case. For the Ne^{8+}

case, the continuum radial wavefunctions, $P_{klj}(r)$, are obtained by diagonalization of the hamiltonian below:

$$H(r) = -\frac{1}{2}\frac{\partial^2}{\partial r^2} + \frac{l(l+1)}{2r^2} + V(r) + V_{so}(r) \ , \tag{4.30}$$

where

$$V_{so}(r) = \frac{1}{4c^2}\frac{(j(j+1) - l(l+1) - \frac{3}{4})}{r}\frac{\partial V(r)}{\partial r} \tag{4.31}$$

and the application of lowest order perturbation theory using Eqs.(4.26) and (4.27). The total double photoionization cross section is given by:

$$\sigma_2 = \frac{\omega}{IT}\int_0^\infty dk_1 \int_0^\infty dk_2 \sum_{l_1 j_1 l_2 j_2 J} |K^J_{l_1 j_1 l_2 j_2}(k_1, k_2)|^2 \ , \tag{4.32}$$

where T is again the total time for the propagation.

4.3 Results

Double photoionization cross sections for ground and excited states of He are calculated using the TDCC($l_1 l_2 L$) and TDCC($l_1 j_1 l_2 j_2 J$) methods. A lattice of 360 × 360 points is used with a uniform grid spacing of $\Delta r_1 = \Delta r_2 = 0.20$ and including up to $l \leq 3$ (see Tables 4.1-4.2) or $lj \leq 3\frac{7}{2}$ (see Tables 4.3-4.7) angular momenta. For more accurate cross sections a lattice of 720 × 720 points is used with a uniform grid spacing of $\Delta r_1 = \Delta r_2 = 0.10$ and including up to $l \leq 5$ or $lj \leq 5\frac{11}{2}$ angular momenta.

4.3.1 $1s^2$ ground configuration of He

Double photoionization cross sections for the $1s^2$ ^1S term of He are calculated using the TDCC($l_1 l_2 L$) method. Relaxation on the lattice using Eq.(4.7), the initial condition of Eq.(4.8), and the 4 $L = 0$ coupled channels found in Table 4.1 yields a ground state of He with an energy of $E =$ -75.8 eV for the 360 × 360 lattice. Propagation on the lattice using Eq.(4.2) with the 10 $L =$ 0,1 coupled channels found in Table 4.1 yields the total double photoionization cross sections using Eq.(4.13) found in Figure 4.1. At a photon energy of 100 eV the cross section is found to peak at a value of 8.86 kb. Relaxation on the lattice with 6 $L = 0$ coupled channels yields a ground state of He with an energy of $E =$ -78.2 eV for the 720 × 720 lattice. Propagation on the lattice with 16 $L =$ 0,1 coupled channels yields the total double photoionization cross sections found in Figure 4.1. At a photon energy of 105 eV the cross section is found to peak at a value of 8.73 kb. We note that experimental measurements[59] find a peak cross section of 8.81 ± 0.4 kb at a photon energy of 102 eV.

Double photoionization cross sections for the $1s^2$ $^1S_0$ level of He are calculated using the TDCC($l_1 j_1 l_2 j_2 J$) method. Relaxation on the lattice using Eq.(4.20), the initial condition of Eq.(4.21), and the 7 $J = 0$ coupled channels found in Table 4.3 yields a ground state of He with an energy of $E =$ -75.8 eV for the 360 × 360 lattice. Propagation on the lattice using Eq.(4.14) with the 23 $J =$ 0,1 coupled channels found in Table 4.3 yields the total double photoionization cross sections using Eq.(4.32) found in Figure 4.1. The cross sections at the

3 photon energies are in good agreement with the TDCC(l_1l_2L) results for the 360 × 360 lattice. Relaxation on the lattice with 11 $J = 0$ coupled channels yields a ground state of He with an energy of E = -78.2 eV for the 720 × 720 lattice. Propagation on the lattice with 39 J = 0,1 coupled channels yields the total double photoionization cross sections found in Figure 4.1. The cross sections at the 3 photon energies are in good agreement with the TDCC(l_1l_2L) results for the 720 × 720 lattice.

4.3.2 $1s2s$ excited configuration of He

Double photoionization cross sections for the $1s2s\ ^3S$ term of He are calculated using the TDCC(l_1l_2L) method. Relaxation on the lattice using Eq.(4.7), the initial condition of Eq.(4.9), and the 4 $L = 0$ coupled channels found in Table 4.1 yields an excited state of He with an energy E = -57.1 eV for the 360 × 360 lattice. Propagation on the lattice using Eq.(4.2) with the 10 L = 0,1 coupled channels found in Table 4.1 yields the total double photoionization cross sections using Eq.(4.13) found in Figure 4.2. At a photon energy of 70 eV the cross section is found to peak at a value of 1.95 kb. Relaxation on the lattice with 6 $L = 0$ coupled channels yields an excited state of He with an energy of E = -58.6 eV for the 720 × 720 lattice. Propagation on the lattice with 16 L = 0,1 coupled channels yields the total double photoionization cross sections found in Figure 4.2. At a photon energy of 75 eV the cross section is found to peak at a value of 2.47 kb.

Double photoionization cross sections for the $1s2s\ ^3S_1$ level of He are calculated using the TDCC($l_1j_1l_2j_2J$) method. Relaxation on the lattice using Eq.(4.20), the initial condition of Eq.(4.22), and the 17 $J = 1$ coupled channels found in Table 4.4 yields an excited state of He with an energy of E = -57.1 eV for the 360 × 360 lattice. Propagation on the lattice using Eq.(4.14) with the 43 J = 1,0,2 coupled channels found in Table 4.4 yields the total double photoionization cross sections using Eq.(4.32) found in Figure 4.2. The cross sections at the 3 photon energies are in good agreement with the TDCC l_1l_2L results for the 360 × 360 lattice. Relaxation on the lattice with 29 $J = 1$ coupled channels yields an excited state of He with an energy of E = -58.6 eV for the 720 × 720 lattice. Propagation on the lattice with 79 J = 1,0,2 coupled channels yields the total double photoionization cross sections found in Figure 4.2. The cross sections at the 3 photon energies are in good agreement with the TDCC(l_1l_2L) results for the 720 × 720 lattice.

4.3.3 $1s2p$ excited configuration of He

Double photoionization cross sections for the $1s2p\ ^3P$ term of He are calculated using the TDCC(l_1l_2L) method. Relaxation on the lattice using Eq.(4.7), the initial condition of Eq.(4.10), and the 6 L = 1 coupled channels found in Table 4.2 yields an excited state of He with an energy E = -56.1 eV for the 360 × 360 lattice. Propagation on the lattice using Eq.(4.2) with the 17 L = 1,0,2 coupled channels found in Table 4.2 yields the total double photoionization cross sections using Eq.(4.13) found in Figure 4.3. At a photon energy of 75 eV the cross section is found to peak at a value of 2.38 kb. Relaxation on the lattice with 10 L = 1 coupled channels yields an excited state of He with an energy E = -57.5 eV for the 720 × 720 lattice. Propagation on the lattice with 29 L = 1,0,2 coupled channels yields the total double photoionization cross sections found in Figure 4.4. At a photon energy of 75.0 eV the cross section is found to peak at 3.59 kb.

Double photoionization cross sections for the $1s2p\ ^3P_0$ level of He are calculated using the TDCC($l_1j_1l_2j_2J$) method. Relaxation on the lattice using Eq.(4.20), the initial condition of Eq.(4.23), and the 6 J = 0 coupled channels found in Table 4.5 yields an excited state of He with an energy E = -56.1 eV for the 360 × 360 lattice. Propagation on the lattice using Eq.(4.14) with the 23 J = 0,1 coupled channels found in Table 4.5 yields the total double photoionization cross sections using Eq.(4.32) found in Figure 4.3 The cross sections at the 9 photon energies are above the TDCC(l_1l_2L) results at the lower photon energies for the 360 × 360 lattice. At a photon energy of 65.0 eV the cross section is found to peak at a value of 3.66 kb. Relaxation on the lattice with 10 J = 0 coupled channels yields an excited state of He with an energy E = -57.5 eV for the 720 × 720 lattice. Propagation on the lattice with

39 J = 0,1 coupled channels yields the total double photoionization cross sections found in Figure 4.4. The cross sections at the 9 photon energies are above the TDCC(l_1l_2L) results at the lower photon energies for the 720 × 720 lattice. At a photon energy of 70.0 eV the cross section is found to peak at a value of 4.55 kb.

Double photoionization cross sections for the $1s2p\ ^3P_1$ level of He are calculated using the TDCC($l_1j_1l_2j_2J$) method. Relaxation on the lattice using Eq.(4.20), the initial condition of Eq.(4.24), and the 16 J = 1 coupled channels found in Table 4.6 yields an excited state with an energy E = -56.1 eV for the 360 × 360 lattice. Propagation on the lattice using Eq.(4.14) with the 44 J = 1,0,2 coupled channels found in Table 4.6 yields the double photoionization cross sections using Eq.(4.32) found in Figure 4.3. The cross sections at the 9 photon energies are above the TDCC(l_1l_2L) results at the lower photon energies for the 360 × 360 lattice. At a photon energy of 70.0 eV the cross section is found to peak at a value of 3.31 kb. Relaxation on the lattice with 28 J = 1 coupled channels yields an excited state of He with an energy E = -57.5 eV for the 720 × 720 lattice. Propagation on the lattice with 80 J = 1,0,2 coupled channels yields the total photoionization cross sections found in Figure 4.4. The cross sections at the 9 photon energies are above the TDCC(l_1l_2L) results at the lower photon energies for the 720 × 720 lattice. At a photon energy of 70.0 eV the cross section is found to peak at a value of 4.45 kb.

Double photoionization cross sections for the $1s2p\ ^3P_2$ level of He are calculated using the TDCC($l_1j_1l_2j_2J$) method. Relaxation on the lattice using Eq.(4.20), the initial condition of Eq.(4.25), and the 20 J = 2 coupled channels found in Table 4.7 yields an excited state of He with an energy E = -56.1 eV for the 360 × 360 lattice. Propagation on the lattice using Eq.(4.14) with the 56 J = 2,1,3 coupled channels found in Table 4.7 yields the total double photoionization cross sections using Eq.(4.32) found in Figure 4.3. The cross sections at the 9 photon energies are above the TDCC(l_1l_2L) results at the lower photon energies for the 360 × 360 lattice. At a photon energy of 70.0 eV the cross section is found to peak at a value of 2.99 kb. Relaxation on the lattice with 40 J = 2 coupled channels yields an excited state of He with an energy E = -57.5 eV for the 720 × 720 lattice. Propagation on the lattice with 116 J = 2,1,3 coupled channels yields the total double photoionization cross sections found in Figure 4.4. The cross sections at the 9 photon energies are above the TDCC($l_1 l_2 L$) results at the lower photon energies for the 720 × 720 lattice. At a photon energy of 75.0 eV the cross section is found to peak at a value of 3.96 kb.

4.3.4 Averages over terms and levels for He

Since for the $1s^2$ ground configuration there is only one ^1S term and $^1S_0$ level, we find the double photoionization cross sections to be the same for both the $\Delta r_i = 0.20$ and $\Delta r_i = 0.10$ lattices, as shown in Figure 4.1.

For the $1s2s$ excited configuration there are two ^3S and ^1S terms, as well as two $^3S_1$ and $^1S_0$ levels. Since the ^3S term and the $^3S_1$ level pair off exactly, we find the double photoionization cross sections to be the same for both the $\Delta r_i = 0.20$ and $\Delta r_i = 0.10$ lattices, as shown in Figure 4.2.

For the $1s2p$ excited configuration there are two ^3P and ^1P terms, as well as four $^3P_0$, $^3P_1$, $^3P_2$, and $^1P_1$ levels. Additional TDCC($l_1 l_2 L$) calculations for the ^1P term of He and TDCC($l_1 j_1 l_2 j_2 J$) calculations for the $^1P_1$ level of He were made on the 360 × 360 lattice. Average term cross sections are given by:

$$\sigma^{avg}_{term} = \frac{3}{4}\sigma(^3P) + \frac{1}{4}\sigma(^1P) \ , \tag{4.33}$$

while average level cross sections are given by:

$$\sigma^{avg}_{level} = \frac{1}{12}\sigma(^3P_0) + \frac{3}{12}\sigma(^3P_1) + \frac{5}{12}\sigma(^3P_2) + \frac{3}{12}\sigma(^1P_1) \ . \tag{4.34}$$

The average double photoionization cross sections for the $1s2p$ excited configuration are found to be in good agreement, as shown in Figure 4.5.

4.3.5 $1s^2$ ground configuration of Ne^{8+}

Double photoionization cross sections for the ground state of Ne^{8+} are calculated using the non-relativistic and semi-relativistic TDCC methods. A lattice of 720 × 720 points is used with a uniform grid spacing of $\Delta r_1 = \Delta r_2 = 0.01$ and including up to $l \leq 5$ or $lj \leq 5\frac{11}{2}$ coupled channel angular momenta.

Double photoionization cross sections for the $1s^2\ {}^1S$ term of Ne^{8+} are calculated using the non-relativistic TDCC method. Relaxation on the lattice with the 6 $L = 0$ coupled channels found in Table 4.8 yields a ground state of Ne^{8+} with an energy of E = -2549 eV. Propagation on the lattice with the 16 $L = 0{,}1$ coupled channels found in Table 4.8 yields the total double photoionization cross sections found in Figure 4.6. At a photon energy of 3500 eV the cross section is found to peak at a value of 12.4 b.

Double photoionization cross sections for the $1s^2\ {}^1S_0$ level of Ne^{8+} are calculated using the semi-relativistic TDCC method. Relaxation on the lattice with the 11 $J = 0$ coupled channels found in Table 4.9 yields a ground state of Ne^{8+} with an energy of E = -2559 eV, in good agreement with the NIST recommended value of E = -2558 eV [41]. Propagation on the lattice with the 39 $J = 0{,}1$ coupled channels found in Table 4.9 yields the total double photoionization cross sections found in Figure 4.6. The cross sections at the 6 photon energies are slightly above the non-relativistic TDCC results.

4.4 Summary

A time-dependent close-coupling method was developed that includes the spin-orbit interaction through the use of a $l_1 j_1 l_2 j_2 J$ coupling scheme. Double photoionization cross sections for the He atom were then calculated for the $1s^2\ ^1S_0$, $1s2s\ ^3S_1$, and $1s2p\ ^3P_{0,1,2}$ levels. Lattices with 360 × 360 points, a uniform grid spacing of $\Delta r_i = 0.20$, and $lj \leq 3\frac{7}{2}$ angular momenta, and with 720 × 720 points, a uniform grid spacing of $\Delta r_i = 0.10$, and $lj \leq 5\frac{11}{2}$ angular momenta were both used. Good agreement was found between the TDCC($l_1 j_1 l_2 j_2 J$) calculations for the $1s^2\ ^1S_0$ level and the TDCC($l_1 l_2 L$) calculations for the $1s^2\ ^1S$ term, as well as between the TDCC($l_1 j_1 l_2 j_2 J$) calculations for the $1s2s\ ^3S_1$ level and the TDCC($l_1 l_2 L$) calculations for the $1s2s\ ^3S$ term. The TDCC($l_1 j_1 l_2 j_2 j$) calculations for the $1s2p\ ^3P_{0,1,2}$ levels were all found to peak higher than the TDCC($l_1 l_2 L$) calculations for the $1s2p\ ^3P$ term, with the $1s2p\ ^3P_0$ level having the highest peak cross section on both the 360 × 360 point and the 720 × 720 point lattices. However, good agreement was found between the TDCC($l_1 l_2 L$) results for the average of the $1s2p\ ^3P$ and $1s2p\ ^1P$ terms and the TDCC($l_1 j_1 l_2 j_2 J$) results for the average of the $1s2p\ ^3P_{0,1,2}$ and $1s2p\ ^1P_1$ levels on the 360 × 360 point lattice.

A semi-relativistic time-dependent close-coupling method was developed that includes the spin-orbit, mass-velocity, and Darwin interactions through the use of a $l_1 j_1 l_2 j_2 J$ coupling scheme. Double photoionization cross sections for the Ne^{8+} atomic ion were calculated for the $1s^2\ ^1S_0$ level. A lattice with 720 × 720 points, a uniform grid spacing of $\Delta r_i = 0.01$, and $lj \leq 5\frac{11}{2}$ coupled channel angular momenta was used. The semi-relativistic TDCC calculations for the $1s^2\ ^1S_0$ level were found to be slightly above the non-relativistic TDCC calculations for the $1s^2\ ^1S$ term.

In the future, we plan to continue the application of TDCC method based on a $l_1 j_1 l_2 j_2 J$ coupling scheme. Although experimental observation of differences in double photoionization cross sections for the $1s2p\ ^3P_{0,1,2}$ excited levels of He are difficult due to the extremely small fine structure splitting, the possibilities of comparing theory with experiment could be greater for the $1s^2 2s^2 2p^2\ ^3P_{0,1,2}$ ground state levels of Carbon or heavier systems. We note that for more highly charged atomic ions, like Kr^{34+}, that the semi-relativistic TDCC method fails and one must use a fully-relativistic TDCC method[60]. Thus, we plan to apply the semi-relativistic TDCC method to the outer subshells of alkaline atoms and their low charged ions in the calculation of total and differential cross sections for single photon and two-photon double ionization to compare with new experimental measurements.

Table 4.1: TDCC l_1l_2L coupled channels for the $1s^2\ ^1S$ and the $1s2s\ ^3S$ terms of He

channel	(l_1, l_2)	L	channel	(l_1, l_2)	L
1	s, s	0	1	s, p	1
2	p, p	0	2	p, s	1
3	d, d	0	3	p, d	1
4	f, f	0	4	d, p	1
			5	d, f	1
			6	f, d	1

Table 4.2: TDCC l_1l_2L coupled channels for the $1s2p\ ^3P$ term of He

channel	(l_1, l_2)	L	channel	(l_1, l_2)	L	channel	(l_1, l_2)	L
1	s, p	1	1	s, s	0	1	s, d	2
2	p, s	1	2	p, p	0	2	d, s	2
3	p, d	1	3	d, d	0	3	p, p	2
4	d, p	1	4	f, f	0	4	p, f	2
5	d, f	1				5	f, p	2
6	f, d	1				6	d, d	2
						7	f, f	2

Table 4.3: TDCC $l_1j_1l_2j_2J$ coupled channels for the $1s^2\ ^1S_0$ level of He

channel	(l_1j_1, l_2j_2)	J	channel	(l_1j_1, l_2j_2)	J
1	$s\frac{1}{2},\ s\frac{1}{2}$	0	1	$s\frac{1}{2},\ p\frac{1}{2}$	1
2	$p\frac{1}{2},\ p\frac{1}{2}$	0	2	$p\frac{1}{2},\ s\frac{1}{2}$	1
3	$p\frac{3}{2},\ p\frac{3}{2}$	0	3	$s\frac{1}{2},\ p\frac{3}{2}$	1
4	$d\frac{3}{2},\ d\frac{3}{2}$	0	4	$p\frac{3}{2},\ s\frac{1}{2}$	1
5	$d\frac{5}{2},\ d\frac{5}{2}$	0	5	$p\frac{1}{2},\ d\frac{3}{2}$	1
6	$f\frac{5}{2},\ f\frac{5}{2}$	0	6	$d\frac{3}{2},\ p\frac{1}{2}$	1
7	$f\frac{7}{2},\ f\frac{7}{2}$	0	7	$p\frac{3}{2},\ d\frac{3}{2}$	1
			8	$d\frac{3}{2},\ p\frac{3}{2}$	1
			9	$p\frac{3}{2},\ d\frac{5}{2}$	1
			10	$d\frac{5}{2},\ p\frac{3}{2}$	1
			11	$d\frac{3}{2},\ f\frac{5}{2}$	1
			12	$f\frac{5}{2},\ d\frac{3}{2}$	1
			13	$d\frac{5}{2},\ f\frac{5}{2}$	1
			14	$f\frac{5}{2},\ d\frac{5}{2}$	1
			15	$d\frac{5}{2},\ f\frac{7}{2}$	1
			16	$f\frac{7}{2},\ d\frac{5}{2}$	1

Table 4.4: TDCC $l_1 j_1 l_2 j_2 J$ coupled channels for the $1s2s\ {}^3S_1$ level of He

channel	$(l_1 j_1, l_2 j_2)$	J	channel	$(l_1 j_1, l_2 j_2)$	J	channel	$(l_1 j_1, l_2 j_2)$	J
1	$s\frac{1}{2}$, $s\frac{1}{2}$	1	1	$s\frac{1}{2}$, $p\frac{1}{2}$	0	1	$s\frac{1}{2}$, $p\frac{3}{2}$	2
2	$s\frac{1}{2}$, $d\frac{3}{2}$	1	2	$p\frac{1}{2}$, $s\frac{1}{2}$	0	2	$p\frac{3}{2}$, $s\frac{1}{2}$	2
3	$d\frac{3}{2}$, $s\frac{1}{2}$	1	3	$p\frac{3}{2}$, $d\frac{3}{2}$	0	3	$s\frac{1}{2}$, $f\frac{5}{2}$	2
4	$p\frac{1}{2}$, $p\frac{1}{2}$	1	4	$d\frac{3}{2}$, $p\frac{3}{2}$	0	4	$f\frac{5}{2}$, $s\frac{1}{2}$	2
5	$p\frac{1}{2}$, $p\frac{3}{2}$	1	5	$d\frac{5}{2}$, $f\frac{5}{2}$	0	5	$p\frac{1}{2}$, $d\frac{3}{2}$	2
6	$p\frac{3}{2}$, $p\frac{1}{2}$	1	6	$f\frac{5}{2}$, $d\frac{5}{2}$	0	6	$d\frac{3}{2}$, $p\frac{1}{2}$	2
7	$p\frac{3}{2}$, $p\frac{3}{2}$	1				7	$p\frac{1}{2}$, $d\frac{5}{2}$	2
8	$p\frac{3}{2}$, $f\frac{5}{2}$	1				8	$d\frac{5}{2}$, $p\frac{1}{2}$	2
9	$f\frac{5}{2}$, $p\frac{3}{2}$	1				9	$p\frac{3}{2}$, $d\frac{3}{2}$	2
10	$d\frac{3}{2}$, $d\frac{3}{2}$	1				10	$d\frac{3}{2}$, $p\frac{3}{2}$	2
11	$d\frac{3}{2}$, $d\frac{5}{2}$	1				11	$p\frac{3}{2}$, $d\frac{5}{2}$	2
12	$d\frac{5}{2}$, $d\frac{3}{2}$	1				12	$d\frac{5}{2}$, $p\frac{3}{2}$	2
13	$d\frac{5}{2}$, $d\frac{5}{2}$	1				13	$d\frac{3}{2}$, $f\frac{5}{2}$	2
14	$f\frac{5}{2}$, $f\frac{5}{2}$	1				14	$f\frac{5}{2}$, $d\frac{3}{2}$	2
15	$f\frac{5}{2}$, $f\frac{7}{2}$	1				15	$d\frac{3}{2}$, $f\frac{7}{2}$	2
16	$f\frac{7}{2}$, $f\frac{5}{2}$	1				16	$f\frac{7}{2}$, $d\frac{3}{2}$	2
17	$f\frac{7}{2}$, $f\frac{7}{2}$	1				17	$d\frac{5}{2}$, $f\frac{5}{2}$	2
						18	$f\frac{5}{2}$, $d\frac{5}{2}$	2
						19	$d\frac{5}{2}$, $f\frac{7}{2}$	2
						20	$f\frac{7}{2}$, $d\frac{5}{2}$	2

Table 4.5: TDCC $l_1j_1l_2j_2J$ coupled channels for the $1s2p\ {}^3P_0$ level of He

channel	(l_1j_1, l_2j_2)	J	channel	(l_1j_1, l_2j_2)	J
1	$s\frac{1}{2},\ p\frac{1}{2}$	0	1	$s\frac{1}{2},\ s\frac{1}{2}$	1
2	$p\frac{1}{2},\ s\frac{1}{2}$	0	2	$s\frac{1}{2},\ d\frac{3}{2}$	1
3	$p\frac{3}{2},\ d\frac{3}{2}$	0	3	$d\frac{3}{2},\ s\frac{1}{2}$	1
4	$d\frac{3}{2},\ p\frac{3}{2}$	0	4	$p\frac{1}{2},\ p\frac{1}{2}$	1
5	$d\frac{5}{2},\ f\frac{5}{2}$	0	5	$p\frac{1}{2},\ p\frac{3}{2}$	1
6	$f\frac{5}{2},\ d\frac{5}{2}$	0	6	$p\frac{3}{2},\ p\frac{1}{2}$	1
			7	$p\frac{3}{2},\ p\frac{3}{2}$	1
			8	$p\frac{3}{2},\ f\frac{5}{2}$	1
			9	$f\frac{5}{2},\ p\frac{3}{2}$	1
			10	$d\frac{3}{2},\ d\frac{3}{2}$	1
			11	$d\frac{3}{2},\ d\frac{5}{2}$	1
			12	$d\frac{5}{2},\ d\frac{3}{2}$	1
			13	$d\frac{5}{2},\ d\frac{5}{2}$	1
			14	$f\frac{5}{2},\ f\frac{5}{2}$	1
			15	$f\frac{5}{2},\ f\frac{7}{2}$	1
			16	$f\frac{7}{2},\ f\frac{5}{2}$	1
			17	$f\frac{7}{2},\ f\frac{7}{2}$	1

Table 4.6: TDCC $l_1 j_1 l_2 j_2 J$ coupled channels for the $1s2p\ {}^3P_1$ level of He

channel	$(l_1 j_1, l_2 j_2)$	J	channel	$(l_1 j_1, l_2 j_2)$	J	channel	$(l_1 j_1, l_2 j_2)$	J
1	$s\frac{1}{2},\ p\frac{1}{2}$	1	1	$s\frac{1}{2},\ s\frac{1}{2}$	0	1	$s\frac{1}{2},\ d\frac{3}{2}$	2
2	$p\frac{1}{2},\ s\frac{1}{2}$	1	2	$p\frac{1}{2},\ p\frac{1}{2}$	0	2	$d\frac{3}{2},\ s\frac{1}{2}$	2
3	$s\frac{1}{2},\ p\frac{3}{2}$	1	3	$p\frac{3}{2},\ p\frac{3}{2}$	0	3	$s\frac{1}{2},\ d\frac{5}{2}$	2
4	$p\frac{3}{2},\ s\frac{1}{2}$	1	4	$d\frac{3}{2},\ d\frac{3}{2}$	0	4	$d\frac{5}{2},\ s\frac{1}{2}$	2
5	$p\frac{1}{2},\ d\frac{3}{2}$	1	5	$d\frac{5}{2},\ d\frac{5}{2}$	0	5	$p\frac{1}{2},\ p\frac{3}{2}$	2
6	$d\frac{3}{2},\ p\frac{1}{2}$	1	6	$f\frac{5}{2},\ f\frac{5}{2}$	0	6	$p\frac{3}{2},\ p\frac{1}{2}$	2
7	$p\frac{3}{2},\ d\frac{3}{2}$	1	7	$f\frac{7}{2},\ f\frac{7}{2}$	0	7	$p\frac{1}{2},\ f\frac{5}{2}$	2
8	$d\frac{3}{2},\ p\frac{3}{2}$	1				8	$f\frac{5}{2},\ p\frac{1}{2}$	2
9	$p\frac{3}{2},\ d\frac{5}{2}$	1				9	$p\frac{3}{2},\ p\frac{3}{2}$	2
10	$d\frac{5}{2},\ p\frac{3}{2}$	1				10	$p\frac{3}{2},\ f\frac{5}{2}$	2
11	$d\frac{3}{2},\ f\frac{5}{2}$	1				11	$f\frac{5}{2},\ p\frac{3}{2}$	2
12	$f\frac{5}{2},\ d\frac{3}{2}$	1				12	$p\frac{3}{2},\ f\frac{7}{2}$	2
13	$d\frac{5}{2},\ f\frac{5}{2}$	1				13	$f\frac{7}{2},\ p\frac{3}{2}$	2
14	$f\frac{5}{2},\ d\frac{5}{2}$	1				14	$d\frac{3}{2},\ d\frac{3}{2}$	2
15	$d\frac{5}{2},\ f\frac{7}{2}$	1				15	$d\frac{3}{2},\ d\frac{5}{2}$	2
16	$f\frac{7}{2},\ d\frac{5}{2}$	1				16	$d\frac{5}{2},\ d\frac{3}{2}$	2
						17	$d\frac{5}{2},\ d\frac{5}{2}$	2
						18	$f\frac{5}{2},\ f\frac{5}{2}$	2
						19	$f\frac{5}{2},\ f\frac{7}{2}$	2
						20	$f\frac{7}{2},\ f\frac{5}{2}$	2
						21	$f\frac{7}{2},\ f\frac{7}{2}$	2

Table 4.7: TDCC $l_1 j_1 l_2 j_2 J$ coupled channels for the $1s2p\ ^3P_2$ level of He

channel	$(l_1 j_1, l_2 j_2)$	J	channel	$(l_1 j_1, l_2 j_2)$	J	channel	$(l_1 j_1, l_2 j_2)$	J
1	$s\frac{1}{2},\ p\frac{3}{2}$	2	1	$s\frac{1}{2},\ s\frac{1}{2}$	1	1	$s\frac{1}{2},\ d\frac{5}{2}$	3
2	$p\frac{3}{2},\ s\frac{1}{2}$	2	2	$s\frac{1}{2},\ d\frac{3}{2}$	1	2	$d\frac{5}{2},\ s\frac{1}{2}$	3
3	$s\frac{1}{2},\ f\frac{5}{2}$	2	3	$d\frac{3}{2},\ s\frac{1}{2}$	1	3	$p\frac{1}{2},\ f\frac{5}{2}$	3
4	$f\frac{5}{2},\ s\frac{1}{2}$	2	4	$p\frac{1}{2},\ p\frac{1}{2}$	1	4	$f\frac{5}{2},\ p\frac{1}{2}$	3
5	$p\frac{1}{2},\ d\frac{3}{2}$	2	5	$p\frac{1}{2},\ p\frac{3}{2}$	1	5	$p\frac{1}{2},\ f\frac{7}{2}$	3
6	$d\frac{3}{2},\ p\frac{1}{2}$	2	6	$p\frac{3}{2},\ p\frac{1}{2}$	1	6	$f\frac{7}{2},\ p\frac{1}{2}$	3
7	$p\frac{1}{2},\ d\frac{5}{2}$	2	7	$p\frac{3}{2},\ p\frac{3}{2}$	1	7	$p\frac{3}{2},\ p\frac{3}{2}$	3
8	$d\frac{5}{2},\ p\frac{1}{2}$	2	8	$p\frac{3}{2},\ f\frac{5}{2}$	1	8	$p\frac{3}{2},\ f\frac{5}{2}$	3
9	$p\frac{3}{2},\ d\frac{3}{2}$	2	9	$f\frac{5}{2},\ p\frac{3}{2}$	1	9	$f\frac{5}{2},\ p\frac{3}{2}$	3
10	$d\frac{3}{2},\ p\frac{3}{2}$	2	10	$d\frac{3}{2},\ d\frac{3}{2}$	1	10	$p\frac{3}{2},\ f\frac{7}{2}$	3
11	$p\frac{3}{2},\ d\frac{5}{2}$	2	11	$d\frac{3}{2},\ d\frac{5}{2}$	1	11	$f\frac{7}{2},\ p\frac{3}{2}$	3
12	$d\frac{5}{2},\ p\frac{3}{2}$	2	12	$d\frac{5}{2},\ d\frac{3}{2}$	1	12	$d\frac{3}{2},\ d\frac{3}{2}$	3
13	$d\frac{3}{2},\ f\frac{5}{2}$	2	13	$d\frac{5}{2},\ d\frac{5}{2}$	1	13	$d\frac{3}{2},\ d\frac{5}{2}$	3
14	$f\frac{5}{2},\ d\frac{3}{2}$	2	14	$f\frac{5}{2},\ f\frac{5}{2}$	1	14	$d\frac{5}{2},\ d\frac{3}{2}$	3
15	$d\frac{3}{2},\ f\frac{7}{2}$	2	15	$f\frac{5}{2},\ f\frac{7}{2}$	1	15	$d\frac{5}{2},\ d\frac{5}{2}$	3
16	$f\frac{7}{2},\ d\frac{3}{2}$	2	16	$f\frac{7}{2},\ f\frac{5}{2}$	1	16	$f\frac{5}{2},\ f\frac{5}{2}$	3
17	$d\frac{5}{2},\ f\frac{5}{2}$	2	17	$f\frac{7}{2},\ f\frac{7}{2}$	1	17	$f\frac{5}{2},\ f\frac{7}{2}$	3
18	$f\frac{5}{2},\ d\frac{5}{2}$	2				18	$f\frac{7}{2},\ f\frac{5}{2}$	3
19	$d\frac{5}{2},\ f\frac{7}{2}$	2				19	$f\frac{7}{2},\ f\frac{7}{2}$	3
20	$f\frac{7}{2},\ d\frac{5}{2}$	2						

Table 4.8: TDCC $l_1 l_2 L$ coupled channels for the $1s^2\ ^1S$ term

channel	(l_1, l_2)	L	channel	(l_1, l_2)	L
1	s, s	0	1	s, p	1
2	p, p	0	2	p, s	1
3	d, d	0	3	p, d	1
4	f, f	0	4	d, p	1
5	g, g	0	5	d, f	1
6	h, h	0	6	f, d	1
			7	f, g	1
			8	g, f	1
			9	g, h	1
			10	h, g	1

Table 4.9: TDCC $l_1j_1l_2j_2J$ coupled channels for the $1s^2\ ^1S_0$ level

channel	(l_1j_1, l_2j_2)	J	channel	(l_1j_1, l_2j_2)	J
1	$s\frac{1}{2}$, $s\frac{1}{2}$	0	1	$s\frac{1}{2}$, $p\frac{1}{2}$	1
2	$p\frac{1}{2}$, $p\frac{1}{2}$	0	2	$p\frac{1}{2}$, $s\frac{1}{2}$	1
3	$p\frac{3}{2}$, $p\frac{3}{2}$	0	3	$s\frac{1}{2}$, $p\frac{3}{2}$	1
4	$d\frac{3}{2}$, $d\frac{3}{2}$	0	4	$p\frac{3}{2}$, $s\frac{1}{2}$	1
5	$d\frac{5}{2}$, $d\frac{5}{2}$	0	5	$p\frac{1}{2}$, $d\frac{3}{2}$	1
6	$f\frac{5}{2}$, $f\frac{5}{2}$	0	6	$d\frac{3}{2}$, $p\frac{1}{2}$	1
7	$f\frac{7}{2}$, $f\frac{7}{2}$	0	7	$p\frac{3}{2}$, $d\frac{3}{2}$	1
8	$g\frac{7}{2}$, $g\frac{7}{2}$	0	8	$d\frac{3}{2}$, $p\frac{3}{2}$	1
9	$g\frac{9}{2}$, $g\frac{9}{2}$	0	9	$p\frac{3}{2}$, $d\frac{5}{2}$	1
10	$h\frac{9}{2}$, $h\frac{9}{2}$	0	10	$d\frac{5}{2}$, $p\frac{3}{2}$	1
11	$h\frac{11}{2}$, $h\frac{11}{2}$	0	11	$d\frac{3}{2}$, f$\frac{5}{2}$	1
			12	$f\frac{5}{2}$, $d\frac{3}{2}$	1
			13	$d\frac{5}{2}$, $f\frac{5}{2}$	1
			14	$f\frac{5}{2}$, $d\frac{5}{2}$	1
			15	$d\frac{5}{2}$, $f\frac{7}{2}$	1
			16	$f\frac{7}{2}$, $d\frac{5}{2}$	1
			17	$f\frac{5}{2}$, $g\frac{7}{2}$	1
			18	$g\frac{7}{2}$, $f\frac{5}{2}$	1
			19	$f\frac{7}{2}$, $g\frac{7}{2}$	1
			20	$g\frac{7}{2}$, $f\frac{7}{2}$	1
			21	$f\frac{7}{2}$, $g\frac{9}{2}$	1
			22	$g\frac{9}{2}$, $f\frac{7}{2}$	1
			23	$g\frac{7}{2}$, $h\frac{9}{2}$	1
			24	$h\frac{9}{2}$, $g\frac{7}{2}$	1
			25	$g\frac{9}{2}$, $h\frac{9}{2}$	1
			26	$h\frac{9}{2}$, $g\frac{9}{2}$	1
			27	$g\frac{9}{2}$, $h\frac{11}{2}$	1
			28	$h\frac{11}{2}$, $g\frac{9}{2}$	1

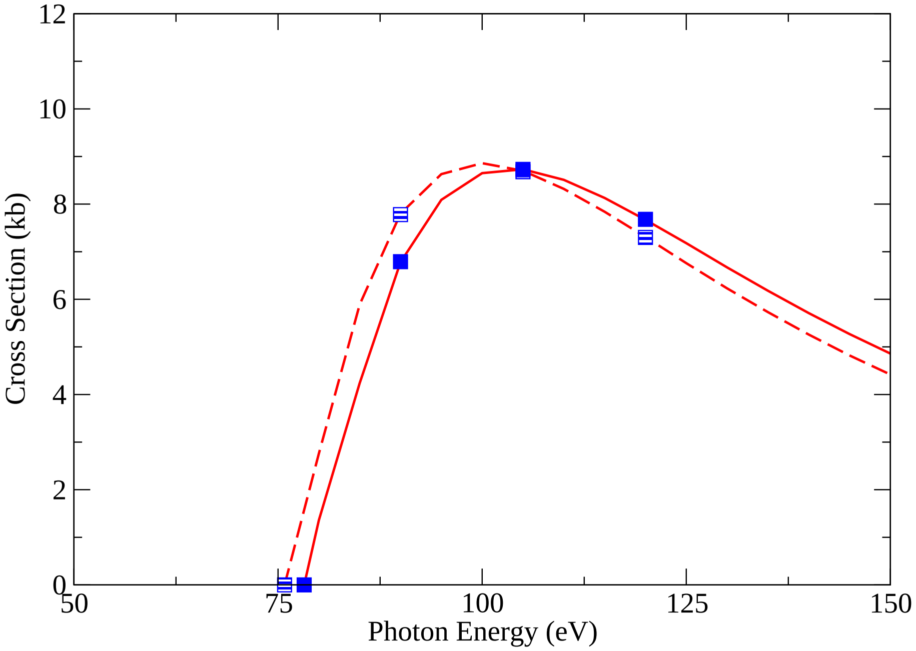

Figure 4.1: (color online) Double photoionization of the $1s^2$ ground configuration. Dashed line (red): TDCC(l_1l_2L) ($\Delta r_i = 0.20$) for the ^1S term, dashed squares (blue): TDCC($l_1j_1l_2j_2J$) ($\Delta r_i = 0.20$) for the $^1S_0$ level, solid line (red): TDCC(l_1l_2L) ($\Delta r_i = 0.10$) for the ^1S term, solid squares (blue): TDCC($l_1j_1l_2j_2J$) ($\Delta r_i = 0.10$) for the $^1S_0$ level (1.0 kb = 1.0×10^{-21} cm^2).

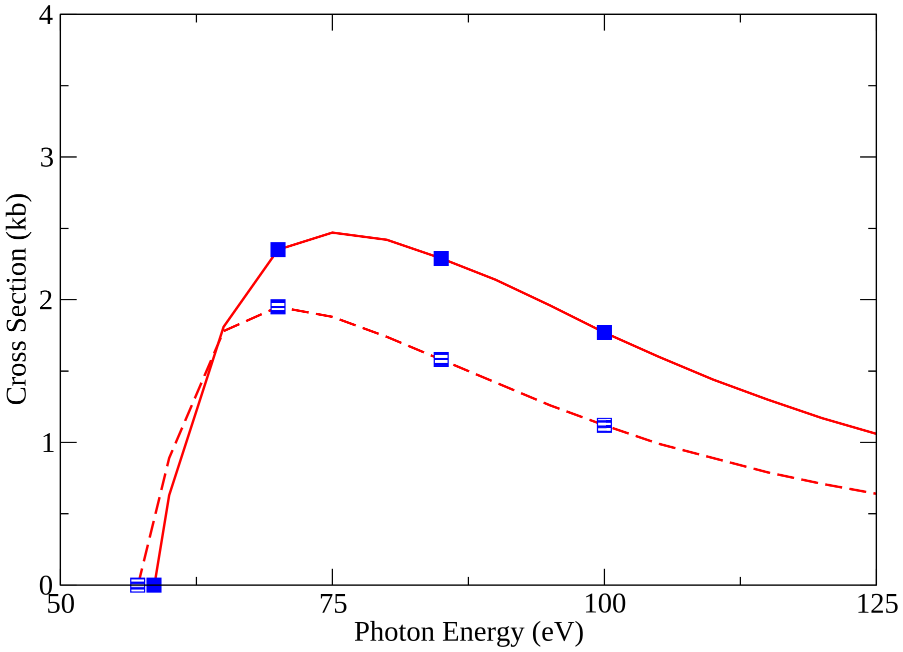

Figure 4.2: (color online) Double photoionization of the $1s2s$ excited configuration. Dashed line (red): TDCC(l_1l_2L) ($\Delta r_i = 0.20$) for the ^3S term, dashed squares (blue): TDCC($l_1j_1l_2j_2J$) ($\Delta r_i = 0.20$) for the $^3S_0$ level, solid line (red): TDCC(l_1l_2L) ($\Delta r_i = 0.10$) for the ^3S term, solid squares (blue): TDCC($l_1j_1l_2j_2J$) ($\Delta r_i = 0.10$) for the $^3S_0$ level (1.0 kb = 1.0×10^{-21} cm^2).

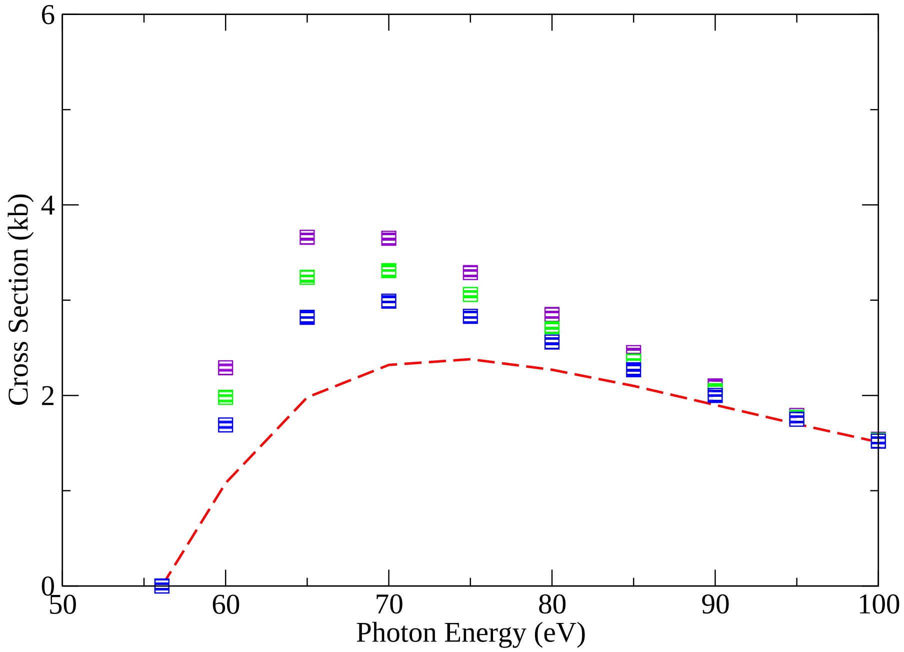

Figure 4.3: (color online) Double photoionization of the $1s2p$ excited configuration. Dashed line (red): TDCC(l_1l_2L) ($\Delta r_i = 0.20$) for the ^3P term, upper dashed squares (violet): TDCC($l_1j_1l_2j_2J$) ($\Delta r_i = 0.20$) for $^3P_0$ level, middle dashed squares (green): TDCC($l_1j_1l_2j_2J$) ($\Delta r_i = 0.20$) for $^3P_1$ level, lower dashed squares (blue): TDCC($l_1j_1l_2j_2J$) ($\Delta r_i = 0.20$) for $^3P_2$ level (1.0 kb = 1.0×10^{-21} cm^2).

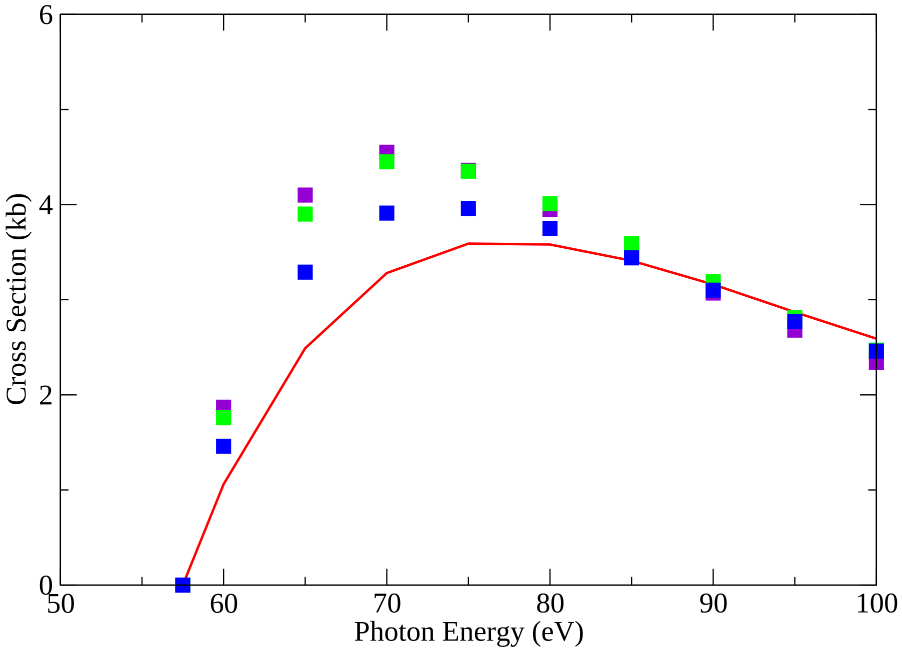

Figure 4.4: (color online) Double photoionization of the $1s2p$ excited configuration. Solid line (red): TDCC($l_1 l_2 L$) ($\Delta r_i = 0.10$) for the ^3P term, upper solid squares (violet): TDCC($l_1 j_1 l_2 j_2 J$) ($\Delta r_i = 0.10$) for $^3P_0$ level, middle solid squares (green): TDCC($l_1 j_1 l_2 j_2 J$) ($\Delta r_i = 0.10$) for $^3P_1$ level, lower solid squares (blue): TDCC($l_1 j_1 l_2 j_2 J$) ($\Delta r_i = 0.10$) for $^3P_2$ level (1.0 kb = 1.0×10^{-21} cm^2).

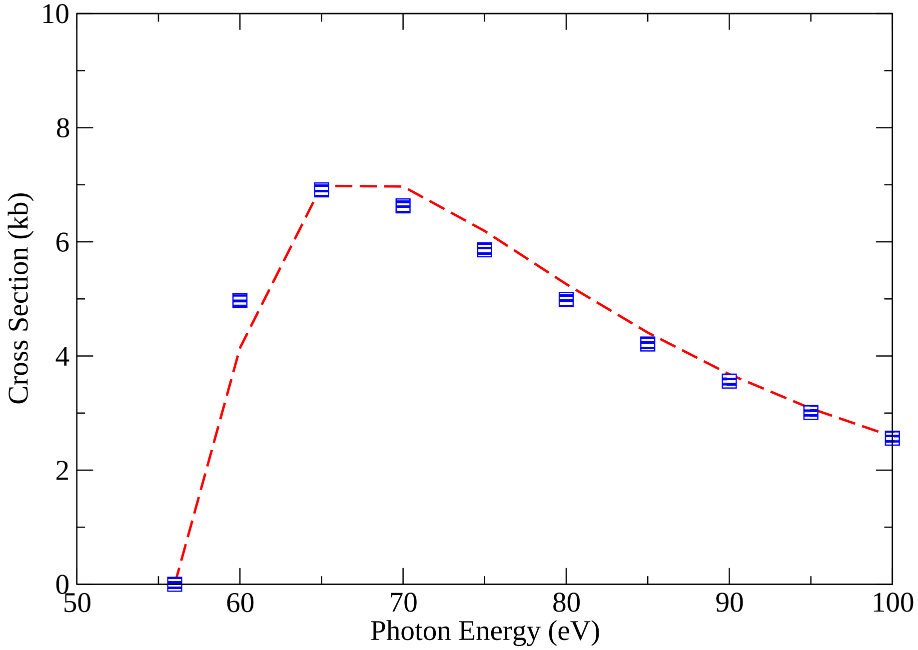

Figure 4.5: (color online) Average double photoionization of the $1s2p$ excited configuration. Dashed line (red): TDCC($l_1 l_2 L$) ($\Delta r_i = 0.20$) for $\frac{3}{4}\ {}^3P + \frac{1}{4}\ {}^1P$ terms, dashed squares (blue): TDCC($l_1 j_1 l_2 j_2 J$) ($\Delta r_i = 0.20$) for $\frac{1}{12}\ {}^3P_0 + \frac{3}{12}\ {}^3P_1 + \frac{5}{12}\ {}^3P_2 + \frac{3}{12}\ {}^1P_1$ levels (1.0 kb = 1.0×10^{-21} cm^2).

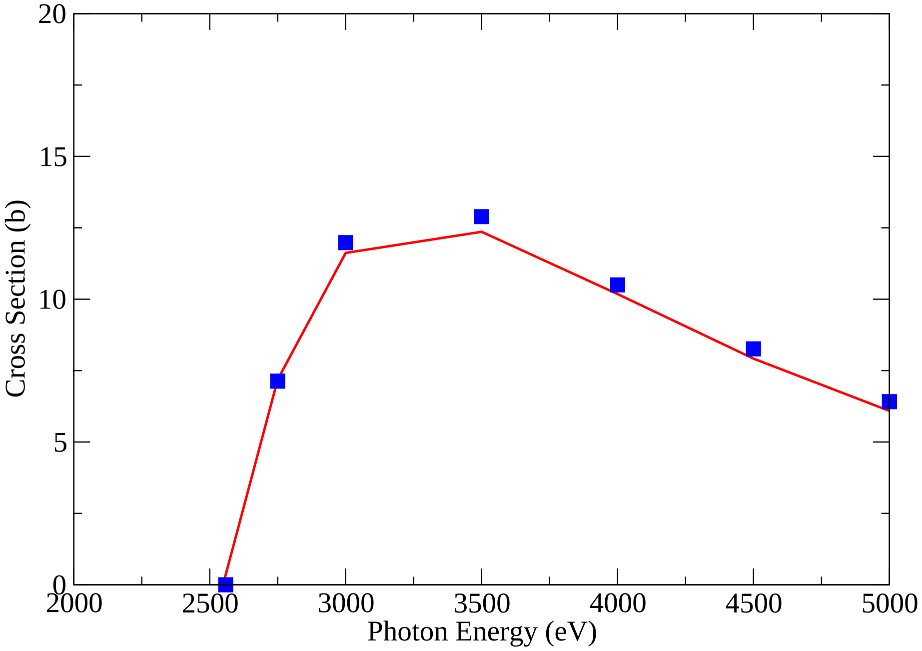

Figure 4.6: (color online) Double photoionization of the $1s^2$ ground configuration of Ne^{8+}. Solid line (red): non-relativistic TDCC for the ^1S term, squares (blue): semi-relativistic TDCC for the $^1S_0$ level (1.0 b $= 1.0 \times 10^{-24}$ cm^2).

Chapter 5

Single and Double Photoionization of Li_2

5.1 Background

Studies of the photoionization of diatomic molecules are important for the understanding of many astrophysical and laboratory science phenomena[26]. Single photoionization with excitation and double photoionization processes involve the quantal dynamics of two active electrons in the non-spherical Coulomb field of the residual molecular ion. Non-perturbative solutions to the Schrodinger equation have been applied to study the two-electron motion found in the photoionization of H_2. Total cross section calculations[61, 62] for the double photoionization of H_2 were found to be in good agreement with experiment[63, 64]. Subsequently energy and angle differential cross section calculations[65, 16] for the double photoionization of H_2 were found to be in good agreement with experiment[66]. Joint theoretical and experimental efforts have also examined the kinetic energy release effect[67] and new fragmentation patterns[68] in the double photoionization of H_2.

The Li_2 molecule is an ideal target in the exploration of two-electron motion in a non-spherical Coulomb field since it's dominant $1s\sigma^2 2p\sigma^2 2s\sigma^2$ ground configuration consists of two tightly bound closed inner subshells and one loosely bound closed outer subshell. We note that the double ionization potential of Li_2 is approximately a factor of 2.5 smaller that that of H_2. Previously only the single photoionization cross section for Li_2 has been calculated, using perturbation theory for the the scattering matrix element and both the distorted-wave approximation[69] and the random phase approximation[70] for the ejected electron continuum.

5.2 Theory

5.2.1 3D Time-Dependent Close-Coupling Method

In previous work the time-dependent close-coupling method was developed for the photoionization of H_2^+[71]. We present a brief review of the extension to any one active electron diatomic molecule.

For photoionization of an N electron diatomic molecule with one active electron, the total electronic wavefunction may be expanded in rotational functions:

$$\Psi(\vec{r},t) = \sum_m \frac{P_m(r,\theta,t)}{r\sqrt{\sin\theta}} \frac{e^{im\phi}}{\sqrt{2\pi}} \ . \tag{5.1}$$

Upon substitution into the time-dependent Schrodinger equation, we obtain the time-dependent close-coupling equations given by:

$$\begin{aligned} i\frac{\partial P_m(r,\theta,t)}{\partial t} &= T_m(r,\theta)P_m(r,\theta,t) \\ &\quad + \sum_{m'} W_{m,m'}(r,\theta,t)P_{m'}(r,\theta,t) \ . \end{aligned} \tag{5.2}$$

The kinetic, nuclear, and molecular core operator is given by:

$$\begin{aligned} T_m(r,\theta) &= K(r) + \bar{K}(r,\theta) + \frac{m^2}{2r^2(\sin\theta)^2} \\ &\quad - \sum_{\pm} \frac{Z_t}{\sqrt{r^2 + \frac{1}{4}R_t^2 \pm rR_t\cos\theta}} + V_{core}^{N-1}(r,\theta) \ , \end{aligned} \tag{5.3}$$

where the internuclear axis is located along the z axis, $K(r)$ and $\bar{K}(r,\theta)$ are kinetic energy operators, Z_t is the target nuclear charge, R_t is the target internuclear distance, and $V_{core}^{N-1}(r,\theta)$ is a Hartree with local exchange potential for the remaining (N-1) electrons, thus for H_2^+ we have $V_{core}^{N-1}(r,\theta) = 0$. The radiation field operator for linear polarization, where the field is perpendicular to the internuclear axis, is given by:

$$\begin{aligned} W_{m,m'}(r,\theta,t) &= E(t)\cos\omega t \\ &\quad \times r\cos\theta < m|m' > , \end{aligned} \tag{5.4}$$

while the radiation field operator for circular polarization, where the field is parallel to the internuclear axis, is given by:

$$\begin{aligned} W_{m,m'}(r,\theta,t) &= \sqrt{\frac{1}{2}}E(t)\cos\omega t \\ &\quad \times r\sin\theta < m|e^{i\phi}|m' > , \end{aligned} \tag{5.5}$$

where $E(t)$ is the electric field amplitude, ω is the radiation field amplitude, and the length gauge is chosen.

A complete set of bound, $P_{nl|m|}(r,\theta)$, and continuum, $P_{kl|m|}(r,\theta)$, radial and angular orbitals are determined by the diagonalization of the Hamiltonian of Eq.(5.3). The initial condition for the solution of Eq.(5.2) is given by:

$$P_m(r,\theta,t=0) = P_{n_0l_0|m_0|}(r,\theta)\delta_{m,m_0} \ . \tag{5.6}$$

The total cross section for single photoionization leaving the molecular ion in the initial state is given by:

$$\sigma_{single}(n_0l_0m_0) = \frac{\omega}{I}\frac{\mathcal{P}_{single}(n_0l_0m_0)}{\mathcal{T}} \ , \tag{5.7}$$

where I is the radiation field intensity and $\mathcal{T}$ is the integral of the electromagnetic field pulse shape with respect to propagation time. The single photoionization probability is given by:

$$\begin{aligned} \mathcal{P}_{single}(n_0l_0m_0) &= \int_0^\infty dr \int_0^\pi d\theta |P_m(r,\theta,t)P_m(r,\theta,t)|^2 \\ &\quad -\sum_{n,l} |\int_0^\infty dr \int_0^\pi d\theta P_m(r,\theta,t)P_{nl|m|}(r,\theta)|^2 \ , \end{aligned} \tag{5.8}$$

where $m = m_0$ for linear polarization and $m = m_0 \pm 1$ for circular polarization. We note that the ionization probabilities and cross sections may only be calculated after the wavefunction, $P_m(r, \theta, t)$, has evolved to sufficiently long times.

5.2.2 6D Time-Dependent Close-Coupling Method

In previous work the time-dependent close-coupling method was developed for the photoionization of H_2[61]. We present a brief review of the extension to any two active electron diatomic molecule.

For photoionization of an N electron diatomic molecule with two active electrons, the total electronic wavefunction may be expanded in products of rotational functions for each $M = m_1 + m_2$ symmetry:

$$\Psi(\vec{r}_1, \vec{r}_2, t) = \sum_{m_1, m_2} \frac{P^M_{m_1 m_2}(r_1, \theta_1, r_2, \theta_2, t)}{r_1 r_2 \sqrt{\sin\theta_1}\sqrt{\sin\theta_2}} \Phi_{m_1}(\phi_1)\Phi_{m_2}(\phi_2) \ . \tag{5.9}$$

Upon substitution into the time-dependent Schrodinger equation in the weak field perturbative limit, we obtain the time-dependent close-coupling equations given by:

$$\begin{aligned} i\frac{\partial P^M_{m_1 m_2}(r_1, \theta_1, r_2, \theta_2, t)}{\partial t} \quad = \quad & \sum_{i=1,2} (T_{m_i}(r_i, \theta_i)) P^M_{m_1 m_2}(r_1, \theta_1, r_2, \theta_2, t) \\ & + \sum_{m_1', m_2'} V^M_{m_1 m_2, m_1' m_2'}(r_1, \theta_1, r_2, \theta_2) \\ & \times P^M_{m_1' m_2'}(r_1, \theta_1, r_2, \theta_2, t) \\ & + \sum_{m_1'', m_2''} W^{M M_0}_{m_1 m_2, m_1'' m_2''}(r_1, \theta_1, r_2, \theta_2, t) \\ & \times P^{M_0}_{m_1'' m_2''}(r_1, \theta_1, r_2, \theta_2) e^{-iE_0 t} \ . \end{aligned} \tag{5.10}$$

The kinetic, nuclear, and molecular core operator is given by:

$$\begin{aligned} T_m(r,\theta) &= K(r) + \bar{K}(r,\theta) + \frac{m^2}{2r^2(\sin\theta)^2} \\ &\quad - \sum_{\pm} \frac{Z_t}{\sqrt{r^2 + \frac{1}{4}R_t^2 \pm rR_t\cos\theta}} + V_{core}^{N-2}(r,\theta)\ , \end{aligned} \tag{5.11}$$

where $V_{core}^{N-2}(r,\theta)$ is a Hartree with local exchange potential for the remaining (N-2) electrons, thus for H_2 we have $V_{core}^{N-2}(r,\theta) = 0$. The Coulomb repulsion operator is given by:

$$\begin{aligned} V^M_{m_1m_2,m_1'm_2'}(r_1,\theta_1,r_2,\theta_2) &= \sum_\lambda \frac{r_<^\lambda}{r_>^{\lambda+1}} \sum_q \frac{(\lambda-|q|)!}{(\lambda+|q|)!} P_\lambda^{|q|}(\cos\theta_1) P_\lambda^{|q|}(\cos\theta_2) \\ &\quad \times < m_1m_2|e^{iq(\phi_2-\phi_1)}|m_1'm_2' > , \end{aligned} \tag{5.12}$$

where $P_\lambda^{|q|}(\cos\theta)$ is an associated Legendre function. The radiation field operator for linear polarization is given by:

$$\begin{aligned} W^{MM_0}_{m_1m_2,m_1''m_2''}(r_1,\theta_1,r_2,\theta_2) &= E(t)\cos\omega t \\ &\quad \times(r_1\cos\theta_1 < m_1m_2|m_1''m_2'' > \\ &\quad + r_2\cos\theta_2 < m_1m_2|m_1''m_2'' >)\ , \end{aligned} \tag{5.13}$$

while the radiation field operator for circular polarization is given by:

$$\begin{aligned} W^{MM_0}_{m_1m_2,m_1''m_2''}(r_1,\theta_1,r_2,\theta_2) &= \sqrt{\frac{1}{2}} E(t)\cos\omega t \\ &\quad \times(r_1\sin\theta_1 < m_1m_2|e^{i\phi_1}|m_1''m_2'' > \\ &\quad + r_2\sin\theta_2 < m_1m_2|e^{i\phi_2}|m_1''m_2'' >)\ . \end{aligned} \tag{5.14}$$

A complete set of bound, $P_{nl|m|}(r,\theta)$, and continuum, $P_{kl|m|}(r,\theta)$, radial and angular orbitals are determined by the diagonalization of the Hamiltonian of Eq.(5.11). The function $P^{M_0}_{m_1m_2}(r_1,\theta_1,r_2,\theta_2)$ and energy E_0 in Eq.(5.10) are obtained by relaxation of Eq.(5.10) in imaginary time without the radiation field operator. The initial condition for the solution of Eq.(5.10) is given by:

$$P^M_{m_1m_2}(r_1,\theta_1,r_2,\theta_2,t=0)=0 \tag{5.15}$$

The total cross section for single photoionization leaving the molecular ion in a specific bound state is given by:

$$\sigma_{single}(nlm)=\frac{\omega}{I}\frac{\partial\mathcal{P}_{single}(nlm)}{\partial t}\ . \tag{5.16}$$

The total cross section for single photoionization is given by:

$$\sigma_{single}=\sum_{nlm}\sigma_{single}(nlm)\ . \tag{5.17}$$

The single ionization probability is given by:

$$\begin{aligned}\mathcal{P}_{single}(nlm) \ = \ & \sum_{m'}\int d1\left|\int d2P^M_{m'm}(1,2,t)P_{nl|m|}(2)\right|^2 \\ & -\sum_{n',l',m'}\left|\int d1\int d2P^M_{m'm}(1,2,t)P_{n'l'|m'|}(1)P_{nl|m|}(2)\right|^2 \\ & +\sum_{m'}\int d2\left|\int d1P^M_{m'm}(1,2,t)P_{nl|m|}(1)\right|^2 \\ & -\sum_{n',l',m'}\left|\int d1\int d2P^M_{m'm}(1,2,t)P_{nl|m|}(1)P_{n'l'|m'|}(2)\right|^2\ .\end{aligned} \tag{5.18}$$

The total cross section for double photoionization is given by:

$$\sigma_{double}=\frac{\omega}{I}\frac{\partial\mathcal{P}_{double}}{\partial t}\ . \tag{5.19}$$

The double ionization probability is given by:

$$\begin{aligned}
\mathcal{P}_{double} &= \sum_{m',m} \int d1 \int d2 \left| P^{M}_{m'm}(1,2,t) \right|^2 \\
&\quad - \sum_{nlm} \mathcal{P}_{single}(nlm) \\
&\quad - \sum_{n,l,m} \sum_{n',l',m'} \left| \int d1 \int d2 P^{M}_{mm'}(1,2,t) P_{nl|m|}(1) P_{n'l'|m'|}(2) \right|^2 \ . \qquad (5.20)
\end{aligned}$$

In both Eqs.(5.18) and (5.20):

$$P^{M}_{m'm}(1,2,t) \ = \ P^{M}_{m'm}(r_1,\theta_1,r_2,\theta_2,t)$$

and

$$\int dN \ = \ \int_0^{\infty} dr_N \int_0^{\pi} d\theta_N \ ,$$

where $M = M_0$ for linear polarization and $M = M_0 \pm 1$ for circular polarization. We note that the ionization probabilities and cross sections may only be calculated after the wavefunction, $P^{M}_{m'm}(1,2,t)$, has evolved to sufficiently long times.

5.3 Calculations and Results

5.3.1 3D Time-Dependent Close-Coupling Method

The 3D time-dependent close-coupling (TDCC-3D) method is used to calculate single photoionization cross sections for Li_2 at incident energies above the single ionization energy threshold.

A single configuration self-consistent field method based on a linear combination of Slater-type orbitals[72] is first used to calculate the $1s\sigma^2 2p\sigma^2 2s\sigma$ ground configuration of Li_2^+ at the equilibrium internuclear distance of $R_t = 5.0$ for Li_2. The molecular bound orbitals are then transformed[73] onto various two-dimensional numerical lattices with a uniform radial mesh spacing Δr and a uniform angular mesh spacing $\Delta\theta$. For $V^1_{core}(r,\theta)$ in Eq.(5.3), we choose the Hartree with local exchange potential given by:

$$\begin{aligned} V_{HX}(r,\theta) &= \sum_{k=0} \int_0^\infty dr' \int_0^\pi d\theta' \frac{r_<^k}{r_>^{k+1}} P_0^k(\cos\theta) P_0^k(\cos\theta') \\ &\times \left[2P^2_{1s\sigma}(r',\theta') + 2P^2_{2p\sigma}(r',\theta') + P^2_{2s\sigma}(r',\theta')\right] \\ &- \frac{\alpha}{2}\left[\frac{24\rho(r,\theta)}{\pi}\right]^{\frac{1}{3}} , \end{aligned} \tag{5.21}$$

where

$$\rho(r,\theta) = \frac{2P^2_{1s\sigma}(r,\theta) + 2P^2_{2p\sigma}(r,\theta) + P^2_{2s\sigma}(r,\theta)}{2\pi r^2 \sin\theta} . \tag{5.22}$$

Diagonalization of the Hamiltonian of Eq.(5.3) was used to obtain all of the Li_2 bound states for $m = 0, 1$ on various two-dimensional lattices. The parameter α of Eq.(5.21) was adjusted for each lattice, as given in Table 5.1, so that the ionization potential of Li_2 was in agreement with the NIST[74] value of 5.1 eV.

Time-dependent close-coupling calculations were then carried out for Li_2 using various two-dimensional lattices. An implicit method[71] was used to solve the close-coupled equations for propagation in real time. Propagation of Eq.(5.2) was made for ten radiation field periods, for photon energies ranging from $\omega = 6.0$ eV to $\omega = 40.0$ eV, and for a radiation field intensity of $I = 10^{12}$ W/cm^2. Changing the intensity to $I = 10^{13}$ W/cm^2 yielded very little change in the final photoionization cross sections. The TDCC-3D equations given by Eq.(5.3) for the ionization of the $2s\sigma$ orbital reduces to one $m = 0$ coupled channel for linear polarization and two $m = 0, 1$ coupled channels for circular polarization.

To prevent collapse of the outer subshell wavefunctions, $P_m(r, \theta, t)$, into closed subshells during propagation of the close-coupled equations, we use a standard core orthogonalization method. Thus the $P_0(r, \theta, t)$ coupled channel is orthogonalized at each time step according to:

$$\begin{aligned} P_0(r,\theta,t) &= P_0(r,\theta,t) \\ &\quad -P_{1s\sigma}(r,\theta)\int_0^\infty dr' \int_0^\pi d\theta' P_{1s\sigma}(r',\theta')P_0(r',\theta',t) \\ &\quad -P_{2p\sigma}(r,\theta)\int_0^\infty dr' \int_0^\pi d\theta' P_{2p\sigma}(r',\theta')P_0(r',\theta',t) \ . \end{aligned} \tag{5.23}$$

Single ionization probabilities, $\mathcal{P}_{single}(n_0 l_0 m_0)$, from Eq.(5.8) are obtained at the end of the ten radiation field periods.

Single photoionization cross sections calculated using the TDCC-3D method are presented in Table 5.2. To compare with previous distorted-wave[69] and random-phase approximation [70] calculations, we calculate a "total" photoionization cross section found by adding the linear polarization cross section and twice the circular polarization cross section together, where the factor of two comes from the assumption that right circular polarization results ($m = 0 \rightarrow m = 1$) are equal to left circular polarization results ($m = 0 \rightarrow m = -1$). We note that comparisons with experiment generally use an "average" photoionization cross section found by dividing the "total" cross section by three. As found in Table 5.2 the previous distorted-wave[69] and random-phase approximation[70] peak cross sections are in reasonable agreement with TDCC-3D cross sections using a 2D lattice with either ($\Delta r = 0.10, \Delta\theta = \frac{\pi}{32}$) and ($\Delta r = 0.05, \Delta\theta = \frac{\pi}{32}$), but not with ($\Delta r = 0.20, \Delta\theta = \frac{\pi}{32}$). For photon energies near threshold a radial box size of $R = 96.0$ was needed to obtain a cross section that varies smoothly with photon energy, while at higher photon energies ($\omega \geq 20.0$ eV) a radial box size of $R = 48.0$ is sufficient. We also tried a 2D lattice with ($\Delta r = 0.10, \Delta\theta = \frac{\pi}{64}$) and found only a small change in the cross sections at the peak and no change in the cross sections at the higher photon energies when compared to the results from the 2D lattice with ($\Delta r = 0.10, \Delta\theta = \frac{\pi}{32}$).

Single photoionization cross sections calculated using the TDCC-3D method using a 2D lattice with ($\Delta r = 0.10, \Delta\theta = \frac{\pi}{32}$) are presented in Figure 5.1. Both the linear and circular polarization cross sections peak around 13 eV with the linear results about 3.8 times higher than the circular results. We note that at the higher photon energies ($\omega \geq 30$ eV) that the linear and circular cross sections have similar values.

5.3.2 6D Time-Dependent Close-Coupling Method

The 6D time-dependent close-coupling (TDCC-6D) method is used to calculate single and double photoionization cross sections for Li_2 at incident energies above the double ionization energy threshold. Based on our preceeding TDCC-3D calculations using different 2D lattices, we elected to carry out TDCC-6D calculations using a 4D lattice with ($\Delta r_1 = \Delta r_2 = 0.10, \Delta\theta_1 = \Delta\theta_2 = \frac{\pi}{32}$) and an overall box size of $R_1 = R_2 = 48.0$. It is computationally much less expensive to make lattice choices using the TDCC-3D method than the TDCC-6D method.

A single configuration self-consistent field method based on a linear combination of Slater-type orbitals[72] is first used to calculate the $1s\sigma^2 2p\sigma^2$ ground configuration of Li_2^{++} at the equilibrium internuclear distance of $R_t = 5.0$ for Li_2. The molecular bound orbitals are then transformed[73] onto a two-dimensional numerical lattice with a uniform radial mesh spacing of $\Delta r = 0.10$ and a uniform angular mesh spacing of $\Delta\theta = \frac{\pi}{32}$. For $V^2_{core}(r, \theta)$

in Eq.(5.11), we choose the Hartree with local exchange potential given by:

$$\begin{aligned} V_{HX}(r,\theta) &= \sum_{k=0} \int_0^\infty dr' \int_0^\pi d\theta' \frac{r_<^k}{r_>^{k+1}} P_0^k(\cos\theta) P_0^k(\cos\theta') \\ &\quad \times \left[2P_{1s\sigma}^2(r',\theta') + 2P_{2p\sigma}^2(r',\theta')\right] \\ &\quad -\frac{\alpha}{2}\left[\frac{24\rho(r,\theta)}{\pi}\right]^{\frac{1}{3}} , \end{aligned} \qquad (5.24)$$

where

$$\rho(r,\theta) = \frac{2P_{1s\sigma}^2(r,\theta) + 2P_{2p\sigma}^2(r,\theta)}{2\pi r^2 \sin\theta} . \qquad (5.25)$$

We then made calculations using GAUSSIAN 2009 [75] and various basis set extrapolation methods[76] to find the ionization potential for Li_2^+ at the equilibrium internuclear distance of $R_t = 5.0$ for Li_2. For Li_2^+ we obtained an ionization potential of 12.0 eV. Diagonalization of the Hamiltonian of Eq.(5.11) was used to obtain all of the Li_2^+ bound states for $m = 0, 1, 2$ on a 2D lattice with $(\Delta r = 0.10, \Delta\theta = \frac{\pi}{32})$. The choice for the parameter α in Eq.(5.24) of 1.21 was found to given an ionization potential of Li_2^+ in agreement with the GAUSSIAN 2009 [75] value of 12.0 eV.

Time-dependent close-coupling calculations were then carried out for Li_2 using a 4D lattice with $(\Delta r_1 = \Delta r_2 = 0.10, \Delta\theta_1 = \Delta\theta_2 = \frac{\pi}{32})$. An implicit method[61] was used to solve the close-coupled equations for both relaxation in imaginary time and propagation in real time. Using a uniform mesh spacing of $\Delta\tau = 0.01$, relaxation of Eq.(5.10) for 2000 time steps yielded two electron outer subshell wavefunctions:

$$P_{m_1 m_2}^{M_0}(r_1,\theta_1,r_2,\theta_2) = P_{m_1 m_2}^{M_0}(r_1,\theta_1,r_2,\theta_2,\tau \to \infty) , \qquad (5.26)$$

where $M_0 = 0$ and (m_1, m_2) covers 5 coupled channels:

$$(0,0), (1,-1), (-1,1), (2,-2), (-2,2) . \qquad (5.27)$$

The two electron outer subshell energy was found to be $E_0 = -17.1$ eV.

To prevent collapse of the outer subshell wavefunctions, $P^M_{m_1m_2}(1,2,\tau)$, into closed inner subshells during relaxation of the close-coupled equations, we use a standard core orthogonalization method. Thus the $P^0_{00}(1,2,\tau)$ coupled channel is orthogonalized at each time step according to :

$$\begin{aligned}
P^0_{00}(1,2,\tau) \;=\; & P^0_{00}(1,2,\tau) \\
& -P_{1s\sigma}(1)\int d1' P_{1s\sigma}(1')P^0_{00}(1',2,\tau) \\
& -P_{2p\sigma}(1)\int d1' P_{2p\sigma}(1')P^0_{00}(1',2,\tau) \\
& -P_{1s\sigma}(2)\int d2' P_{1s\sigma}(2')P^0_{00}(1,2',\tau) \\
& -P_{2p\sigma}(2)\int d2' P_{2p\sigma}(2')P^0_{00}(1,2',\tau) \\
& +P_{1s\sigma}(1)P_{1s\sigma}(2)\int d1' \int d2' P_{1s\sigma}(1')P_{1s\sigma}(2')P^0_{00}(1,2,\tau) \\
& +P_{1s\sigma}(1)P_{2p\sigma}(2)\int d1' \int d2' P_{1s\sigma}(1')P_{2p\sigma}(2')P^0_{00}(1,2,\tau) \\
& +P_{2p\sigma}(1)P_{1s\sigma}(2)\int d1' \int d2' P_{2p\sigma}(1')P_{1s\sigma}(2')P^0_{00}(1,2,\tau) \\
& +P_{2p\sigma}(1)P_{2p\sigma}(2)\int d1' \int d2' P_{2p\sigma}(1')P_{2p\sigma}(2')P^0_{00}(1,2,\tau)\ . \qquad (5.28)
\end{aligned}$$

The wavefunctions for the other 4 coupled channels do not need to be orthogonalized.

Using a uniform mesh spacing of $\Delta t = 0.005$, propagation of Eq.(5.10) was made for ten radiation field periods, for photon energies ranging from $\omega = 20.0$ eV to 40.0 eV, and for a radiation field intensity of $I = 10^{15}$ W/cm^2. Changing the intensity to $I = 10^{14}$ W/cm^2 yielded very little change in the final photoionization cross sections. For linear polarization $M = 0$ and (m_1, m_2) covers the 5 coupled channels of Eq.(5.27), while for circular polarization $M = 1$ and (m_1, m_2) covers 6 coupled channels:

$$(0,1), (1,0), (-1,2), (2,-1), (-2,3), (3,-2)\ . \qquad (5.29)$$

Including the additional coupled channels $(3, -3)$ and $(-3, 3)$ for linear polarization, or $(-3, 4)$ and $(4, -3)$ for circular polarization, made very little change in the cross sections.

To prevent collapse of the outer subshell wavefunctions, $P^M_{m_1 m_2}(1, 2, t)$, into closed subshells during propagation of the close-coupled equations, we use the core orthogonalization method presented above for relaxation of the close-coupled equations. For linear polarization Eq.(5.28) is used with $\tau \rightarrow t$. For circular polarization, the $P^1_{01}(1, 2, t)$ coupled channel is orthogonalized at each time step according to:

$$\begin{aligned} P^1_{01}(1,2,t) &= P^1_{01}(1,2,t) \\ &\quad -P_{1s\sigma}(1) \int d1' P_{1s\sigma}(1') P^1_{01}(1',2,t) \\ &\quad -P_{2p\sigma}(1) \int d1' P_{2p\sigma}(1') P^1_{01}(1',2,t) \ , \end{aligned} \tag{5.30}$$

and the $P^1_{10}(1, 2, t)$ coupled channel is orthogonalized at each time step according to:

$$\begin{aligned} P^1_{10}(1,2,t) &= P^1_{10}(1,2,t) \\ &\quad -P_{1s\sigma}(2) \int d2' P_{1s\sigma}(2') P^1_{10}(1,2',t) \\ &\quad -P_{2p\sigma}(2) \int d2' P_{2p\sigma}(2') P^1_{10}(1,2',t) \ . \end{aligned} \tag{5.31}$$

The wavefunctions for the other 4 coupled channels do not need to be orthogonalized. Single ionization probabilities, $\mathcal{P}_{single}(nlm)$, and double ionization probabilities, $\mathcal{P}_{double}$, from Eqs.(5.18) and (5.20) are obtained at the end of the ten radiation field periods.

Single and double photoionization cross sections calculated using the TDCC-6D method on a 4D lattice with ($\Delta r_1 = \Delta r_2 = 0.10, \Delta\theta_1 = \Delta\theta_2 = \frac{\pi}{32}$) are presented in Table 5.3. For linear polarization at 20.0 eV, the results for total single ionization are approximately 55% above the results for single ionization leaving Li_2^+ in the $2s\sigma$ bound state. For circular polarization at 20.0 eV, the results for total single ionization are approximately 67% above the results for single ionization leaving Li_2^+ in the $2s\sigma$ bound state. We note that the ratio of double ionization to total single ionization is 0.023 for linear polarization and 0.018 for circular polarization at a photon energy of 25.0 eV.

Single photoionization cross sections leaving Li_2^+ in the $2s\sigma$ bound state calculated using the TDCC-6D method on a 4D lattice with $(\Delta r_1 = \Delta r_2 = 0.10, \Delta\theta_1 = \Delta\theta_2 = \frac{\pi}{32})$ are presented in Figure 5.1. For photon energies greater than 20.0 eV, the TDCC-3D results are somewhat higher than the TDCC-6D results for linear polarization, while the TDCC-3D and TDCC-6D results are in close agreement for circular polarization. The TDCC-6D results should be more accurate than the TDCC-3D results due to the use of the correlated two-electron outer subshell wavefunction found in Eq.(5.26).

Double photoionization cross sections calculated using the TDCC-6D method on a 4D lattice with $(\Delta r_1 = \Delta r_2 = 0.10, \Delta\theta_1 = \Delta\theta_2 = \frac{\pi}{32})$ are presented in Figure 5.2. The TDCC-6D results for linear polarization are found to be larger than for circular polarization for all incident photon energies. The peak cross sections for Li_2 at around a photon energy of 25.0 eV are found to be 0.0160 Mb for linear polarization and 0.0100 Mb for circular polarization. On the other hand we note that for H_2, TDCC-6D calculations[61] found the peak double ionization cross sections at around a photon energy of 70.0 eV to be 0.0003 Mb for linear polarization and 0.0033 Mb for circular polarization.

5.4 Summary

Time-dependent close-coupling methods have been used to calculate single and double photoionization cross sections for Li_2. With four tightly bound inner subshell electrons and two loosely bound outer subshell electrons, diatomic Lithium is an ideal target for the study of two-electron continuum correlation effects in a non-spherical Coulomb field. The TDCC-3D method is used to calculate single photoionization cross sections and to find the optimal lattice spacings for use by the TDCC-6D method. The TDCC-6D calculations for single and double photoionization of Li_2 were made for photon energies above the double ionization threshold of 17.1 eV. In contrast to previous TDCC-6D calculations for H_2[61], the linear polarization cross sections are larger than the circular polarization cross sections and overall found to be approximately five times larger. We hope that our theoretical work will stimulate future experimental studies of the double photoionization of Li_2.

Table 5.1: Local Exchange Parameter for the Li_2^+ Core Potential

Δr	$\Delta\theta$	α
0.20	$\frac{\pi}{32}$	1.10
0.10	$\frac{\pi}{32}$	0.86
0.05	$\frac{\pi}{32}$	0.72

Table 5.2: Single Photoionization Peak Cross Sections (1.0 Mb = 1.0×10^{-18} cm^2)

Method	Photon Energy (eV)	Cross Section (Mb)
DW[69]	11 eV	2.3 Mb
RPA[70]	11 eV	2.6 Mb
TDCC-3D (0.20,$\frac{\pi}{32}$)	16 eV	1.8 Mb
TDCC-3D (0.10,$\frac{\pi}{32}$)	13 eV	2.6 Mb
TDCC-3D (0.05,$\frac{\pi}{32}$)	13 eV	2.7 Mb

Table 5.3: Photoionization Cross Sections (1.0 Mb = 1.0×10^{-18} cm^2)

E(eV)	$\sigma_{single}(2s\sigma)$ linear	σ_{single} linear	σ_{double} linear	$\sigma_{single}(2s\sigma)$ circular	σ_{single} circular	σ_{double} circular
20.0	0.82	1.27	0.0147	0.39	0.65	0.0064
22.5	0.61	0.90	0.0168	0.38	0.60	0.0087
25.0	0.49	0.71	0.0160	0.35	0.55	0.0100
27.5	0.41	0.58	0.0140	0.34	0.51	0.0099
30.0	0.34	0.48	0.0123	0.32	0.47	0.0094
35.0	0.24	0.35	0.0101	0.27	0.39	0.0078
40.0	0.19	0.28	0.0088	0.22	0.31	0.0063

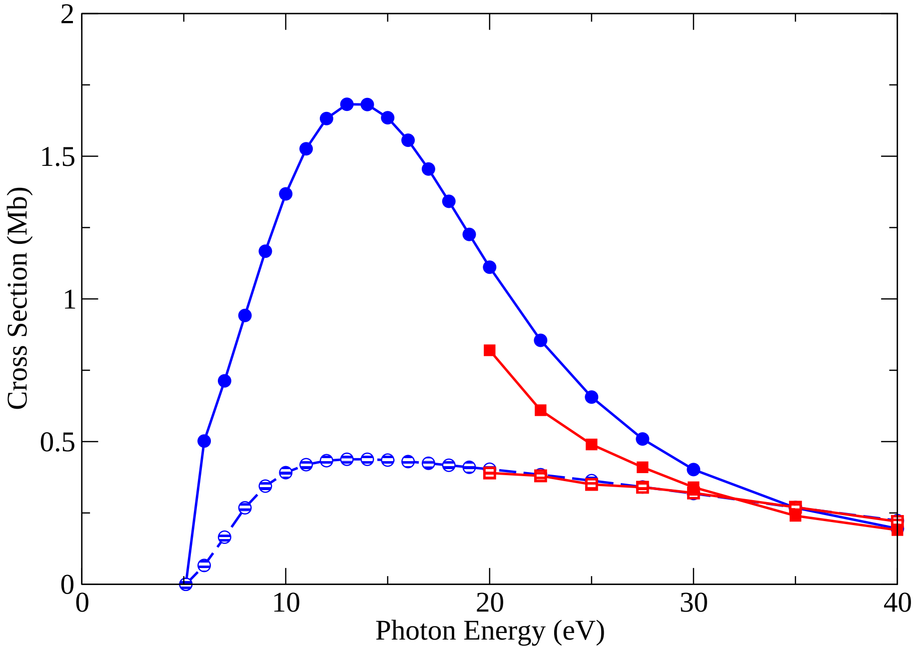

Figure 5.1: (color online) Single photoionization of Li_2. Solid line with circles (blue): linear TDCC-3D, dashed line with circles (blue): circular TDCC-3D, solid line with squares (red): linear TDCC-6D, dashed line with squares (red): circular TDCC-6D (1.0 Mb $= 1.0 \times 10^{-18}$ cm^2).

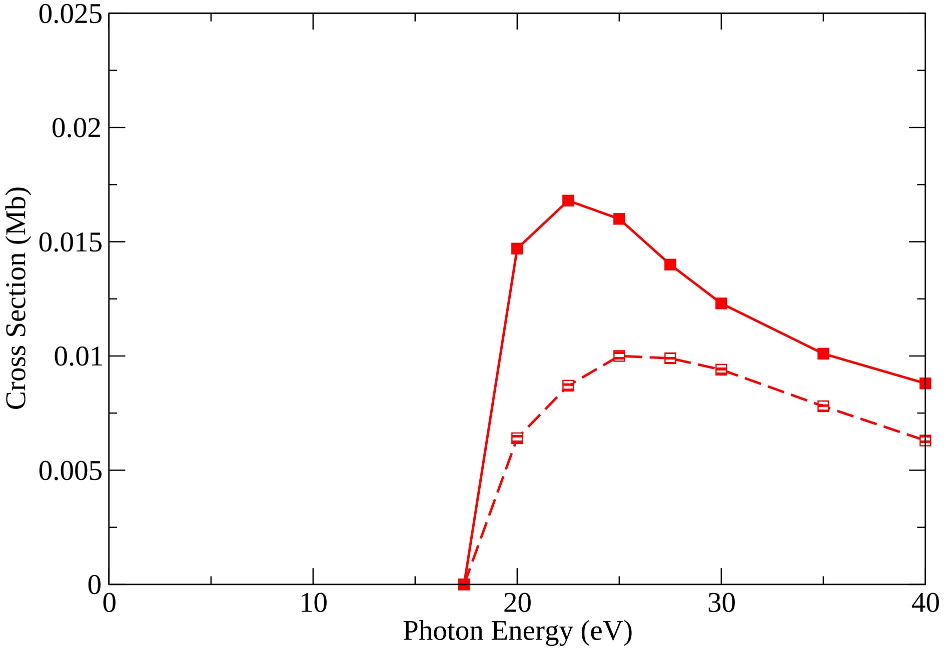

Figure 5.2: (color online) Double photoionization of Li_2. Solid line with squares (red): linear TDCC-6D, dashed line with squares (red): circular TDCC-6D (1.0 Mb = 1.0 × 10^{-18} cm^2).

Chapter 6

Non-Equilibrium Modeling of the Fe XVII 3C/3D ratio for an Intense X-ray Free Electron Laser

6.1 Background

Spectral emission from Fe XVII can be used as a valuable plasma diagnostic for both laboratory and astrophysical plasmas [17, 18]. The ratio of the 3C line intensity (transition $2p^5$ 3d ($^1P_1$) → $2p^6$ ($^1S_0$)) to the 3D line intensity (transition $2p^5$ 3d ($^3D_1$) → $2p^6$ ($^1S_0$)) is sensitive to the plasma electron temperature and has been the focus of much attention in the literature. During the history of disagreement between theory and observation for this line ratio, a number of underlying effects were found to be important, including blending with an inner shell satellite line of Fe XVI [77] and radiative cascades [78, 79]. In addition, Gu [80] explored the possibility that insufficient configuration-interaction was included in the atomic structure calculations leading to unconverged oscillator strengths. He then used an approximate method to account for this lack of convergence to modify the atomic collision data used in Fe XVII spectral modeling. A full discussion of the comparison of theory and experiment for this line ratio is outside of the scope of this chapter. Brown [81] presents a review of measurement results and Brown and Beiersdorfer [82] show a useful summary of the discrepancies and the effects that have been investigated. The focus of this chapter is on the analysis of a recent experiment using an X-ray Free Electron Laser (XFEL) that sought to identify the source of the aforementioned discrepancies [1].

Bernitt et al. [1] used an intense XFEL at the Linac Coherent Light Source (LCLS), employing the laser to excite Fe^{16+} ions in an Electron Beam Ion Trap (EBIT). The laser has a narrow bandwidth and was tuned to just populate the upper level of either the 3C or the 3D transition. In this two-level setup, the observed 3C/3D line intensity ratio was expected to be the same as the 3C/3D oscillator strength ratio, and any differences could be interpreted that the theoretical work was not accurately determining the atomic structure of Fe^{16+}. The experiment resulted in a much lower 3C/3D line intensity ratio (2.61 ± 0.13) than the previously calculated oscillator strength ratios, ~ 3.5 or higher. It was also pointed out that the 3C/3D oscillator strength ratio is only slowly converging with the increased size of the configuration-interaction expansion included in the theoretical calculations. The most complete theoretical calculations all produced oscillator strength ratios (3.5 [80], 3.54 [79] 3.42 [83], and 3.49 [1]) significantly larger than the observed line intensity ratio from the LCLS experiment.

To investigate the unexpectedly low 3C/3D line intensity ratio observed from the XFEL experiment, two approaches were adopted. A density-matrix (DM) approach first employed by Oreshkina et al. [2, 3] and reproduced in this chapter, showed that the 3C/3D line intensity ratio can be reduced below the expected oscillator strength ratio for sufficiently intense laser pulses and that the reduction is sensitive to certain laser pulse parameters (intensity, duration and bandwidth). Alternatively, Loch et al. [28] used a collisional-radiative (CR) method and showed that the spectral emission from the plasma after the laser pulse has left the plasma volume makes a strong contribution to the lowering of the 3C/3D line intensity ratio.

In this chapter both the CR and the DM approaches are summarized. The DM method is preferred for intense laser fields, due to the possible non-linear response of the excited populations with laser intensity and the phase of the electric field. In Section 6.2 both theoretical methods are described, in Section 6.3 the results using each method are shown, and in Section 6.4 some discussion and possible future directions are presented.

6.2 Theory

6.2.1 Collisional-Radiative Method

The CR method is used widely in laboratory and astrophysical plasma modeling. This approach takes into account all of the atomic process in a rate matrix, from which the steady-state and time-dependent populations can be evaluated. The laser bandwidth in the LCLS experiment was sufficiently narrow to ensure that only one transition in Fe^{16+} could be excited at a time, thus this could be treated as a two-level system. For both the 3C and 3D lines, the only populating mechanism for the excited state is photo-absorption from the ground level and the only associated depopulating mechanisms are stimulated emission (sometimes referred to as the interacting process) and spontaneous emission (the non-interacting process). The time-dependent population density for the excited state N_e and ground state N_g can be evaluated from:

$$\frac{dN_e}{dt} = N_g(t)\rho(\omega_0,t)B_{g\to e} - N_e(t)(A_{e\to g} + \rho(\omega_0,t)B_{e\to g}) \tag{6.1}$$

$$\frac{dN_g}{dt} = -N_g(t)\rho(\omega_0,t)B_{g\to e} + N_e(t)(A_{e\to g} + \rho(\omega_0,t)B_{e\to g}) \tag{6.2}$$

where $B_{g\to e}$, $B_{e\to g}$, $A_{e\to g}$ are the Einstein photo-absorption, stimulated emission and spontaneous emission coefficients, respectively. ω_0 is the angular frequency for the transition between the two levels. These can be evaluated from atomic structure calculations. ρ is the radiation field density (J/m^3/Hz) and can be determined from the laser parameters. In the DM approach the laser intensity I (W/cm^2) is used, so it is beneficial to be able to convert between the two representations via $\rho = I/(c \cdot \delta\nu)$. Here c is the speed of light and $\delta\nu$ is the bandwidth of the laser (e.g. $I = 10^{10}$ W/cm^2 $\to \rho = 1.10 \times 10^{-9}$ J/m^3/Hz). In order to solve the time-dependent Eqs. (6.1) and (6.2), the matrix form is used:

$$\begin{bmatrix} dN_g/dt \\ dN_e/dt \end{bmatrix} = \begin{bmatrix} -\rho(\omega_0,t)B_{g\to e} & A_{e\to g}+\rho(\omega_0,t)B_{e\to g} \\ \rho(\omega_0,t)B_{g\to e} & -(A_{e\to g}+\rho(\omega_0,t)B_{e\to g}) \end{bmatrix} \begin{bmatrix} N_g \\ N_e \end{bmatrix}. \tag{6.3}$$

Initially, one hundred percent of the population is fixed to be in the ground state. Thus, the initial normalized population vector is $\begin{bmatrix} 1 & 0 \end{bmatrix}^T$, where the superscript T indicates the transpose. The excited state population $N_e(t)$ is evaulated for a given $\rho(t)$ using Eq. (6.3). This can then be used to determine the photon emission for the time during which the laser pulse is in the plasma volume. Note that while stimulated emission is included in the modeling of the excited population density (see Eq. (6.3)), these photons are not counted in the predicted line intensity (see Eq. (6.4)) since the stimulated emission photons are emitted in the direction of the laser beam and not towards the detector. After the laser pulse has left the plasma volume, there will be a number of electrons left in the excited state. All of these will decay via spontaneous emission before the next laser pulse. Thus, there is a second contribution to the line emission with each of these excited state electrons producing one photon. That is, the total photon energy detected in the spectral line will be proportional to:

$$I^{photon}_{e\to g} = \hbar\omega_0 A_{e\to g}\int_0^T N_e(t)dt + \hbar\omega_0 N_e(T). \tag{6.4}$$

The first term on the right hand side represents the emission during the time, indicated by T, that the laser pulse is interacting with the EBIT plasma and the second term represents the contribution to the emission from the plasma after the laser pulse has passed. Clearly the laser pulse temporal profile is a key factor in evaluating the time-dependent excited populations. Various envelopes for $\rho(t)$ have been considered.

6.2.2 Density-Matrix Method

The DM approach is a different formalism. For a two-level system in a stationary state, the ground and excited levels have eigenvalues $\hbar\omega_g$ and $\hbar\omega_e$, and wave functions $\Psi_g(\vec{r})$ and

$\Psi_e(\vec{r})$ in the Heisenberg picture. The total wave function of the system can be expressed as:

$$\Psi(\vec{r},t) = C_g(t)\Psi_g(\vec{r}) + C_e(t)\Psi_e(\vec{r}). \tag{6.5}$$

The density operator is defined as $\rho{=}\left|\Psi\right\rangle\left\langle\Psi\right|$, which has the form

$$\rho = \begin{bmatrix} \left\langle g\right|\rho\left|g\right\rangle & \left\langle g\right|\rho\left|e\right\rangle \\ \left\langle e\right|\rho\left|g\right\rangle & \left\langle e\right|\rho\left|e\right\rangle \end{bmatrix} = \begin{bmatrix} \frac{N_g}{N_g+N_e} & C_gC_e^* \\ C_eC_g^* & \frac{N_e}{N_g+N_e} \end{bmatrix} \tag{6.6}$$

where $\frac{N_g}{N_g+N_e}$ and $\frac{N_e}{N_g+N_e}$ are referred to as the populations and the products $C_gC_e^*$ and $C_eC_g^*$ are referred to as the coherence terms. For systems interacting with a laser, the Hamiltonian of the system can be written as:

$$H = H_S + H_I, \tag{6.7}$$

where the first term represents the stationary Hamiltonian given by

$$H_S = \hbar\omega_g\left|\Psi_g\right\rangle\left\langle\Psi_g\right| + \hbar\omega_e\left|\Psi_e\right\rangle\left\langle\Psi_e\right| \tag{6.8}$$

and the second term represents the interaction Hamiltonian

$$H_I = -\vec{D}\cdot\vec{E}, \tag{6.9}$$

where $\vec{D}$ is the dipole moment and $\vec{E}$ is the radiation field. For a linearly polarized electric field along the z-axis, it can be written as $\vec{E} = E_0(t)\cos(\omega_L t + \psi(t))\vec{z}$, where $E_0(t)$ is the electric field amplitude. $E_0(t)$ can be determined from the radiation field intensity I via $I = \frac{1}{2}c\epsilon_0 nE_0$, where c is the speed of the light, ϵ is the electric permittivity of free space, and n is the refractive index of the medium. ω_L is the angular frequency of the laser and $\psi(t)$ is the time-dependent phase of the laser field. Using the rotating-wave-pproximation (RWA), the interaction Hamiltonian can be further expanded as

$$H_I = -\frac{\hbar\Omega^*}{2} |e\rangle \langle g| e^{-i\omega_L t} - \frac{\hbar\Omega}{2} |g\rangle \langle e| e^{i\omega_L t}, \tag{6.10}$$

where Ω is the Rabi-frequency given by $\Omega = E_0(t)D_{eg}e^{i\psi(t)}/\hbar$, with $D_{eg} = e\langle e| \hat{z} |g\rangle$ being the eletric dipole matrix element. The density operator ρ is governed by the equation:

$$\frac{d\rho}{dt} = \frac{1}{i\hbar}[H, \rho] + \Lambda\rho \tag{6.11}$$

where Λ is the decay term due to spontaneous emission. From Eq. (6.11), one can show that:

$$\frac{d\rho_{gg}}{dt} = \Gamma\rho_{ee} - \frac{i\Omega^*}{2}e^{-i\omega_L t}\rho_{ge} + \frac{i\Omega}{2}e^{i\omega_L t}\rho_{eg} \tag{6.12a}$$

$$\frac{d\rho_{ee}}{dt} = -\Gamma\rho_{ee} + \frac{i\Omega^*}{2}e^{-i\omega_L t}\rho_{ge} - \frac{i\Omega}{2}e^{i\omega_L t}\rho_{eg} \tag{6.12b}$$

$$\frac{d\rho_{eg}}{dt} = \frac{i\Omega^*}{2}e^{-i\omega_L t}\rho_{gg} - \frac{i\Omega^*}{2}e^{i\omega_L t}\rho_{ee} - (i\omega_0 + \frac{\Gamma}{2})\rho_{eg}. \tag{6.12c}$$

By using $\rho_{ge} = \rho_{ge}^*$, it is straightforward to get the expression for $\frac{d\rho_{ge}}{dt}$. By defining a new variable $\tilde{\rho} = e^{i\omega_L t}\rho$ and a detuning parameter $\Delta = \omega_L - \omega_0$, Eqs. (6.12a) to (6.12c) can be rewritten as follows:

$$\frac{d\rho_{gg}}{dt} = \Gamma\rho_{ee} - \frac{i\Omega^*}{2}\tilde{\rho}_{ge} + \frac{i\Omega}{2}\tilde{\rho}_{eg} \tag{6.13a}$$

$$\frac{d\rho_{ee}}{dt} = -\Gamma\rho_{ee} + \frac{i\Omega^*}{2}\tilde{\rho}_{ge} - \frac{i\Omega}{2}\tilde{\rho}_{eg} \tag{6.13b}$$

$$\frac{d\tilde{\rho}_{eg}}{dt} = \frac{i\Omega^*}{2}\rho_{gg} - \frac{i\Omega^*}{2}\rho_{ee}(i\Delta - \frac{\Gamma}{2})\tilde{\rho}_{eg}. \tag{6.13c}$$

From Eqs. (6.13a) to (6.13c) one can produce the Optical-Bloch equation

$$\begin{bmatrix} d\rho_{gg}/dt \\ d\rho_{ee}/dt \\ d\tilde{\rho}_{ge}/dt \\ d\tilde{\rho}_{eg}/dt \end{bmatrix} = \begin{bmatrix} 0 & \Gamma & -\frac{i\Omega^*}{2} & \frac{i\Omega}{2} \\ 0 & -\Gamma & \frac{i\Omega^*}{2} & -\frac{i\Omega}{2} \\ -\frac{i\Omega^*}{2} & \frac{i\Omega^*}{2} & 0 & -i\Delta - \frac{\Gamma}{2} \\ \frac{i\Omega^*}{2} & -\frac{i\Omega^*}{2} & 0 & i\Delta - \frac{\Gamma}{2} \end{bmatrix} \begin{bmatrix} \rho_{gg} \\ \rho_{ee} \\ \tilde{\rho}_{ge} \\ \tilde{\rho}_{eg} \end{bmatrix}. \tag{6.14}$$

The electric field amplitude $E_0(t)$ should be a profile consistent with the laser pulse of the experiment. Oreshkina et al. [2, 3] use a Gaussian envelope with a constant phase, and a Gaussian envelope with a random phase (evaluated with the partial coherent method (PCM) [84, 85]). These two cases are considered here, in addition to the case of the homogeneous envelope.

To solve Eq. (6.14), it is assumed that initially one hundred percent of the population is in the ground state (i.e., one starts with $\begin{bmatrix} 1 & 0 & 0 & 0 \end{bmatrix}^T$ for the density vector). The energy detected from the line emission can be expressed as a function of the detuning parameter

$$E(\Delta) \propto \Gamma\omega_0 \int_{-\infty}^{+\infty} \rho_{ee}(t)dt, \tag{6.15}$$

with $\rho_{ee}(t)$ being evaluated from Eq. (6.14). The line intensity is then evaluated from an integral over the detuning parameter:

$$L = \int E(\Delta)d\Delta. \tag{6.16}$$

Note that the laser pulse parameters are included in the DM approach via the the electric field ($\vec{E}$), with the pulse envelope imposed on $E_0(t)$ and the time dependence of the phase of the electric field included in $\psi(t)$. The CR approach includes the intensity profile of the laser via the radiation field density ($\rho(t)$) but does not include the phase of the electric field. The Einstein A and B coefficients are related via the detailed balance relationships and thus the CR method can be thought of as the limiting case for a perfectly incoherent field.

As part of this work, codes were developed for both the CR and DM methods. The CR results have been presented in the literature [28]. Here we show the DM results for the same conditions as those of Oreshkina et al. [2, 3], to test their conclusions. Also, in the following section CR results will be shown which use identical Einstein A-coefficients as the DM calculations and the radiation field densities will also be converted to the equivalent laser intensities. Note that the two methods should not be expected to produce equivalent results, even for low radiation field densities, as they treat the coherence effects differently. It is nevertheless interesting to show the results from both approaches, which are presented in the next section.

6.3 Results

6.3.1 LCLS parameter estimation

The LCLS XFEL parameters for the experiment are described by Bernitt et al. [1] and on the LCLS web page [1]. The modeling results require the radiation field density parameters (for the CR results) and the laser intensity parameters (for the DM results). From Bernitt et al. [1], the laser pulses vary in duration from 200 to 2000 fs, but mostly within the range of 200–500 fs (G.V. Brown, private communication). The total energy per laser pulse in the experiment has an upper limit of 3 mJ. However the filtering and optical losses after the soft X-ray (SXR) monochromator are expected to reduce the total energy per shot to 0.0013–0.39 mJ [28]. The LCLS XFEL focal diameter has a range of 3–10 μm [86]. A value of 10 μm was chosen for the modeling to make the beam weakly focused. Note that the possibility that the beam had a much larger diameter will be considered later in this chapter. These parameters result in a radiation field density (ρ) of 4.62×10^{-7} – 3.46×10^{-4} J/m^3/Hz, and using a laser bandwidth of 1.0 eV the corresponding laser intensity would be in the range

---

[1] https://portal.slac.stanford.edu/sites/lcls_public/Instruments/SXR/Pages/Specifications.asp

$4.18 \times 10^{12} - 3.14 \times 10^{15}$ W/cm^2. Oreshkina et al. [2, 3] estimated the laser intensity to be in the range $10^{11} - 10^{14}$ W/cm^2. They used a larger focal diameter than the one given above and also a larger energy per pulse (3 mJ).

The other important characteristic about the LCLS XFEL pulses is their stochastic nature. Each pulse consists of many short spikes a few fs in duration, with gaps between the spikes also being a few fs long. The phase during each of the spikes is in general not coherent with the previous spikes. Thus, both the intensity and the phase are stochastic in nature for each pulse. In the case-studies presented below we first consider the line intensity ratio for individual homogeneous pulses to illustrate the mechanism for the lowering of the line intensity ratio. We then introduce stochastic pulses and evaluate the line ratio for a large number of stochastic pulses to simulate the experimental conditions as closely as possible.

6.3.2 CR model

The CR results for these LCLS laser parameters using a number of pulse profiles for $\rho(t)$ are considered first. Einstein A-coefficients of 2.22×10^{13} s^{-1} and 6.02×10^{12} s^{-1} for the 3C and 3D A-values were used, taken from the largest calculation shown in [2, 3]. The purpose here is to demonstrate the mechanism for the reduction in the 3C/3D line intensity ratio, with the conclusions being independent of the precise values chosen for the A-values.

Smooth homogeneous pulse

Considering first a pulse with a radiation field density that is homogeneous in time, the time-dependent populations can be solved using Eq. (6.3) and the 3C/3D line intensity ratio determined using Eq. (6.4). Fig. 6.1 shows the excited states population for the upper levels of the 3C and 3D transitions for a range of pulse intensities. Both excited state populations increase towards a constant (steady-state) value during the homogeneous pulse. However, due to the different Einstein A coefficients for the 3C and 3D transitions, the two excited states converge onto this value at different rates. The excited state population for

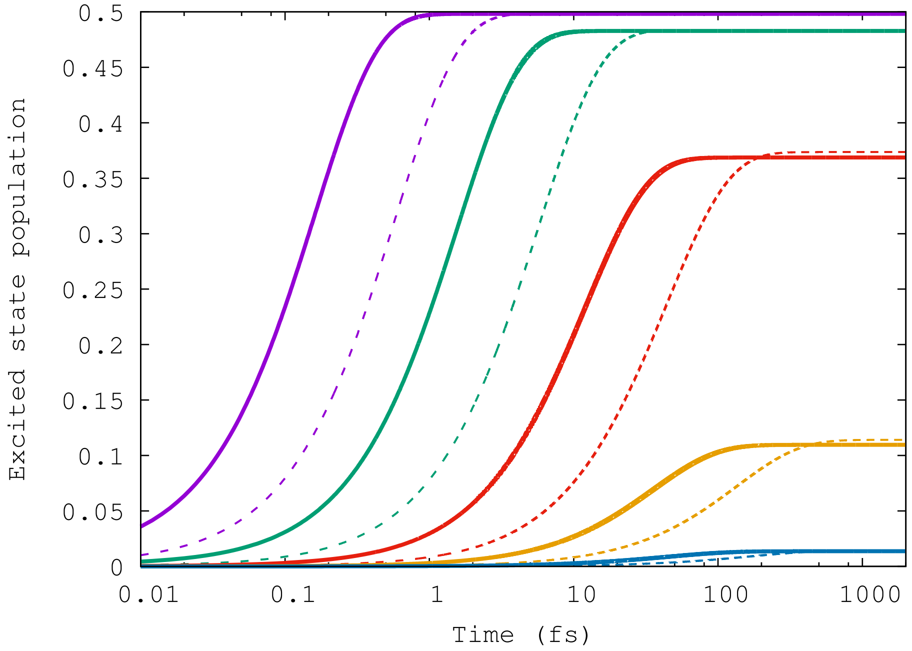

Figure 6.1: Excited state fractional population ($N_e/(N_e + N_g)$) as a function of time for a homogenous radiation field density using the CR method. The solid lines shows the upper level populations for the 3C transition and the dashed lines show the upper level populations for the 3D transition. Results are shown for laser intensities of 10^{15} W/cm^2 (purple), 10^{14} W/cm^2 (green), 10^{13} W/cm^2 (red), 10^{12} W/cm^2 (yellow), and 10^{11} W/cm^2 (blue).

the upper level of the 3C line reaches steady-state in a shorter time than the corresponding 3D population. For low radiation field densities the steady-state population value depends linearly on the radiation field density and results in an excited state population fraction that is less than 0.5. As the radiation field density increases, the excited states reach their steady-state value in a much shorter time and the steady-state value is no longer directly proportional to the radiation field density. It can also be seen that the maximum value for the steady-state excited population fraction is 0.5, the high radiation field density limit for the excited population in the CR method. In this case, the populating and depopulating of the excited states happen simultaneously, in other words the process is always incoherent, which leads to steady and non-oscillating excited state populations.

The 3C/3D line intensity ratio for a homogenous radiation field density is shown in Fig. 6.2. For laser intensities above approximately 1 × 10^{12} W/cm^2 there is a reduction

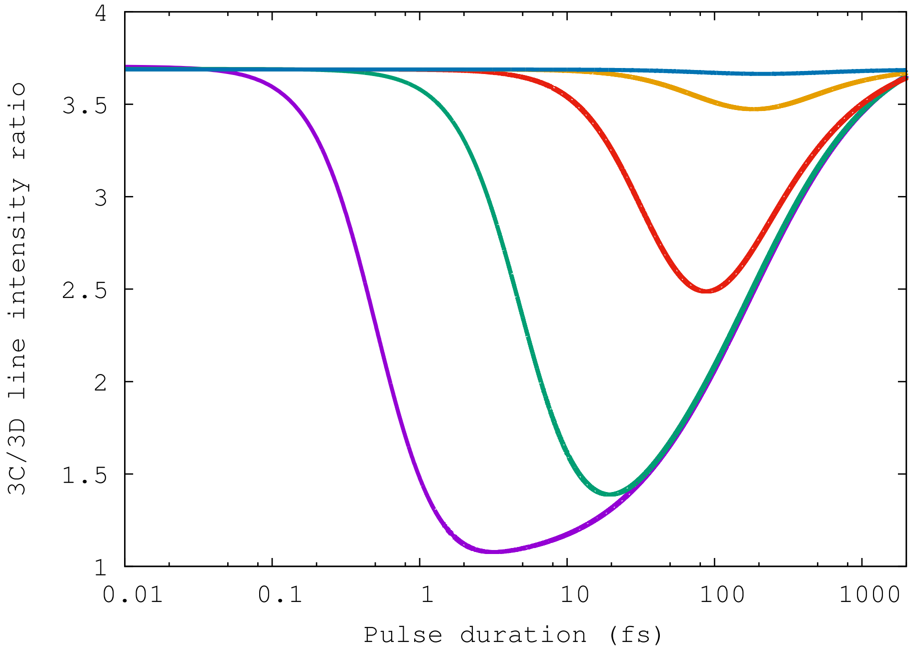

Figure 6.2: The 3C/3D line intensity ratio as a function of pulse duration for a homogenous radiation field density using the CR method. Results are shown for laser intensities of 10^{15} W/cm^2 (solid purple line), 10^{14} W/cm^2 (solid green line), 10^{13} W/cm^2 (solid red line), 10^{12} W/cm^2 (solid yellow line), 10^{11} W/cm^2 (solid blue line).

in the line intensity ratio below the oscillator strength ratio value. The reduction was shown previously [28] to be primarily due to contributions to the emission during the XFEL interaction with the plasma being different from the contribution after the pulse has left the plasma volume. For the intense pulses, the 3D intensity always has a larger fraction of its emission coming from this 'after the pulse' component than the 3C intensity. This results in a reduction in the line intensity ratio below the oscillator strength ratio value.

Stochastic pulse

Consider next the CR results for a stochastic profile of the pulse. We generate a random set of Gaussian profiles, each with 0.2 fs standard deviation and remove a random number of Gaussians to produce a pulse profile similar to that shown on the LCLS web page, see Fig. 4 of Loch et al. [28]. We normalize the stochastic pulse profile so that the integrated intensity is equivalent to a homogeneous radiation field density. We then use this value to label the stochastic pulse, which allows us to compare the two sets of results.

Fig. 6.3 shows the comparison of line ratio using the CR method with both the homogeneous and stochastic pulses. The stochastic features of the pulse profiles do not change the overall trend of the line ratio using the CR model. This is because the stochastic laser intensity spikes have only small (i.e., a few fs) gaps between them. Thus, for intense pulses the excited populations are still driven close to their steady-state values and do not have time to decay significantly during the gap between the spikes. In the stochastic simulations we use different pulses for the 3C and 3D transitions, and have many pulses for each set of pulse parameters. Each point in Fig. 6.3 was generated using 80 stochastic pulse profiles for the 3C and 80 pulses for the 3D. Note the stochastic pulse simulations produce a similar reduction in the line ratio to that obtained from the homogeneous pulse calculations, i.e. the 3C/3D line ratios are lower for shorter and intense pulses. Note that the experiment would have involved a large number of pulses of different intensities and pulse durations. If the distribution of pulse conditions was known, then it would be possible to compare with a simulated line ratio for the same set of pulse distributions. Such a simulation could be used to explore the sensitivity to the A-values employed in the model, resulting in a recommended range of values on the A-value ratio. While the experimental distribution of pulse conditions is not currently known well enough to perform such a comparison, it should be pointed out that the CR model implies that pulse intensities above 10^{12} W/cm^2 are required to produce a reduction in the line ratio.

6.3.3 DM model

We next consider the DM approach for different pulse envelopes. The same laser bandwidth (1.0 eV) and A-values are used as those chosen by Oreshkina et al. [2, 3], to allow a direct comparison to be made with their results. As in the discussion of the CR section, the

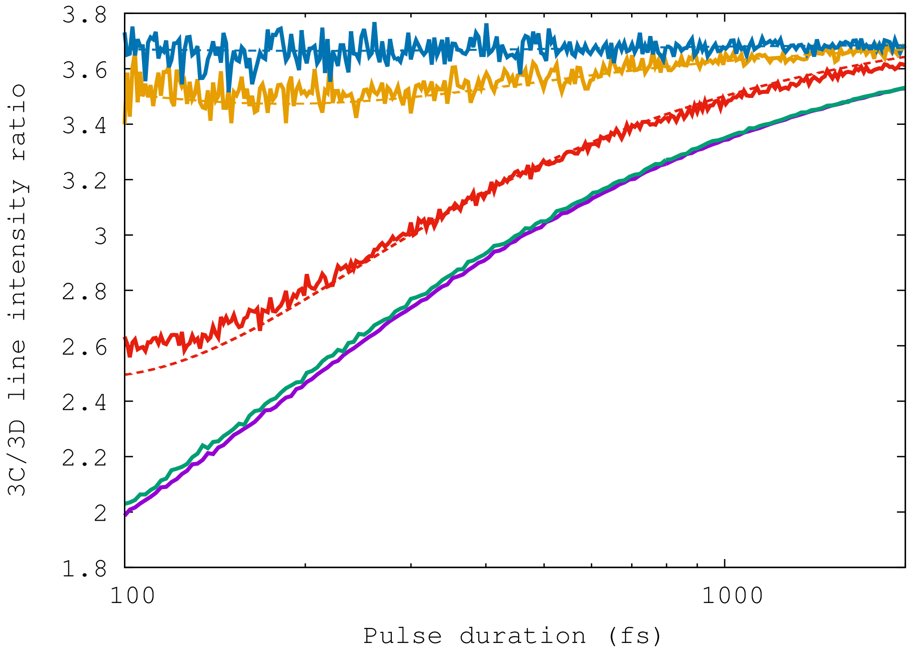

Figure 6.3: The 3C/3D line intensity ratio as a function of pulse duration. The stochastic results take an average of 80 stochastic pulses for each data point. The homogeneous results are the same as those shown in Fig. 6.2. The solid lines show the stochastic results and the dashed lines show the homogeneous data. Results are shown for intensities of 10^{15} W/cm^2 (purple), 10^{14} W/cm^2 (green), 10^{13} W/cm^2 (red), 10^{12} W/cm^2 (yellow), 10^{11} W/cm^2 (blue).

conclusions that are drawn here will be general and not dependent upon the specific values chosen for the A-values for Fe^{16+}.

Smooth homogeneous pulse

In the DM approach, the level populating and depopulating mechanisms are slightly different from the CR model, as the process involves an intermediate step which contains two polarization states, ρ_{ge} and ρ_{eg}. This characrteristic enables the Rabi-oscillation of the populations and is required for intense radiation fields and coherent systems.

We consider first a homogeneous pulse, that is $E_0(t)$ is a constant in time, with the value determined from the laser intensity. Eq. (6.14) is used to evaluate the time-dependent populations and Eq. (6.16) is used to evaluate the Fe XVII 3C/3D line intensity ratio. Fig. 6.4 shows the excited state populations as a function of time using the DM approach for a range of homogeneous pulse intensities. For low intensities the populations increase smoothly to a steady-state value, with a similar shape to the CR results. There is, however, a noticeable difference: the steady-state value can be different for the two transitions. It can also be seen that the 3C excited population reaches steady-state in a shorter time than the 3D excited population. At higher intensities ($\sim 10^{11}$ W/cm^2 and above), Rabi-flopping starts to become apparent in both the 3C and 3D populations. Thus, the duration of the pulse can make a large difference in the relative emission for the two lines. One pulse could result in a 3C excited population that is greater than the 3D excited population, while a slightly longer pulse could lead to the opposite. It can also be seen that for the DM method for coherent pulses, the 3C/3D line ratio could be higher than or smaller than the oscillator strength ratio, depending upon the relative populations of the two excited states. This will be shown in more detail in the next section.

Coherent Gaussian pulse

Oreshkina et al. [2, 3] modeled the Fe XVII experiment using a DM approach with a Gaussian profile as the pulse envelope. We consider the same case here, to allow us to compare our DM results with theirs. We start with pulses possessing a coherent phase for the duration of the pulse ($\psi(t) = 0$). Fig. 6.5 shows the time evolution of the excited population fractions for a pulse with intensity of 1×10^{13} W/cm^2 and two different pulse durations (100 fs and 200 fs), showing characteristic Rabi-flopping. The Rabi-frequency of the 3C populations is more rapid than the 3D, due to the larger A-value for the 3C transition. This difference in Rabi-frequency can result in quite different excited populations at the end of the laser pulse interaction with the plasma. Considering these two pulse durations as an illustrative example: for the 100 fs case, the 3D transition has a much larger excited population at the end of the pulse than the 3C excited population, while for the 200 fs case the two have almost the same population fraction. This behavior drives the 3C/3D line intensity ratio for the 100 fs case to be much smaller than the oscillator strength value. Clearly one would not expect the line intensity ratio produced from these populations to be equivalent to the oscillator strength ratio. Furthermore, the contribution to the emission from the time after the laser pulse has left the plasma volume is quite sensitive to the population in the excited state at the end of the laser pulse. Again one has the scenario where the emission from the 'after-the-pulse' component will be quite different in the two cases, producing quite different line ratio values for these two pulses.

Fig. 6.6 shows the 3C/3D line ratio as a function of pulse duration for coherent Gaussian pulses. We obtain very similar line ratio results to those of Oreshkina et al. [2, 3]. It is useful to consider the two pulse durations shown in Fig. 6.5. The 3C/3D line ratios for the two scenarios shown in Fig. 6.5 are shown by the purple and green square in Fig. 6.6. For the 100-fs pulse (where the 3D population fraction is greater than the 3C value at the end of the pulse), the line ratio is 1.55 which is much smaller than the 3C/3D oscillator strength ratio, as one might expect from the populations. For the 200-fs pulse (where the 3D population fraction is about the same as the 3C at the end of the pulse), the ratio is 5.38. Fig. 6.6 also shows that for coherent pulses a change in the line ratio from the oscillator strength ratio requires pulse intensities above about 1×10^{11} W/cm^2.

Stochastic Gaussian pulse

To model the LCLS pulse parameters more accurately, the stochastic features of the pulse need to be included. We use the PCM [84, 85] to model the stochastic nature of the pulse intensity and phase. Fig. 6.7 shows a stochastic pulse intensity generated using the PCM. Note that it still has a Gaussian envelope, but there are now many stochastic spikes of intensity throughout the pulse. Note also that the electric field strength and the phase are both stochastic and complex. These stochastic pulses can now be modeled using the DM formalism to produce a 3C/3D line intensity ratio. Fig. 6.8 shows the comparison of the calculated 3C/3D line intensity ratio with the results of Oreshkina et al. [2, 3]. The line ratio results are calculated from an average of 80 pulses using a bandwidth of eV, and the results are in good agreement with Oreshkina el al. [2, 3]. We were, however, not able to achieve convergence within 10 or 20 pulses as stated in their paper; in general it took more runs to achieve convergence on the average line ratio value. The calculated line ratios are all below the oscillator strength ratio for intensities above $\sim 10^{12}$ W/cm^2. The bandwidth of the pulse also affects the coherence of the pulse and the duration of the spikes in the intensity, thus it strongly affects the line ratio. If the bandwidth is very small, then the pulse profile becomes much more coherent and the spikes in intensity are wide. In this limit the stochastic pulses produce line ratio values very close to the coherent Gaussian pulses from Fig. 6.6.

It should also be noted that the emission from the plasma after the pulse has left the plasma volume is still a strong factor in lowering the line intensity ratio below the oscillator strength value. Fig. 6.9 shows the 3C/3D line ratio if only the emission during the pulse interaction with the plasma is included. The results of Oreshkina [2, 3] are also shown for comparison to highlight the effect of the ‘after-the-pulse’ contribution to the line emission.

The ratio values are all significantly increased, producing values above the oscillator strength ratio value. Thus, the contribution from the emission after the pulse is an important factor in producing a 3C/3D line intensity ratio that is lower than the oscillator strength value for both the CR and DM approaches.

As a final illustration of the results using the DM approach, a simulation was carried out for a distribution of pulse intensities and pulse durations. Using a laser bandwidth of 1.0 eV, a distribution of pulse intensities, with 10 evenly spaced points per decade from 10^{11} to 10^{14} W/cm^2, and a distribution of linearly spaced pulse durations ranging from 200 to 500 fs, a total line intensity for the 3C and 3D lines was produced. The two total line intensities were then used to produce a 3C/3D line intensity ratio, giving a value of 2.71. It should be noted that the pulse parameters and distributions are not well known from the experiment, so this type of investigation should not be considered to be a true simulation of the experiment, but an illustration that pulse parameters in this range of intensities and durations can produce a line intensity ratio close to the value that was measured. For the A-values chosen for this simulation, some pulse intensities at (or above) 10^{13} W/cm^2 are required to produce line ratios in the range measured by the experiment. It would clearly be very useful to be able to use the observed line intensity ratio, and knowledge of the pulse parameters, to determine what the 3C/3D A-value ratio would need to be to produce agreement with the experiment (i.e., to make no assumption about the A-values for either line, but to determine the ratio from the experiment). However, without more accurate knowledge of the pulse parameters, this does not currently appear to be possible. The next section explores this in more detail.

Photon counts

If the laser intensity is significantly below 10^{11} W/cm^2, one would expect the line intensity ratio to be close to the oscillator strength ratio. In recent discussion with the experimentalists, it was pointed out to us that the defocusing of the laser would produce a beam much more weakly focused than we assumed in our model. While we had assumed a beam radius of 5 μm, it was likely to be closer to 0.5 mm (FWHM), i.e. a factor of 100 times wider. This change would produce intensities a factor of 10^4 weaker, so the range of pulse intensities would be $4.18 \times 10^8 - 3.14 \times 10^{11}$ W/cm^2. In this range, the measured line intensity ratio would be expected to be the same as the oscillator strength ratio.

It is instructive to consider the photon counts produced from each pulse, remembering that the LCLS experiment consisted of a large number of individual pulses, with the final line intensity being the result from all of the pulses combined. Fig. 6.10 shows the photon emission as a function of pulse intensity. The weak pulses produce only a few photons, and the number of photons produced increases linearly with pulse intensity until about 10^{12} W/cm^2. Thus, the more intense pulses produce more photons from the plasma. For the line intensity ratio to be dominated by the pulse intensities in the $4.18 \times 10^8 - 3.14 \times 10^{11}$ W/cm^2 range, it would be very important that no pulses had intensities above this range. It would only take a few pulses above 10^{13} W/cm^2 for those pulses to dominate the line intensities, and hence the line ratio. This topic will be explored in future work. It would also be of great benefit if an experiment could be performed where no pulses with intensities above $\sim 10^{12}$ W/cm^2 were allowed to interact with the plasma. In such an experiment, the observed line intensity ratio is expected to be a good indication of the 3C/3D oscillator strength ratio.

6.4 Summary

A review has been presented of two time-dependent methods that have been used to model the Fe XVII 3C/3D line intensity ratio for an intense laser field, the CR and DM approaches. Both methods show a reduction in the line intensity ratio below the oscillator strength ratio for pulses with intensities above $\sim 10^{12}$ W/cm^2. A significant factor in lowering the line ratio for both methods is the contribution to the emission from the plasma after the laser pulse has left the plasma volume. We confirm the importance of the effects previously reported by Oreshkina et al. [2, 3]: the non-linear effects in the DM method and the stochastic nature of the laser pulses. Further knowledge of the distribution of laser pulse parameters, or future experiments with no pulse intensities above $\sim 10^{12}$ W/cm^2, would allow an accurate evaluation of the 3C/3D oscillator strength ratio.

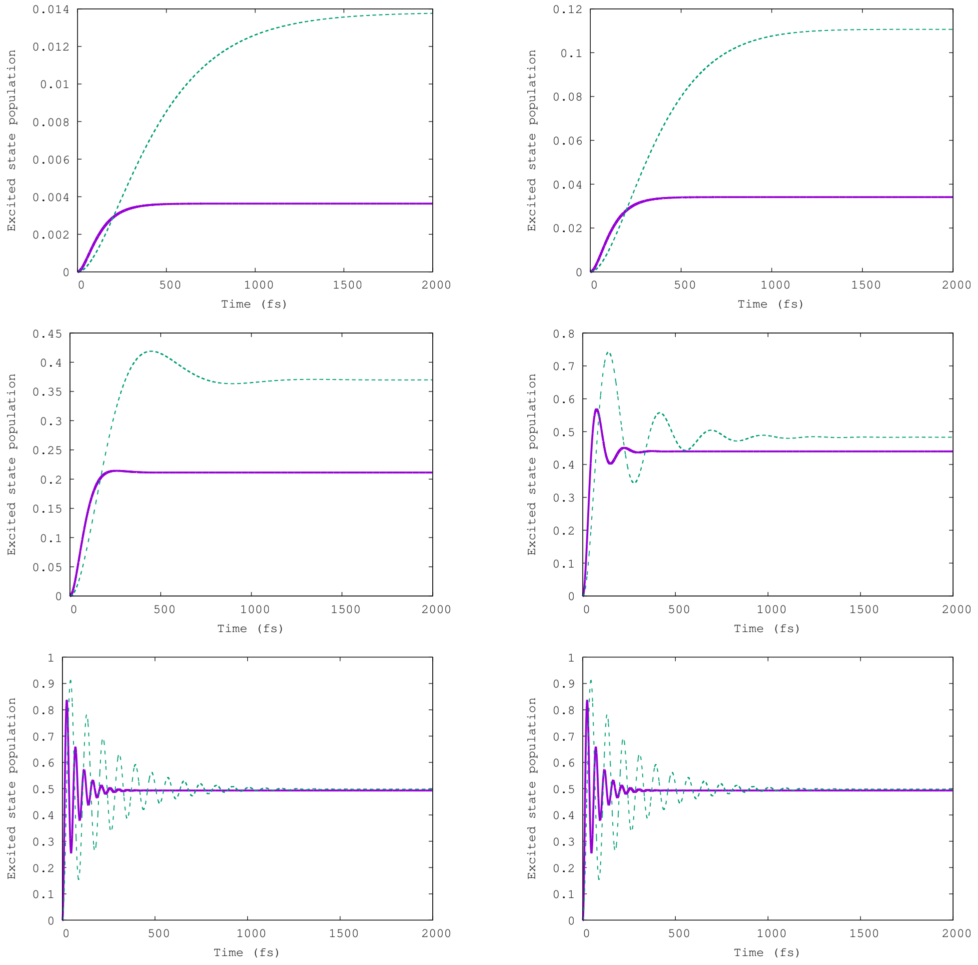

Figure 6.4: Excited state fractional populations as a function of time under a continuous flat pulse using the DM approach. The solid purple lines show the excited 3C populations and the dashed green lines show the excited 3D populations. Results are shown for 10^9?W/cm^2 (row 1, column 1), 3C at 10^{10} W/cm^2 (row 1, column 2), 3C at 10^{11} W/cm^2 (row 1, column 2), 3C at 10^{12} W/cm^2 (row 2, column 2), 3C at 10^{13} W/cm^2 (row 3, column 1), 3C at 10^{14} W/cm^2 (row 3 column 2).

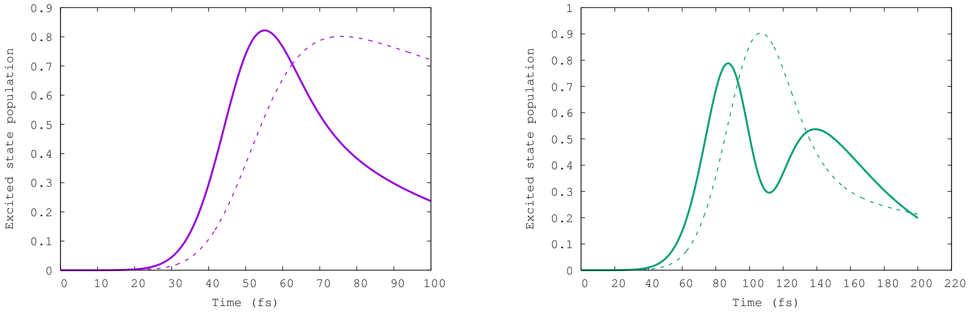

Figure 6.5: Excited state fractional populations as a function of time for a Gaussian pulse with intensity 10^{13} W/cm^2 using the DM Model. The left panel displays the 100-fs results: the solid (purple) line indicates the 3C population and the dashed (purple) line indicates the 3D population. The right panel displays the 200-fs results: the solid (green) line indicates the 3C population and the dashed (green)line indicates the 3D population.

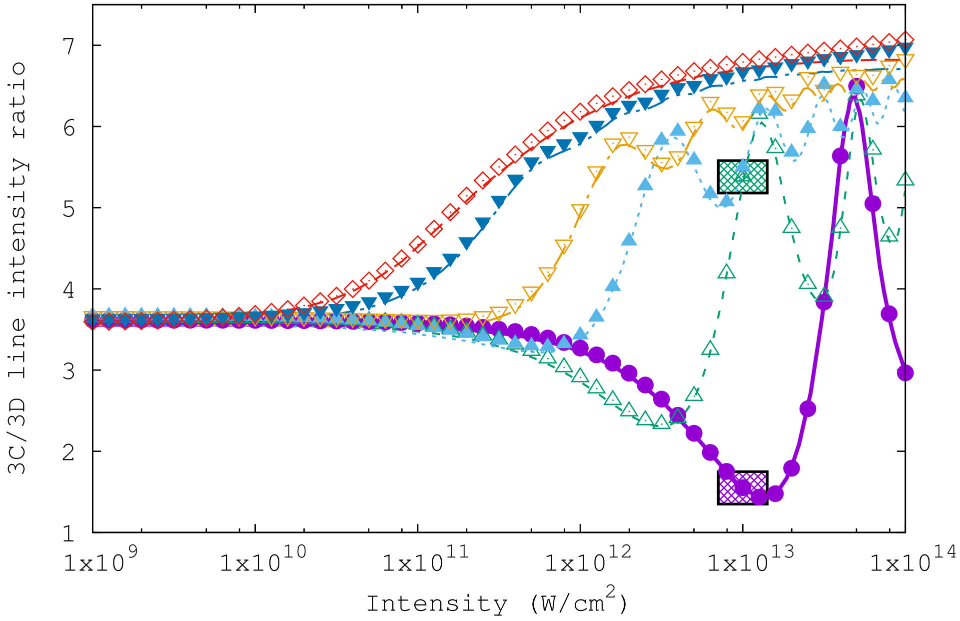

Figure 6.6: 3C/3D line intensity ratio as a function of radiation field intensity under a Gaussian pulse using the DM Model compared with Oreshkina el al. [2, 3]. In all cases the symbols show the results from the work of this chapter and the lines show the results of Oreshkina et al. [3]. Results are shown for 100 fs (purple), 200 fs (green), 400 fs (blue), 600 fs (yellow), 1200 fs (dark blue), and 2000 fs (red).

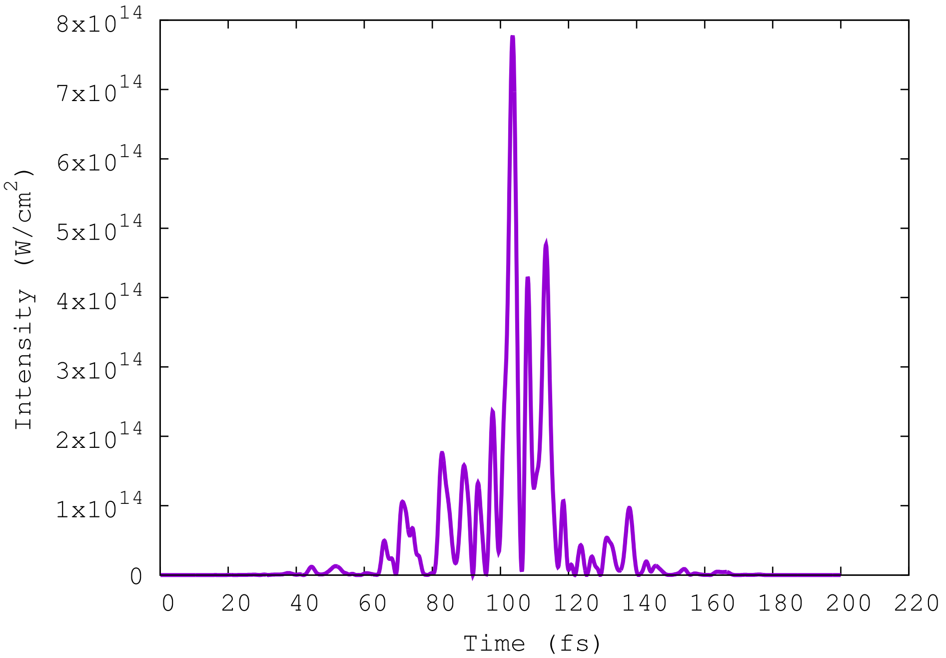

Figure 6.7: A sample stochastic pulse with Gaussian envelope for a 200 fs pulse duration.

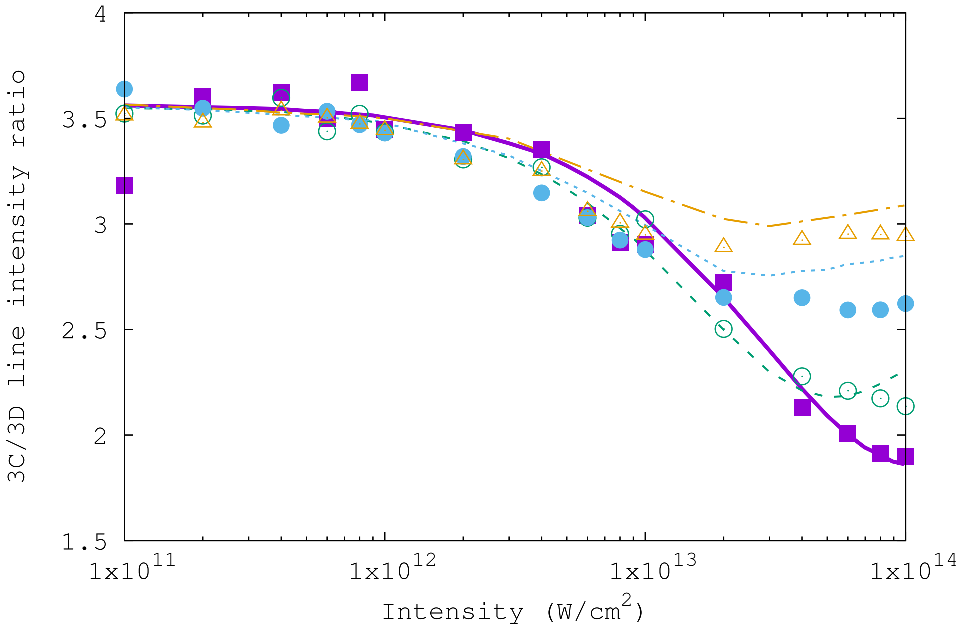

Figure 6.8: The 3C/3D line intensity ratio as a function of radiation field intensity for a stochastic Gaussian pulse using the DM model. The symbols show the current results and the lines show the results of Oreshkina et al. [2]. Results are shown for 100 fs (purple), 200 fs (green), 400 fs (blue), and 600 fs (yellow).

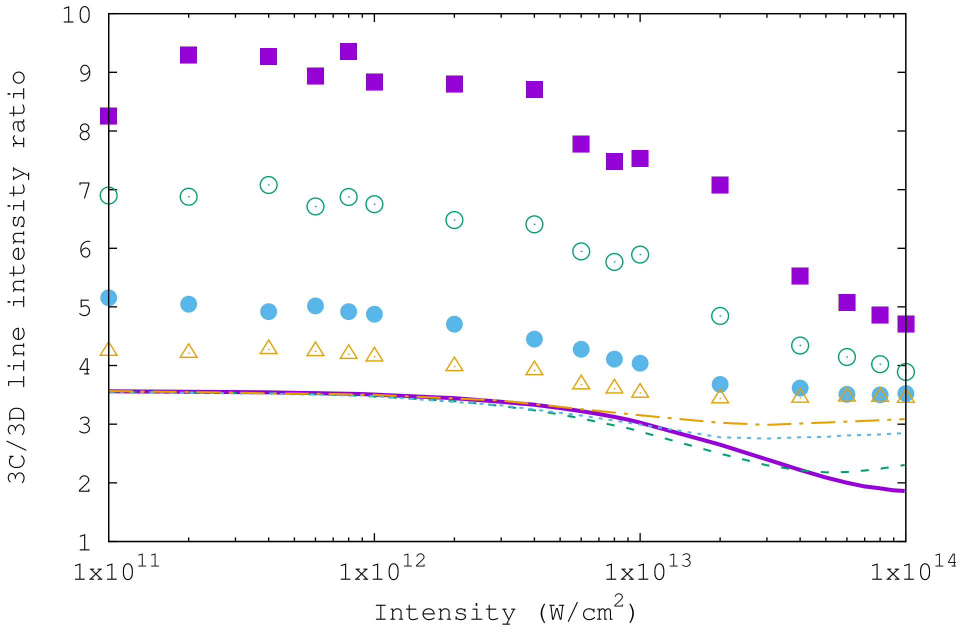

Figure 6.9: The 3C/3D Line intensity ratio as a function of radiation field intensity with no contribution to the emission from the time after the laser has left the plasma volume. The symbols show the current results and the lines show the results of Oreshkina et al. [2]. Note that the Oreshkina et al. [2] results include the contribution to the line intensity ratio due to the emission after the laser pulse has left the plasma volume. Results are shown for 100 fs (purple), 200 fs (green), 400 fs (blue), and 600 fs (yellow).

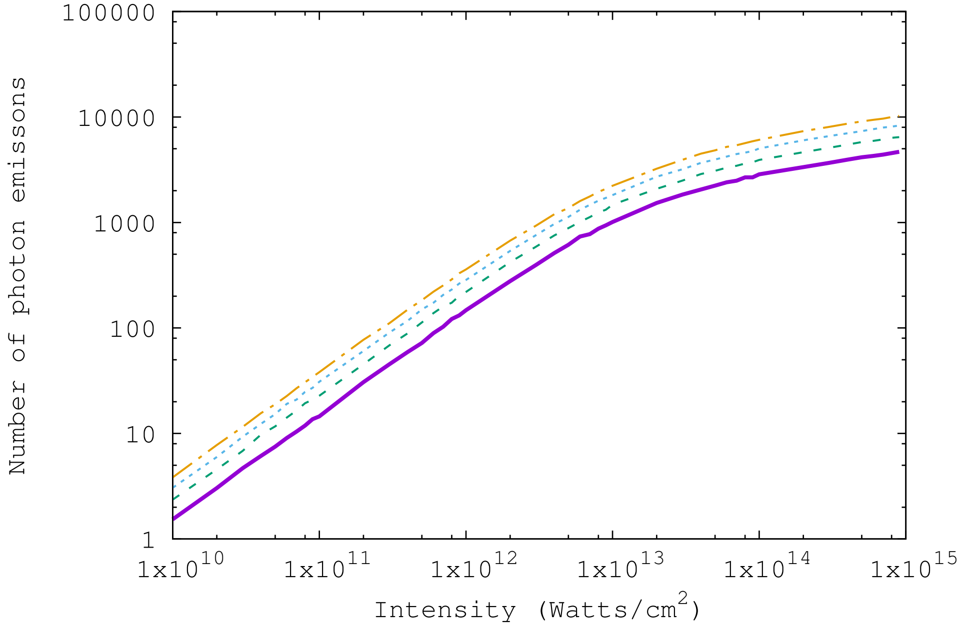

Figure 6.10: Averaged photon counts for the 3C line as a function of radiation field intensity for stochastic Gaussian pulses using the DM model. Results are shown for 200 fs (solid purple line), 300 fs (dashed green line), 400 fs (dotted blue line), and 500 fs (dot-dashed yellow line).

Chapter 7

Summary and Future Work

Results have been presented using the time-dependent close-coupling method for photon interactions with a number of systems. A TDCC method has been used to calculate 5 photon double ionization of Helium atom. It is found that due to the presence of mixed non-sequential and sequential channels, a generalized cross section based on an ionization probability divided by the total number of photon periods cannot be obtained. The is in keeping with the 2 photon double ionization of He, where the generalized cross section cannot be obtained once the energy is in the sequential regime. Calculations for five-photon double ionization probabilities for He are then carried out as a function of photon energy using femtosecond Gaussian pulses. Results were found to be in good agreement with the recent free electron laser experiment [20]. The TDCC method has then been used to calculate 2, 3, 4, and 5 photon double ionization of He using femtosecond Gaussian pulses for both linear and circular polarizations. Total double ionization probabilities were calculated in the energy range from 10 to 60 eV where the 2, 3, 4, and 5 photon absorption dominate the process. Peak total double ionization probabilities are identified for both linear and circular polarized light. At energy around the peak total double ionization probabilities, single and triple differential double ionization probabilities are calculated to guide experiment. For circular polarization the total, single differential, and the triple differential probabilities drop in a steady manner as the number of photons absorbed is increased. We hope these survey calculations will stimulate experimental studies for 2, 3, 4, and 5 photon double ionization of He using femtosecond laser pulses.

Another time-dependent close-coupling method has been developed that includes the spin-orbit interaction through the use of a $l_1 j_1 l_2 j_2 J$ coupling scheme. Double photoionization cross sections for the He atom were then calculated for the $1s^2\ ^1S_0$, $1s2s\ ^3S_1$, and $1s2p\ ^3P_{0,1,2}$ levels. Lattices with 360 × 360 points, a uniform grid spacing of $\Delta r_i = 0.20$, and $lj \leq 3\frac{7}{2}$ angular momenta, and with 720 × 720 points, a uniform grid spacing of $\Delta r_i = 0.10$, and $lj \leq 5\frac{11}{2}$ angular momenta were both used. Good agreement was found between the TDCC($l_1j_1l_2j_2J$) calculations for the $1s^2\ ^1S_0$ level and the TDCC(l_1l_2L) calculations for the $1s^2\ ^1S$ term, as well as between the TDCC($l_1j_1l_2j_2J$) calculations for the $1s2s\ ^3S_1$ level and the TDCC(l_1l_2L) calculations for the $1s2s\ ^3S$ term. The TDCC($l_1j_1l_2j_2j$) calculations for the $1s2p\ ^3P_{0,1,2}$ levels were all found to peak higher than the TDCC(l_1l_2L) calculations for the $1s2p\ ^3P$ term, with the $1s2p\ ^3P_0$ level having the highest peak cross section on both the 360 × 360 point and the 720 × 720 point lattices. However, good agreement was found between the TDCC(l_1l_2L) results for the average of the $1s2p\ ^3P$ and $1s2p\ ^1P$ terms and the TDCC($l_1j_1l_2j_2J$) results for the average of the $1s2p\ ^3P_{0,1,2}$ and $1s2p\ ^1P_1$ levels on the 360 × 360 point lattice. By including two the mass-velocity, and Darwin interactions, a semi-relativistic time-dependent close-coupling method has then been developed through the use of a $l_1j_1l_2j_2J$ coupling scheme. Double photoionization cross sections for the Ne^{8+} atomic ion were calculated for the $1s^2\ ^1S_0$ level. A lattice with 720 × 720 points, a uniform grid spacing of $\Delta r_i = 0.01$, and $lj \leq 5\frac{11}{2}$ coupled channel angular momenta was used. The semi-relativistic TDCC calculations for the $1s^2\ ^1S_0$ level were found to be slightly above the non-relativistic TDCC calculations for the $1s^2\ ^1S$ term. In the future, we plan to continue the application of TDCC method based on a $l_1j_1l_2j_2J$ coupling scheme. Although experimental observation of differences in double photoionization cross sections for the $1s2p\ ^3P_{0,1,2}$ excited levels of He are difficult due to the extremely small fine structure splitting, the possibilities of comparing theory with experiment could be greater for the $1s^22s^22p^2\ ^3P_{0,1,2}$ ground state levels of Carbon or heavier systems. We note that for more highly charged atomic ions, like Kr^{34+}, that the semi-relativistic TDCC method fails and one must use a fully-relativistic TDCC method[60]. Thus, we plan to apply the semi-relativistic TDCC method to the outer subshells of alkaline atoms and their low charged ions in the calculation of total and differential cross sections for single photon and two-photon double ionization to compare with new experimental measurements.

TDCC methods have then been used to calculate single and double photoionization cross sections for Li_2. TDCC-3D method is used to calculate single photoionization cross sections and to find the optimal lattice spacings for use by the TDCC-6D methods. The TDCC-6D method is then used to calculate the single and double photoionization cross sections for Li_2. In contrast to the previous TDCC-6D calculations for H_2 [61], the linear polarization cross sections are larger than the circular polarization cross sections and overall found to be approximately five times larger. We hope that our theoretical work will stimulate future experimental studies of the double photoionization of Li_2.

It has also been shown that the reduction in the Fe XVII 3C/3D line intensity ratio in the X-ray free electron laser at the LCLS facility [1] is likely due to non-equilibrium effects in the intense laser environment. It was shown that the short duration of the laser pulses results in a significant fraction of the detected photon originating from the plasma after the laser pulse has left the plasma volume. If the laser intensity is above $\sim 1 \times 10^{12}$ W/cm^2, this has the effect of reducing the observed line intensity ratio below the oscillator strength ratio value. It was also shown that the non-linear effects included in the DM approach can also be important and have an effect on the expected line intensity ratio. Overall, it appears that the laser intensities above $\sim 1 \times 10^{12}$ W/cm^2 are required for a reduction in the line intensity ratio. It was also shown that even if the experiment consisted of mostly weak pulses, it would only take a small number of intense pulses for them to dominate the line emission. Furthermore, without more precise knowledge of the XFEL pulse parameters and the distribution of pulse intensities and durations, it is not currently possible to extract an oscillator strength ratio from the experimental measurements. However, if the experiment was repeated with mechanisms put in place to eliminate the likelihood of even a small number of intense pulses, then the measurement values should be a good indication of the 3C/3D oscillator strength ratio.

Bibliography

[1] S Bernitt, G V Brown, J K Rudolph, R Steinbrugge, A Graf, M Leutenegger, S W Epp, S Eberle, K Kubicek, V Mackel, M C Simon, E Trabert, E W Magee, C Beilmann, N Hell, S Schippers, A Muller, S M Kahn, A Surzhykov, Z Harman, C H Keitel, J Clementson, F S Porter, W Schlotter, J J Turner, J Ullrich, P Beiersdorfer, and J R Lopez-Urrutia. An unexpectedly low oscillator strength as the origin of the Fe XVII emission problem. Nature, 492(7428):225–228, 2012.

[2] Natalia S. Oreshkina, Stefano M. Cavaletto, Christoph H. Keitel, and Zoltán Harman. Astrophysical line diagnosis requires nonlinear dynamical atomic modeling. Phys. Rev. Lett., 113(14):143001, 2014.

[3] Natalia S. Oreshkina, Stefano M. Cavaletto, Christoph H. Keitel, and Zoltán Harman. X-ray fluorescence spectrum of highly charged Fe ions driven by strong free-electron-laser fields. J. Phys. B, 49(Iii C):094003, 2015.

[4] M S Pindzola, F Robicheaux, S D Loch, J C Berengut, T Topcu, J Colgan, M Foster, D C Griffin, C P Ballance, D R Schultz, T Minami, N R Badnell, M C Witthoeft, D R Plante, D M Mitnik, J A Ludlow, and U Kleiman. The time-dependent close-coupling method for atomic and molecular collision processes. Journal of Physics B: Atomic, Molecular and Optical Physics, 40(7):R39, 2007.

[5] J. Colgan and M. S. Pindzola. Application of the time-dependent close-coupling approach to few-body atomic and molecular ionizing collisions. The European Physical Journal D, 66(11):284, 2012.

[6] M. S. Pindzola, J. Colgan, F. Robicheaux, and D. C. Griffin. Time-dependent close-coupling calculations for the electron-impact ionization of carbon and neon. Phys. Rev. A, 62:042705, Sep 2000.

[7] S D Loch, C P Ballance, D Wu, Sh A Abdel-Naby, and M S Pindzola. Electron-impact ionization of Al. Journal of Physics B: Atomic, Molecular and Optical Physics, 45(6):065201, 2012.

[8] Teck-Ghee Lee, S. D. Loch, C. P. Ballance, J. A. Ludlow, and M. S. Pindzola. Electron-impact-ionization cross sections for excited states of B^{q+} ($q = 0-2$) and an investigation into n scaling of ionization cross sections. Phys. Rev. A, 82:042721, Oct 2010.

[9] C. P. Ballance, S. D. Loch, J. A. Ludlow, Sh. A. Abdel-Naby, and M. S. Pindzola. Electron-impact ionization of C^+ excited states. Phys. Rev. A, 84:062713, Dec 2011.

[10] M S Pindzola, F Robicheaux, and J Colgan. Electron-impact ionization of H_2^+ using a time-dependent close-coupling method. Journal of Physics B: Atomic, Molecular and Optical Physics, 38(17):L285, 2005.

[11] M. S. Pindzola, F. Robicheaux, S. D. Loch, and J. P. Colgan. Electron-impact ionization of H_2 using a time-dependent close-coupling method. Phys. Rev. A, 73:052706, May 2006.

[12] J. Colgan, D. C. Griffin, C. P. Ballance, and M. S. Pindzola. Total cross sections for the double photoionization of Li from the ground and excited states. Phys. Rev. A, 80:063414, Dec 2009.

[13] J A Ludlow, J Colgan, Teck-Ghee Lee, M S Pindzola, and F Robicheaux. Double photoionization of helium including quadrupole radiation effects. Journal of Physics B: Atomic, Molecular and Optical Physics, 42(22):225204, 2009.

[14] J. Colgan and M. S. Pindzola. Core-excited resonance enhancement in the two-photon complete fragmentation of helium. Phys. Rev. Lett., 88:173002, Apr 2002.

[15] S X Hu, J Colgan, and L A Collins. Triple-differential cross-sections for two-photon double ionization of He near threshold. Journal of Physics B: Atomic, Molecular and Optical Physics, 38(1):L35, 2005.

[16] J. Colgan, M. S. Pindzola, and F. Robicheaux. Triple differential cross sections for the double photoionization of H_2. Phys. Rev. Lett., 98:153001, Apr 2007.

[17] K J H Phillips, C J Greer, A K Bhatia, I H Coffey, R Barnsley, and F P Keenan. Fe XVII X-ray lines in solar coronal and laboratory plasmas. Astronomy & Astrophysics, 324:381, 1997.

[18] A. C. Brinkman, C. J. T. Gunsing, J. S. Kaastra, R. L. J. van der Meer, R. Mewe, F. Paerels, A. J. J. Raassen, J. J. van Rooijen, H. Bräuninger, W. Burkert, V. Burwitz, G. Hartner, P. Predehl, J.-U. Ness, J. H. M. M. Schmitt, J. J. Drake, O. Johnson, M. Juda, V. Kashyap, S. S. Murray, D. Pease, P. Ratzlaff, and B. J. Wargelin. First Light Measurements of Capella with the Low-Energy Transmission Grating Spectrometer aboard the Chandra X-Ray Observatory. ApJL, 530:L111–L114, February 2000.

[19] Sh. A. Abdel-Naby, M. F. Ciappina, M. S. Pindzola, and J. Colgan. Nuclear-recoil differential cross sections for the two-photon double ionization of helium. Phys. Rev. A, 87:063425, Jun 2013.

[20] Y. Hikosaka, M. Fushitani, A. Matsuda, T. Endo, Y. Toida, E. Shigemasa, M. Nagasono, K. Tono, T. Togashi, M. Yabashi, T. Ishikawa, and A. Hishikawa. Five-photon sequential double ionization of He in intense extreme-ultraviolet free-electron laser fields. Phys. Rev. A, 90:053403, Nov 2014.

[21] Ofer Kfir, Patrik Grychtol, Emrah Turgut, Ronny Knut, Dmitriy Zusin, Avner Fleischer, Eliyahu Bordo, Tingting Fan, Dimitar Popmintchev, Tenio Popmintchev, Henry

Kapteyn, Margaret Murnane, and Oren Cohen. Helicity-selective phase-matching and quasi-phase matching of circularly polarized high-order harmonics: towards chiral attosecond pulses. Journal of Physics B: Atomic, Molecular and Optical Physics, 49(12):123501, 2016.

[22] Y Li, M S Pindzola, and J Colgan. Five-photon double ionization of helium. Journal of Physics B: Atomic, Molecular and Optical Physics, 49(5):055401, 2016.

[23] M S Pindzola, Y Li, and J Colgan. Multiphoton double ionization of helium using femtosecond laser pulses. Journal of Physics B: Atomic, Molecular and Optical Physics, 49(21):215603, 2016.

[24] Y Li, M S Pindzola, and J Colgan. Double photoionization of helium from the 1s2p ^{3}P excited state. Journal of Physics B: Atomic, Molecular and Optical Physics, 49(19):195205, 2016.

[25] M S Pindzola, Y Li, and J Colgan. A semi-relativistic time-dependent close-coupling method for the double photoionization of Ne^{8+}. International Review of Atomic and Molecular Physics, 6(1):57–65, 2016.

[26] John D. Gillaspy, Wolfgang L. Wiese, and Yuri A. Podpaly. Eighth international conference on atomic data and their applications (ICAMDATA-2012). AIP Conference Proceedings, 1545(1), 2013.

[27] M S Pindzola, Ye Li, and J Colgan. Single and double photoionization of Li_2. Journal of Physics B: Atomic, Molecular and Optical Physics, 48(1):015202, 2015.

[28] S D Loch, C P Ballance, Y Li, M Fogle, and C J Fontes. Non-equilibrium modeling of the fe xvii 3c/3d line ratio in an intense x-ray free-electron laser excited plasma. Apj, 801:L13, 2015.

[29] Liang Feng and Hugo W van der Hart. Two-photon double ionization of he. Journal of Physics B: Atomic, Molecular and Optical Physics, 36(1):L1, 2003.

[30] H. W. van der Hart. Time-dependent R-matrix theory applied to two-photon double ionization of he. Phys. Rev. A, 89:053407, May 2014.

[31] D. A. Horner, F. Morales, T. N. Rescigno, F. Martín, and C. W. McCurdy. Two-photon double ionization of helium above and below the threshold for sequential ionization. Phys. Rev. A, 76:030701, Sep 2007.

[32] A Palacios, D A Horner, T N Rescigno, and C W McCurdy. Two-photon double ionization of the helium atom by ultrashort pulses. Journal of Physics B: Atomic, Molecular and Optical Physics, 43(19):194003, 2010.

[33] J. Feist, S. Nagele, R. Pazourek, E. Persson, B. I. Schneider, L. A. Collins, and J. Burgdörfer. Nonsequential two-photon double ionization of helium. Phys. Rev. A, 77:043420, Apr 2008.

[34] Xiaoxu Guan, K. Bartschat, and B. I. Schneider. Dynamics of two-photon double ionization of helium in short intense XUV laser pulses. Phys. Rev. A, 77:043421, Apr 2008.

[35] Xiaoxu Guan, O Zatsarinny, C J Noble, K Bartschat, and B I Schneider. A time-dependent B-spline R-matrix approach to double ionization of atoms by XUV laser pulses. Journal of Physics B: Atomic, Molecular and Optical Physics, 42(13):134015, 2009.

[36] R. Nepstad, T. Birkeland, and M. Førre. Numerical study of two-photon ionization of helium using an *ab initio* numerical framework. Phys. Rev. A, 81:063402, Jun 2010.

[37] A. S. Simonsen, H. Bachau, and M. Førre. Two-photon double ionization of metastable $^{1,3}S$ $1s2s$ helium. Phys. Rev. A, 89:043427, Apr 2014.

[38] Jonathan S Parker, D H Glass, Laura R Moore, Edward S Smyth, K T Taylor, and P G Burke. Time-dependent and time-independent methods applied to multiphoton ionization of helium. Journal of Physics B: Atomic, Molecular and Optical Physics, 33(7):L239, 2000.

[39] Teck-Ghee Lee, M. S. Pindzola, and F. Robicheaux. Energy and angular differential probabilities for photoionization of He using chirped attosecond soft-x-ray pulses. Phys. Rev. A, 79:053420, May 2009.

[40] Philip Bucksbaum, Thomas Mller, and Kiyoshi Ueda. Frontiers of free-electron laser science. Journal of Physics B: Atomic, Molecular and Optical Physics, 46(16):160201, 2013.

[41] A. Kramida, Yu. Ralchenko, and J. Reader and NIST ASD Team. NIST Atomic Spectra Database (ver. 5.3), [Online]. Available: `http://physics.nist.gov/asd` [2016, November 1]. National Institute of Standards and Technology, Gaithersburg, MD., 2015.

[42] Zheng Zhang, Liang-You Peng, Ming-Hui Xu, Anthony F. Starace, Toru Morishita, and Qihuang Gong. Two-photon double ionization of helium: Evolution of the joint angular distribution with photon energy and two-electron energy sharing. Phys. Rev. A, 84:043409, Oct 2011.

[43] Aihua Liu and Uwe Thumm. Laser-assisted XUV few-photon double ionization of helium: Joint angular distributions. Phys. Rev. A, 89:063423, Jun 2014.

[44] Robert Duane Cowan. The Theory of Atomic Structure and Spectra. Los Alamos Series in Basic and Applied Sciences. University of California Press, Ltd., Berkeley, 1981.

[45] F Maulbetsch and J S Briggs. Selection rules for transitions to two-electron continuum states. Journal of Physics B: Atomic, Molecular and Optical Physics, 28(4):551, 1995.

[46] Jon C. Levin, G. Bradley Armen, and Ivan A. Sellin. Photoionization and Compton double ionization of helium from threshold to 20 keV. Phys. Rev. Lett., 76:1220–1223, Feb 1996.

[47] R. Dörner, T. Vogt, V. Mergel, H. Khemliche, S. Kravis, C. L. Cocke, J. Ullrich, M. Unverzagt, L. Spielberger, M. Damrau, O. Jagutzki, I. Ali, B. Weaver, K. Ullmann, C. C. Hsu, M. Jung, E. P. Kanter, B. Sonntag, M. H. Prior, E. Rotenberg, J. Denlinger, T. Warwick, S. T. Manson, and H. Schmidt-Böcking. Ratio of cross sections for double to single ionization of He by 85-400 eV photons. Phys. Rev. Lett., 76:2654–2657, Apr 1996.

[48] Kurt W. Meyer and Chris H. Greene. Double photoionization of helium using R -matrix methods. Phys. Rev. A, 50:R3573–R3576, Nov 1994.

[49] Anatoli S. Kheifets and Igor Bray. Calculation of double photoionization of helium using the convergent close-coupling method. Phys. Rev. A, 54:R995–R997, Aug 1996.

[50] Pascale J. Marchalant and Klaus Bartschat. R matrix with pseudostates calculation for single and double ionization of helium by photon impact. Phys. Rev. A, 56:R1697–R1700, Sep 1997.

[51] M. S. Pindzola and F. Robicheaux. Time-dependent close-coupling calculations of correlated photoionization processes in helium. Phys. Rev. A, 57:318–324, Jan 1998.

[52] Yanghui Qiu, Jian-Zhi Tang, Joachim Burgdörfer, and Jianyi Wang. Double photoionization of helium from threshold to high energies. Phys. Rev. A, 57:R1489–R1492, Mar 1998.

[53] Hugo W. van der Hart, Kurt W. Meyer, and Chris H. Greene. Double photoionization and ionization excitation of the metastable helium S states. Phys. Rev. A, 57:3641–3645, May 1998.

[54] A. S. Kheifets, A. Ipatov, M. Arifin, and Igor Bray. Double-photoionization calculations of the helium metastable $2^{1,3}S$ states. Phys. Rev. A, 62:052724, Oct 2000.

[55] J. Colgan and M. S. Pindzola. Total and differential cross-section calculations for the double photoionization of the helium $1s2s^{1,3}S$ states. Phys. Rev. A, 67:012711, Jan 2003.

[56] Anatoli S. Kheifets and Igor Bray. Photoionization with excitation and double photoionization of the helium isoelectronic sequence. Phys. Rev. A, 58:4501–4511, Dec 1998.

[57] Hugo W van der Hart and Liang Feng. Double photoionization of excited He-like atoms. Journal of Physics B: Atomic, Molecular and Optical Physics, 34(18):L601, 2001.

[58] U. Kleiman, M. S. Pindzola, and F. Robicheaux. Photoionization with excitation and double photoionization of the Li^+ ground $1\,^1S$ state and metastable $2\,^{1,3}S$ states. Phys. Rev. A, 72:022707, Aug 2005.

[59] J. A. R. Samson, W. C. Stolte, Z.-X. He, J. N. Cutler, Y. Lu, and R. J. Bartlett. Double photoionization of helium. Phys. Rev. A, 57:1906–1911, Mar 1998.

[60] M. S. Pindzola, J. A. Ludlow, and J. Colgan. Photoionization of highly charged atomic ions. Phys. Rev. A, 81:063431, Jun 2010.

[61] J Colgan, M S Pindzola, and F Robicheaux. Time-dependent close-coupling calculations for the double photoionization of He and H_2. Journal of Physics B: Atomic, Molecular and Optical Physics, 37(23):L377, 2004.

[62] W. Vanroose, F. Martín, T. N. Rescigno, and C. W. McCurdy. Nonperturbative theory of double photoionization of the hydrogen molecule. Phys. Rev. A, 70:050703, Nov 2004.

[63] G. Dujardin, M. J. Besnard, L. Hellner, and Y. Malinovitch. Double photoionization of H_2: An experimental test of electronic-correlation models in molecules. Phys. Rev. A, 35:5012–5019, Jun 1987.

[64] H. Kossmann, O. Schwarzkopf, B. Kämmerling, and V. Schmidt. Unexpected behaviour of double photoionization in H_2. Phys. Rev. Lett., 63:2040–2043, Nov 1989.

[65] W. Vanroose, D. A. Horner, F. Martín, T. N. Rescigno, and C. W. McCurdy. Double photoionization of aligned molecular hydrogen. Phys. Rev. A, 74:052702, Nov 2006.

[66] M. Gisselbrecht, M. Lavollée, A. Huetz, P. Bolognesi, L. Avaldi, D. P. Seccombe, and T. J. Reddish. Photodouble ionization dynamics for fixed-in-space H_2. Phys. Rev. Lett., 96:153002, Apr 2006.

[67] T. J. Reddish, J. Colgan, P. Bolognesi, L. Avaldi, M. Gisselbrecht, M. Lavollée, M. S. Pindzola, and A. Huetz. Physical interpretation of the "kinetic energy release" effect in the double photoionization of H_2. Phys. Rev. Lett., 100:193001, May 2008.

[68] J. M. Feagin, J. Colgan, A. Huetz, and T. J. Reddish. Electron-pair excitations and the molecular coulomb continuum. Phys. Rev. Lett., 103:033002, Jul 2009.

[69] FP Larkins and JA Richards. Photoionisation and Auger electron emission from the lithium molecule: Calculations using multicentre numerical continuum functions. Australian Journal of Physics, 39(5):809–828, 10 1986.

[70] Roberto Moccia and Raffaele Montuoro. Mixed L^2 basis set: STOs plus B-splines. calculation of the differential photoionization cross-section of Li_2. Chemical Physics Letters, 368(34):430 – 438, 2003.

[71] J. Colgan, M. S. Pindzola, and F. Robicheaux. Time-dependent studies of single and multiple photoionization of H_2^+. Phys. Rev. A, 68:063413, Dec 2003.

[72] ALCHEMY, 1970. (San Jose, CA: IBM Research Laboratory).

[73] Michael A. Morrison. ALAM, a program for the calculation and expansion of molecular charge densities. Computer Physics Communications, 21(1):63 – 77, 1980.

[74] NIST Computational Chemistry Comparison and Benchmark Database NIST Standard Reference Database Number 101 Release 18, October 2016, Editor: Russell D. Johnson III , [Online]. Available: `http://cccbdb.nist.gov/` .

[75] M. J. Frisch, G. W. Trucks, H. B. Schlegel, G. E. Scuseria, M. A. Robb, J. R. Cheeseman, G. Scalmani, V. Barone, B. Mennucci, G. A. Petersson, H. Nakatsuji, M. Caricato, X. Li, H. P. Hratchian, A. F. Izmaylov, J. Bloino, G. Zheng, J. L. Sonnenberg, M. Hada, M. Ehara, K. Toyota, R. Fukuda, J. Hasegawa, M. Ishida, T. Nakajima, Y. Honda, O. Kitao, H. Nakai, T. Vreven, J. A. Montgomery, Jr., J. E. Peralta, F. Ogliaro, M. Bearpark, J. J. Heyd, E. Brothers, K. N. Kudin, V. N. Staroverov, R. Kobayashi, J. Normand, K. Raghavachari, A. Rendell, J. C. Burant, S. S. Iyengar, J. Tomasi, M. Cossi, N. Rega, J. M. Millam, M. Klene, J. E. Knox, J. B. Cross, V. Bakken, C. Adamo, J. Jaramillo, R. Gomperts, R. E. Stratmann, O. Yazyev, A. J. Austin, R. Cammi, C. Pomelli, J. W. Ochterski, R. L. Martin, K. Morokuma, V. G. Zakrzewski, G. A. Voth, P. Salvador, J. J. Dannenberg, S. Dapprich, A. D. Daniels, . Farkas, J. B. Foresman, J. V. Ortiz, J. Cioslowski, and D. J. Fox. Gaussian 09 Revision E.01. Gaussian Inc. Wallingford CT 2009.

[76] Molecular Modeling Basics. CRC Press, 2010.

[77] G. V. Brown, P. Beiersdorfer, H. Chen, M. H. Chen, and K. J. Reed. Diagnostic Utility of the Relative Intensity of 3C to 3D in Fe XVII. ApJL, 557:L75–L78, August 2001.

[78] S D Loch, M S Pindzola, C P Ballance, and D C Griffin. The effects of radiative cascades on the x-ray diagnostic lines of Fe^{16+}. Journal of Physics B: Atomic, Molecular and Optical Physics, 39(1):85, 2006.

[79] Guo-Xin Chen. Converged Dirac R-matrix calculation of electron impact excitation of Fe XVII. Phys. Rev. A, 76:062708, Dec 2007.

[80] M. F. Gu. New benchmark of x-ray line emission models of Fe xvii, 2009.

[81] G V Brown. A brief review of the intensity of lines 3C and 3D in neon-like Fe XVII. Can. J. Phys., 86:199–208, 2008.

[82] G. V. Brown and P. Beiersdorfer. Brown and Beiersdorfer reply. Phys. Rev. Lett., 108(13):139302, 2012.

[83] U. I. Safronova, C. Namba, I. Murakami, W. R. Johnson, and M. S. Safronova. Electric-dipole, electric-quadrupole, magnetic-dipole, and magnetic-quadrupole transitions in the neon isoelectronic sequence. Phys. Rev. A, 64(1):012507, July 2001.

[84] T Pfeifer, Y Jiang, S Dusterer, R Moshammer, and J Ullrich. Partial-coherence method to model experimental free-electron laser pulse statistics. Opt. Lett., 35(20):3441–3443, 2010.

[85] Stefano M. Cavaletto, Christian Buth, Zoltán Harman, Elliot P. Kanter, Stephen H. Southworth, Linda Young, and Christoph H. Keitel. Resonance fluorescence in ultrafast and intense X-ray free-electron-laser pulses. Phys. Rev. A, 86(3):033402, 2012.

[86] Philip Heimann, Oleg Krupin, William F. Schlotter, Joshua Turner, Jacek Krzywinski, Florian Sorgenfrei, Marc Messerschmidt, David Bernstein, Jaromir Chalupský, Vera

Hájková, Stefan Hau-Riege, Michael Holmes, Libor Juha, Nicholas Kelez, Jan Lüning, Dennis Nordlund, Monica Fernandez Perea, Andreas Scherz, Regina Soufli, Wilfried Wurth, and Michael Rowen. Linac coherent light source soft x-ray materials science instrument optical design and monochromator commissioning. Review of Scientific Instruments, 82(9):093104, 2011.